Dissertation

submitted to the
Combined Faculties for the Natural Sciences and for Mathematics
of the Ruperto-Carola University of Heidelberg, Germany

for the degree of
Doctor of Natural Sciences

Put forward by

SÁNCHEZ PARCERISA, Daniel
Born in: Madrid, Spain

Oral examination: July, 25th 2012

Experimental and computational investigations on the water-to-air stopping power ratio for ion chamber dosimetry in carbon ion radiotherapy

Referees:

Priv-Doz. Dr. Katia Parodi
Prof. Dr. Christian Karger

Examiners:

Prof. Dr. Luca Amendola
Prof. Dr. Dirk Dubbers

PhD Advisors:

Priv-Doz. Dr. Katia Parodi
Dr. Eike Rietzel
Prof. Dr. Oliver Jäkel
Dr. Alexander Gemmel

Zusammenfassung

Die Partikeltherapie ist eine zukunftsweisende Form der Strahlentherapie zur Bekämpfung von Krebs, die die Applikation von äußerst tumorkonformen Dosisverteilungen bei gleichzeitiger Schonung gesunden Gewebes ermöglicht. Die vorliegende Arbeit zielt auf eine Verbesserung der Genauigkeit der Dosimetrie mit Ionisationskammern bei der Partikeltherapie mit Kohlenstoffionen ab. Das Messsignal luftgefüllter Ionisationskammern wird durch eine Reihe von Korrekturfaktoren beeinflusst, die teilweise nur mit begrenzter Genauigkeit bekannt sind. Diese Studie untersucht einen dieser Korrekturfaktoren, nämlich das Verhältnis des Bremsvermögens von Wasser und Luft, $s_{w,air}$.

In einem ersten Schritt haben wir experimentelle Messungen mit monoenergetischen Kohlstoffionen zur Bestimmung des Verhältnisses des Bremsvermögens von Wasser und Luft geplant und durchgeführt. Danach haben wir die Monte Carlo Software FLUKA benutzt, um die Ergebnisse der Messungen auf realistische Therapiestrahlen zu erweitern und ein Modell zur Berechnung von $s_{w,air}$ für jede Position im Behandlungsfeld zu entwickeln. Schließlich haben wir das entwickelte Modell anhand von Patientenbeispielen getestet, um seine Anwendung in der Absolutdosimetrie und Planverifikation zu untersuchen. Die erzielten Ergebnisse sind vielversprechend und können, wenn sie in die empfohlenen Dosimetrieprotokolle aufgenommen werden, die Unsicherheit bei der Bestimmung der absorbierten Dosis in der Kohlenstoffionentherapie vermindern.

Abstract

Particle therapy is an advanced modality of cancer radiotherapy which allows the delivery of a highly conformal dose to the tumour while considerably sparing healthy tissue. This work aims at improving the accuracy of ion chamber dosimetry for particle therapy with carbon ion beams. The readout of air-filled ionization chambers is affected by a number of correction factors, some of which are known only with limited accuracy. This study deals with one of this beam quality correction factors, the stopping power ratio between water and air, or $s_{w,air}$.

On a first step, we planned and carried out experimental measurements to determine the value of water-to-air stopping power ratio in monoenergetic carbon ion beams. Then, we used the Monte Carlo code FLUKA to extend the results of those measurements to realistic treatment beams, and to develop a model to calculate $s_{w,air}$ for any given position in a treatment field. Finally, we tested the developed model in patient cases, to study its possible application in absolute dosimetry and patient plan verification. The obtained results are promising and can, if incorporated in the recommended dosimetry protocols, reduce the uncertainty margins in the determination of absorbed dose for carbon ion beam radiotherapy.

Acknowledgements

When a journey is about to end, it is a joy to look over the walked path and have some thoughts for the people who walked it with you.

In first place, I want to thank my advisors, all of whom gave their best to assist me on this task. In particular, I would like to mention Dr. Alex Gemmel, who supported me day after day and did not let me fall into despair, and Prof. Katia Parodi, who managed to be always extremely supportive and helpful despite the distance.

I want to show gratitude to all my colleagues at Siemens Particle Therapy for their warm welcome in Erlangen, for sharing their knowledge with me, for their patient assistance whenever it was needed, and for giving me a grasp on the Franconian / Bavarian / German way of life. In addition, I want to thank all the technical team who assisted me with the experiments during the endless night shifts in Heidelberg and Marburg.

This Thesis would not have been possible without the support of the PARTNER family. Or, better to say, had it been possible, it would certainly not have been that much fun! Thank you for demonstrating that sometimes, the best science is done around a table full of beers. My acknowledgement goes, as well, to all the professors who contributed to the success of the PARTNER courses, led by our coordinator, Prof. Manjit Dosanjh.

Finally, I would like to thank those closest to me, just for being part of my life. No need to cite all the names here, *you know who you are*. I feel very lucky to have the support of my family, especially my parents, thanks to whom I am who I am: their unconditional love makes me want to be a better person every day. Thanks as well to all the great friends who were by my side during my time in Erlangen: they became my second family, and their company is the best memory that I bring with me. To my SOBFs, or "Spread-Out Best Friends", those extraordinary human beings who, no matter from where, are always there to cheer me up with an email, a telephone call, or a visit; to all of you, I say, *gracias*.

And last but not least, to Pilar, for your affection, your support, your sympathy, and what is more important: for all those things that are yet to come. Every single one of the countless hours spent on planes has been well worth it.

Foreword

This Thesis describes the work that I have carried out as an Early Stage Researcher (ESR) at Siemens Particle Therapy, Erlangen, Germany, and as a member of the European FP7-Marie Curie Initial Training Network "PARTNER" and a registered graduate student at the Faculty of Physics and Astronomy at the University of Heidelberg. The work has been supervised by Dr. Eike Rietzel and Dr. Alexander Gemmel (Siemens AG), Priv-Doz. Dr. Katia Parodi (HIT) and Prof. Dr. Oliver Jäkel (DKFZ / HIT).

The manuscript is organized in seven chapters. The first one describes the goals of the research, and frames the work in its scientific and social context. Chapters two and three describe the underlying theory which supports the presented investigation; in particular, they describe the basics of radiotherapy with charged particles (Chapter 2) and the main procedures used in charged particle dosimetry (Chapter 3). The fourth chapter is devoted to the Monte Carlo code FLUKA, which was extensively used for the investigations. Chapter 5 describes the main scientific contributions of the Thesis, including experimental results, Monte Carlo simulations and physical modelling. In the Chapter 6, these results are applied to a realistic clinical environment. Finally, Chapter 7 is an outlook of the results, with stress on possible future lines of work.

The research leading to these results has received funding from the European Community's Seventh Framework Program 2007-2013 under grant agreement n° 215840-2.

Contents

CHAPTER 1 Context and purpose of the thesis 1

1.1. Treating cancer with particles 1

1.2. Particle Therapy in Europe: ENLIGHT and PARTNER 3

1.3. Particle Therapy Centers in Europe 3

1.3.1. Heidelberg Ion-Beam Therapy Center (HIT) 4

1.3.2. Siemens Simulation and Test Center, Marburg 4

1.4. Reference dosimetry and international standards 5

1.5. Scope of the thesis 6

CHAPTER 2 Basics of particle therapy 7

2.1. Physics of particle therapy 7

2.1.1. Stopping of charged particles 7

2.1.2. Range of particles in matter 10

2.1.3. Multiple Coulomb scattering 12

2.1.4. Linear Energy Transfer and track structure 13

2.1.5. Nuclear interactions and fragmentation 15

2.2. Radiobiology and particle therapy 16

2.3. Practical aspects of particle therapy 19

2.3.1. Accelerators for particle therapy 19

2.3.2. Choice of projectile 20

2.3.3. Delivering dose to the tumour 21

2.3.4. From dose prescription to treatment planning 23

2.3.5. Machine and patient QA 26

CHAPTER 3 Relevant aspects of dosimetry for Particle Therapy 27

3.1. Introduction 27

3.2. Dosimetry equipment 27

3.2.1. Calorimeters 27

3.2.2. Ionization chambers 28

3.3. Dosimetry under reference conditions 29

3.4. Dosimetry under non-reference conditions 31

3.4.1. Monitor calibration 31

3.4.2. Plan verification 34

CHAPTER 4 Monte Carlo simulations and experimental validation 37

4.1 Introduction 37

4.2 The FLUKA code 37

4.3 Choice of physics settings for particle therapy simulations 38

4.4 Experimental-based validation of FLUKA simulations 39

CHAPTER 5 Experimental and computational assessment of $s_{w,air}$ in ^{12}C beams .. 45

5.1. Introduction 45

5.2. Dependence of $s_{w,air}$ with the kinetic energy of the particles 48

5.3. Experimental measurement of $s_{w,air}$ 49

5.3.1. Principle 49

5.3.2. Measurement of Bragg peak positions 49

5.3.3. Alignment of the PeakFinder^{TM} 52

5.3.4. Atmospheric conditions 54

5.3.5. Experimental values of $s_{w,air}$ derived from range shift measurements 55

5.3.6. Energy dependence of $s_{w,air}$ 55

5.3.7. Estimation of uncertainties 58

5.3.8. Discussion of the experimental results 61

5.4. Monte Carlo calculation with FLUKA 62

5.4.1. Introduction 62

5.4.2. Restricted stopping power tables for air and water 63

5.4.3. Implementation with FLUKA 66

5.4.4. Results 67

5.4.5. Discussion 70

5.5. An empirical expression for water-to-air stopping power ratio 73

CHAPTER 6 Monte Carlo study on plan verification with ionization chambers ... 77

6.1. Plan verification with an ionization chamber matrix 77

6.2. Water-to-air stopping power ratio in full patient plans 77

6.2.1. Introduction 77

6.2.2. 3D Stopping power ratio maps 78

6.2.3. Application of empirical expression to plan verification 82

6.3. Monte Carlo study of the plan verification IC matrix 83

6.3.1. Modeling ionization chambers and detector block with FLUKA 83

6.3.2. Physical crosstalks between IC chambers 86

6.3.3. Chamber-specific $s_{w,air}$ 88

6.4. Conclusions 90

CHAPTER 7 Outlook and conclusions 91

Publications resulting from this Thesis 93

References 95

List of figures

Figure 1.1. Absolute cancer incidence and mortality at the 27-EU, year 2008. (Source: European Cancer Observatory, http://eu-cancer.iarc.fr) 1

Figure 1.2. Dose profiles of various particles (Source: [HAETTNER2006] with data from U. Weber)..... 2

Figure 1.3. Schematic view of the HIT facility (Source: http://www.klinikum.uni-heidelberg.de)..... 4

Figure 1.4. Layout of the Siemens Particle Therapy Simulation and Test Center, in Marburg (Source: http://www.medical.siemens.com) 5

Figure 2.1. Experimental depth dose distributions of ^{12}C ions and in water for different initial energies (Source: [SCHARDT2010]) 7

Figure 2.2. Stopping power of ^{12}C ions and protons in water. The top axis label additionally shows the corresponding range in water for carbon ions (Source: [SCHARDT2010]) . 10

Figure 2.3. Possible measurements of fluence, differential fluence and dose distribution of three proton beams of the same energy with different initial energy spreads, to illustrate $R = d_{80}$ (source: [GOTTSCHALK2004]) 11

Figure 2.4. Range-energy relationship for protons and carbon ions in water. Data from [ICRU1994] and [SIGMUND2009] fit to $R_0=\alpha \cdot T^{\beta}$ with $\beta=1.74$ for protons, and $\beta=1.65$ for carbon ions. 12

Figure 2.5. CSDA range of electrons in water (from NIST, ESTAR database [BERGER2005])..... 14

Figure 2.6. Fragmentation as a two step process (source: [HAETTNER2006])..... 15

Figure 2.7. Depth dose distribution of a 200 MeV/u carbon ion beam. Black solid line represents the full dose, with the blue dashed and solid lines depict the contribution from primary ions and fragments (as calculated with Monte Carlo code PHITS [NIITA2006]). The bottom image shows a zoom of the dose contribution from the main fragments (source: [GUNZERTMARX2008]) 16

Figure 2.8. Definition of RBE, illustrated for cell survival curves (Source: [KRAFT2000]).17

Figure 2.9. Effect of RBE. Biologically equivalent SOBPs (spread out Bragg peaks) constructed by scaling the physical dose with the assumed RBE for protons (left) and carbon ions (right) (source: [IAEA2008])..... 18

Figure 2.10. Depth dose distributions in water for pure monoenergetic beams of different ions with similar range and initial energy spread. Calculated with the Monte Carlo code FLUKA [FASSO2005, BATTISTONI2007]. The higher straggling of lighter ions, and the pronounced tail of the heavier particles can be clearly appreciated. 20

Figure 2.11. The lateral penumbra of a carbon ion beam is much sharper than that of a proton beam (source: [CHU2006]). 21

Figure 2.12. Schematic view of a passive scattering (top) and active scanning (bottom) beam delivery systems (source: [MARC2010]). 22

Figure 2.13. For photon treatment, range errors have a small impact in dose distribution. In contrast, for light ions, due to their sharp dose distribution, a similar error in range could result in much more severe dose mismatch (from [CHU2006]). 24

Figure 2.14. Conversion of CT numbers to water-equivalent path lengths [CHU2006]..... 24

Figure 2.15. Comparison of a photon IMRT plan (left) with 7 fields, and a proton plan with 2 fields (right), for the same patient. It is evident that the proton plan achieves a much more conformal dose with fewer fields (from [GEORG2010]). 25

Figure 3.1. PeakFinder^{TM} used for depth dose measurements positioned on the treatment table at HIT. The beam comes from the nozzle on the left side. 28

Figure 3.2. Definitions of practical range (R_p) and residual range (R_{res}). Figure adapted from [IAEA2000]..... 29

Figure 3.3. Differences in monitor calibration between different ion beam delivery systems. For passive delivery (a), the IC is placed at the center of the SOBP, and the calibration is done in terms of dose/MU, whereas in active delivery (b), the reference dosimeter is placed at the entrance channel of a pristine Bragg peak and the monitor units are converted directly to the number of irradiated particles (from [KARGER2010]). 33

Figure 3.4. PTW Water Phantom (PTW Freiburg, Germany) used for plan verification and QA measurements of proton and light ion beams. 35

Figure 4.1. Simulated depth dose distributions and experimental data measured at HIT for carbon ions (top) and in STCM for protons (bottom) 41

Figure 4.2. Difference in range (80% distal fall-off) between the simulated and measured curves, for different values of the mean ionization potential of water I_w in the simulation for carbon ions (top) and protons (bottom) 42

Figure 5.1. Direct ratio of water to air stopping powers for protons and other light ions according to different stopping power tables as of 1999 [SCHWAB1990, ICRU1994, HIRAOKA1995], motivating the current adoption of the constant value of 1.13 for carbon ion beams. (Source: [HARTMANN1999]) 46

Figure 5.2. Mean water to air stopping power ratio of carbon ions as a function of penetration depth, normalized to unity at zero depth, for monoenergetic beams (left) and a SOBP centred at 5 cm (right, as marked by the dashed vertical lines), calculated with equation (5.1). (Source: [HARTMANN1999]). 46

Figure 5.3. Monte Carlo calculations performed with the SHIELD-HIT coe [DEMENTYEV1999, GUDOWSKA2004] to determine the $s_{w,air}$ ratio for a carbon ion beam of 270 MeV/u initial energy when using different sets of I_w and I_{air} (adapted from [LUHR2011]). The I-value sets correspond to different published data. Discrimination with atomic number Z indicates that the available data tables have been calculated using different I-values for different particles. 47

Figure 5.4: Scheme of the experimental setup. 50

Figure 5.5: Determination of peak position by polynomial fit on E=100.07 MeV/u (left) and E=430.10 MeV/u. The peak of higher energy is broader due to straggling, as reflected by the different scale of the horizontal axis 51

Figure 5.6. Water column positioned in front of the beam nozzle at the QA room of HIT. The red laser markers at the planes of the isocenter are aligned with the black marks on the surface of the water column. 52

Figure 5.7. Measurement of angle between the beam and the water column using a calibrated electronic level. 53

Figure 5.8. Range shortening of a 270 MeV/u carbon ion beam with a polar angle simulating a vertical misalignment of the water column. The solid line plots the range at 0º multiplied by cos(θ). 53

Figure 5.9: Peak position in dependence of air gap for carbon ions at different energies. The higher dispersion in the peak positions for the higher energies is due to the broader peaks, and it causes, in turn, a higher uncertainty in the derived $s_{w,air}$. 56

Figure 5.10: Water-to-air stopping power ratio vs. beam energy. The error bars of the experimental points show the combined standard uncertainties, and the label below them represents the number of repeated measurement series for each point. The weighted average is shown in black. The blue line shows the fit to expression (5.4) for $I_{air}/I_w = 1.157$. Dotted lines indicate the 95% confidence intervals for the fit and for the weighted mean. 57

Figure 5.11. Restricted stopping power tables in water for several isotopes from p to ^{16}O, as calculated with FLUKA. The δ-ray production threshold was set at 30 keV. 64

Figure 5.12. Restricted (δ threshold=30 keV) stopping power of ^{12}C in water, as calculated with the script, compared to the table shown in the FLUKA output file. 65

Figure 5.13. Restricted stopping power of electrons in water calculated with FLUKA for a δ-ray threshold of 30 keV, compared to the unrestricted stopping power from ESTAR database [BERGER2005]..... 65

Figure 5.14. Comparison of dose and *fluw* scorers, yielding similar depth dose distributions, for three pristine 12C Bragg peaks..... 67

Figure 5.15. In red, stopping power ratios of ^{12}C monoenergetic beams of 100.07 MeV/u (top left), 270.55 MeV/u (top right) and 430.10 MeV/u (bottom left), with the 1σ confidence interval, calculated with FLUKA. In green, deposited dose to water. In brown, experimental measurements, as detailed in section 5.3..... 68

Figure 5.16. In red, stopping power ratios of SOBPs of ^{12}C of different depths and sizes, with 1σ confidence interval, calculated with FLUKA. In green, deposited dose to water..... 69

Figure 5.17. $s_{w,air}$ (in red) and depth dose distribution (in green) for pristine peaks of 100.07, 270.55 and 430.10 MeV/u (left) and for nine ^{12}C SOBPs in water (right), plotted as a function of residual range, calculated with FLUKA. 70

Figure 5.18. FLUKA calculations for deposited dose (left) and $s_{w,air}$ (right) for a cubic volume of homogeneous dose in water irradiated with ^{12}C. Horizontal slice in the XZ

plane for y=0 cm (the plan is centered at the point {0,0,5}, in cm). Contours in the $s_{w,air}$ plot represent isodose lines. 71

Figure 5.19. One-dimensional plots showing $s_{w,air}$ and deposited dose for the longitudinal axis (left) and the transversal axis (right), corresponding to the profiles marked by the dashed lines on Figure 5.18. 71

Figure 5.20. FLUKA calculations for deposited dose and $s_{w,air}$ for a cubic volume of homogeneous dose in water irradiated with ^{12}C. Vertical slice in the YZ plane for x=0 cm (the plan is centered at the point {0,0,5}, in cm). Contours in the $s_{w,air}$ plot represent isodose lines. 71

Figure 5.21. FLUKA calculations for deposited dose and $s_{w,air}$ for a cubic volume of homogeneous dose in water irradiated with ^{12}C. Beam's eye view slice in the XY plane for z=5 cm (the plan is centered at the point {0,0,5}, in cm). Contours in the $s_{w,air}$ plot represent isodose lines. 72

Figure 5.22. FLUKA calculation of $s_{w,air}$ versus residual range, for three monoenergetic ^{12}C beams of 100.07, 270.55 and 430.10 MeV/u using a delta ray threshold of 30 keV (blue), and no delta ray tracking at all, using unrestricted stopping power tables (red). In brown are shown the experimentally measured values (cf. section 5.3). 73

Figure 5.23. $s_{w,air}$ calculated with expression (5.11) (blue line), with fit parameters obtained from FLUKA calculated stopping power ratios (red dots) for nine ^{12}C SOBPs. 75

Figure 5.24. Comparison of the 1σ-confidence interval for $s_{w,air}$ given from the proposed expression (blue lines over white area), and the currently recommended value from TRS-398 [IAEA2000] (grey area). 75

Figure 6.1 Snapshot of the plan verification interface from the TPS software (Syngo PT Planning, Siemens Particle Therapy) in use at the Siemens Test Centre Marburg. The white circles represent the positions of the ionization chambers in the matrix, inside the water phantom. 77

Figure 6.2. CT images and delineation of target volumes (red) and organs at risk (black) for a head-and-neck patient (patient #1, left) and a pelvic patient (patient #2, right) 78

Figure 6.3. FLUKA calculations for deposited dose and $s_{w,air}$ for the plan verification of one field of patient treatment plan #1, irradiated with ^{12}C in water. Horizontal slice in the XZ plane for y=0 cm. Contours in the $s_{w,air}$ plot represent isodose lines. 79

Figure 6.4. One-dimensional plots showing $s_{w,air}$ and deposited dose for the longitudinal axis (left) and the transversal axis (right), corresponding to the profiles marked by the dashed lines on Figure 6.3. 79

Figure 6.5. FLUKA calculations for deposited dose and $s_{w,air}$ for the plan verification of one field of patient treatment plan #1, irradiated with ^{12}C in water. Vertical slice in the XY plane for x=0 cm. Contours in the $s_{w,air}$ plot represent isodose lines. 79

Figure 6.6. FLUKA calculations for deposited dose and $s_{w,air}$ for the plan verification of one field of patient treatment plan #1, irradiated with ^{12}C in water. Beam's eye view slice in the XY plane for z=8.2 cm. Contours in the $s_{w,air}$ plot represent isodose lines. 80

Figure 6.7. FLUKA calculations for deposited dose and $s_{w,air}$ for the plan verification of one field of patient treatment plan #2, irradiated with ^{12}C in water. Horizontal slice in the XZ plane for y=0 cm. Contours in the $s_{w,air}$ plot represent isodose lines. 80

Figure 6.8. One-dimensional plots showing $s_{w,air}$ and deposited dose for the longitudinal axis (left) and the transversal axis (right), corresponding to the profiles marked by the dashed lines on Figure 6.7..... 81

Figure 6.9. FLUKA calculations for deposited dose and $s_{w,air}$ for the plan verification of one field of patient treatment plan #2, irradiated with ^{12}C in water. Vertical slice in the XY plane for x=0 cm. Contours in the $s_{w,air}$ plot represent isodose lines..... 81

Figure 6.10. FLUKA calculations for deposited dose and $s_{w,air}$ for the plan verification of one field of patient treatment plan #1, irradiated with ^{12}C in water. Beam's eye view slice in the XY plane for z=16.5 cm. Contours in the $s_{w,air}$ plot represent isodose lines. 81

Figure 6.11. Scheme depicting the determination of the R_{25} reference point, depending on the effective point of measurement in the field..... 82

Figure 6.12. $s_{w,air}$ calculated with FLUKA simulation (left) and with the analytical algorithm described in section 6.2.3 (right), for a cubic volume (top), patient plan #1 (middle) and #2 (bottom)..... 84

Figure 6.13. Dose distribution with automatic subdivision of treatment field (left) and histograms showing the distribution of errors in $s_{w,air}$ for the 4 parts in which the field is divided, comparing the $s_{w,air}$ values given by IAEA and the R_{res} model with the results of the full FLUKA calculation (right). 85

Figure 6.14. Technical drawings of PTW model 31015 [PTW2009] (left), and scheme of implementation with FLUKA combinational geometry (right). 86

Figure 6.15. Upper (left) and lateral schematic views (right) of the detector block PTW Freiburg T21003 showing the 24 ionization chambers (PTW model 31015). 86

Figure 6.16. Test positions of the second chamber around the reference chamber in lateral, posterior, lateral-posterior and lateral-anterior directions. The colour wash display in the background shows the dose distribution for a 200 MeV/u ^{12}C beam extended homogeneously in the transversal directions (FLUKA simulation)..... 87

Figure 6.17. Dose collected by the reference chamber in presence of a second chamber at a given distance in four different directions, relative to the dose by collected by the chamber in absence of a second chamber. Solid lines are shown only to guide the eye.88

Figure 6.18. Vertical and horizontal projections of the ionization chamber matrix in the field. Dose distribution shown at the background for y=0 (horizontal projection, left) and for x=0 (vertical projection, right). 89

Figure 6.19. Chamber-specific values of $s_{w,air}$ for patient plan #1 and matrix geometry as shown in Figure 6.18, as calculated with full FLUKA simulation (blue) and as predicted by the residual range model according to the effective position of the chambers (red). Positions of the ionization chambers are detailed in Figure 6.14..... 89

List of tables

Table 2.1. Contribution to stopping power for protons in aluminium, in percent, of the different terms of the Bethe-Bloch expression (equation (2.2)). Source: [ZIEGLER1999] 9

Table 3.1. Definition of the perturbation factors in p_Q 32

Table 3.2. Estimated relative uncertainties (in %) for the quality factors and corresponding components for proton and light ion beams, including the uncertainty in the quantities related to the the reference radiation [IAEA2000]. 32

Table 4.1. Transport limits for different particle types in FLUKA (source: FLUKA manual) 38

Table 5.1. Statistical variation in the reference point of a DDD (range or peak position) determined by different methods, for 10 consecutive measurements with a ^{12}C beam of 100.07 MeV/u in water. 51

Table 5.2. Comparison of nominal energies and estimated average energies inside the air gap. The values from the last column are used for the fit in Figure 5.10. 55

Table 5.3. Sensitivity analysis for the result of the fit. Resulting (I_a/I_w) for different starting I_w values 57

Table 5.4. Typical values and uncertainties for the quantities used to calculate the solid thickness of air traversed by the beam, *t*, and the mass fraction of water moist, *f*. 59

Table 5.5. Uncertainties in the peak position for different energies derived from repeatability studies, including mechanical uncertainty of the water column and error of the fit. 60

Table 5.6. Uncertainty analysis for water-to-air stopping power ratio, calculated from equation (5.8). 60

Table 5.7. Average parameters for the fits of nine ^{12}C SOBPs to equation (5.11) for three different sets of water and air I-values. 74

CHAPTER 1 Context and purpose of the thesis

1.1. Treating cancer with particles

Cancer causes about one in every four deaths in Europe and the US [NIEDERLANDER2006, HOWLADER2011]. About 2.5 million people are diagnosed with cancer every year in the EU, and about 1.2 million are killed by the disease [ECO2011].

Most prevalent cancers include breast, prostate, lung and colorectal cancers (see Figure 1.1). Their prognosis can vary strongly with cancer type: while some cancer sites (prostate, breast) show a rate of relative survival above 90%, others (lung, liver, pancreas) have a very poor survival rate, typically below 25%. On average, one in every three patients diagnosed with cancer dies because of it [ECO2011].

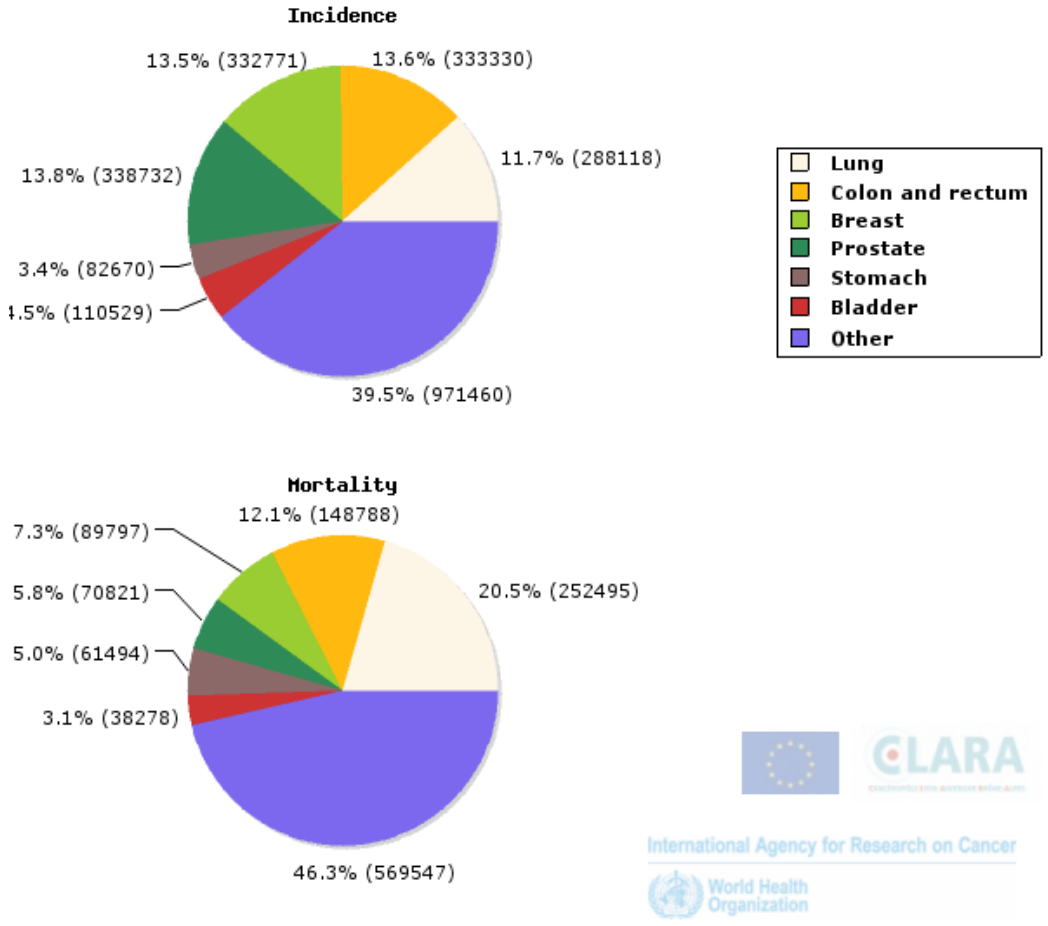

Figure 1.1. Absolute cancer incidence and mortality at the 27-EU, year 2008. (Source: European Cancer Observatory, http://eu-cancer.iarc.fr)

Malignant tumours involve an uncontrolled growth of cells, which invade surrounding tissues and ultimately spread throughout the body. Cancer treatments aim to eliminate all the malignant cells while minimizing the damage to the surrounding healthy tissues. Different

strategies are used, often combined, to achieve that purpose. Any cancer treatment is a compromise between achieving the highest possible TCP (Tumour Control Probability) and minimizing the Normal Tissue Complication Probability, or NTCP.

The three pillars of cancer treatment are: surgery, chemotherapy (including immunotherapy), and radiation therapy. The latter can be, in turn, subdivided into internal and external. Internal radiotherapy, or brachytherapy, consists of the transient insertion of radioactive sources into the patient body, in such a way that the dose from the ionizing radiation released in the radioactive decay is maximized at the tumour site while minimized in the surrounding healthy tissue. External radiotherapy refers to the selected irradiation of the patient body with beams of ionizing radiation. Traditionally, the most common beam modalities used for external radiotherapy are photons and electron beams. These modalities will be referred to as "conventional radiotherapy". However, the pioneering work carried out in the 1950s by Tobias and Lawrence at Berkeley, CA, [TOBIAS1952] after the proposal by Wilson [WILSON1946] opened up a new bunch of possibilities, and since then, treatments have been carried out with protons, pions, neutrons, and several light ions.

The distinctive feature of particle therapy, as opposed to conventional photon therapy, resides in the ballistics of the projectiles. As shown in Figure 1.2, while photons deposit most of their energy in the first centimetres of the tissue, protons and carbon ions present a pronounced peak at a deeper point. This peak is called the *Bragg Peak*. The position at which it appears can be controlled by tuning the energy of the particles, which makes them a perfect candidate for external beam radiotherapy. More details on the distinctive physics of particle therapy are given in section 2.1.

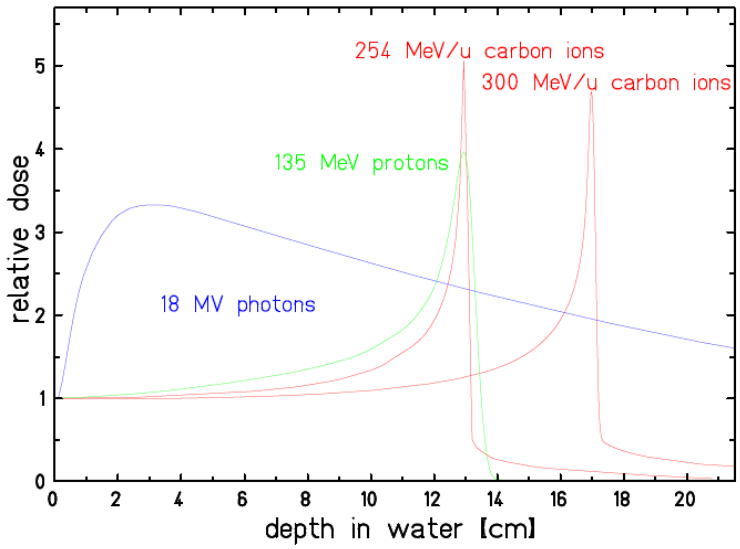

Figure 1.2. Dose profiles of various particles
(Source: [HAETTNER2006] with data from U. Weber)

Radiotherapy (including all its modalities) is involved in the treatment of at least 40% of the patients cured from cancer worldwide, usually in combination with other modalities [DOSANJH2008].

As of May 2011, more than 84,000 patients had been treated with particle therapy, out of which about 74,000 were treated with protons, 7,000 with carbon ions, and the rest with alpha particles and other light ions [PTCOG2011].

1.2. Particle Therapy in Europe: ENLIGHT and PARTNER

In a complex and cutting-edge technology such as particle therapy, it is vital to achieve a close cooperation between the scientific, industrial and the medical communities. It is also necessary to develop strong links between institutions, in order to push together for a common target, of a better, more reliable and cheaper therapy. With these goals, the ENLIGHT network (http://enlight.web.cern.ch) was founded in 2002 to join the European particle therapy community, with more than 150 researchers from more than fifty European Universities and research Institutes. Under the umbrella of ENLIGHT, the European Commission funds, through the FP7 program, several programs addressing different aspects of scientific development, such as cooperation, training, and dissemination of results.

One of these ENLIGHT child programs is PARTNER (http://partner.web.cern.ch), acronym for Particle Training Network for European Radiotherapy, which is defined as *"an interdisciplinary, multinational initiative, which has the primary goal of training researchers who will help to improve the overall efficiency of ion therapy in cancer treatment, and promote clinical, biological and technical developments at a pan-European level, for the benefit of all European inhabitants"*. The network has hosted more than a dozen of courses in the period 2009-2012 and sponsors the research of 25 PhD students and post-doc fellows at several universities, research institutes and industrial partners across Europe. The work leading to this Ph.D. thesis has been sponsored by the PARTNER network, in cooperation with Siemens Particle Therapy.

1.3. Particle Therapy Centres in Europe

After its birth in the 1950s, particle therapy has spread slowly throughout the world, mostly in research facilities and reference national medical centres. In Europe, proton therapy centres for deep-seated tumours are in operation in Orsay (France), Munich (Germany), Uppsala (Sweden), and Villigen (Switzerland); several other research and hospital-based facilities treat eye melanomas with low energy proton beams, and a few more proton centres are currently under construction. Moreover, the experience with carbon ion beams gathered at HIMAC (Chiba, Japan) and GSI (Darmstadt, Germany) paved the way for new, mixed proton and carbon ion facilities: HIT (Heidelberg, Germany) treated its first patient in the fall of 2009, and CNAO (Pavia, Italy) started clinical operation (so far proton only) in the fall of 2011. Moreover, Siemens Particle Therapy has recently finished commissioning a new mixed centre in Marburg (Germany), and another two centres are planned in France (Centre Etoile, near Lyon) and Austria (Med-AUSTRON, close to Vienna).

The experimental work presented in this thesis was carried out mostly at the Heidelberg Ion-Beam Therapy centre (HIT), with some measurements taking place also at the Siemens Simulation and Test Centre in Marburg (STCM).

1.3.1. Heidelberg Ion-Beam Therapy Centre (HIT)

The promising results of the clinical trials which were started at GSI Helmholtzzentrum für Schwerionenforschung (http://www.gsi.de) in 1997 [SCHULZERTNER2004] led to the construction of a hospital-based hadrontherapy facility, with the capability to treat patients with proton and carbon ion beams. The facility is part of the Heidelberg University Hospital, with partnerships with the German Cancer Research Centre (DKFZ) and GSI, with the latter being in charge of the accelerator system. Siemens Particle Therapy provided the irradiation equipment, patient positioning systems, imaging, control and IT solutions (e.g., control system, treatment planning system) for the centre. Construction of the facility started in 2004, the first patients were treated in November of 2009, and more than 600 patients had been treated in the first two years of operation [HIT2011].

A scheme of the centre is displayed in Figure 1.3. The accelerator solution is a combination of two ion sources, a linear accelerator, which accelerates particles from 8keV/u to 7MeV/u, and a synchrotron to bring the beam up to the nominal energies, ranging between 90 and 430 MeV/u. The high energy transport line guides the beam into the caves: two horizontal treatment rooms and the worldwide first rotating heavy ion gantry, as well as research and quality assurance (QA) cave [HABERER2004]. All rooms use active scanning to deliver the dose to the patients, as it will be explained in more detail in section 2.3.2.

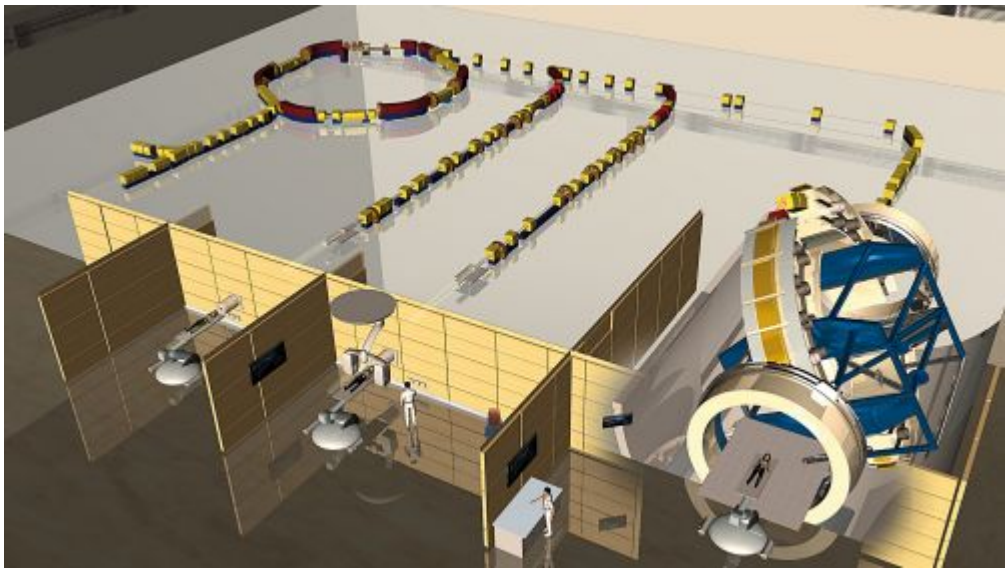

Figure 1.3. Schematic view of the HIT facility
(Source: http://www.klinikum.uni-heidelberg.de)

1.3.2. Siemens Simulation and Test Centre, Marburg

In summer 2007, the medical care company RKA (Rhön-Klinikum AG, http://www.rhoen-klinikum-ag.com) started construction of a particle therapy facility in Marburg, Germany. Siemens was the supplier of all the technology: accelerator, beam transport and monitoring system, patient positioning, imaging, treatment planning, and IT infrastructure.

However, business decisions led in July 2011 to a change of status of the facility, which was acquired by Siemens as a simulation and test centre for particle therapy technology [RKA2011]. The layout is very similar to that of HIT (see Figure 1.4), with three horizontal and one vertical treatment rooms, without gantry. Two of these rooms were commissioned in November 2011 and could start patient treatment at any time, whereas the commissioning of rooms 3 and 4 is scheduled for 2012.

More technical details about the facility can be found in [GRÜBLING2009].

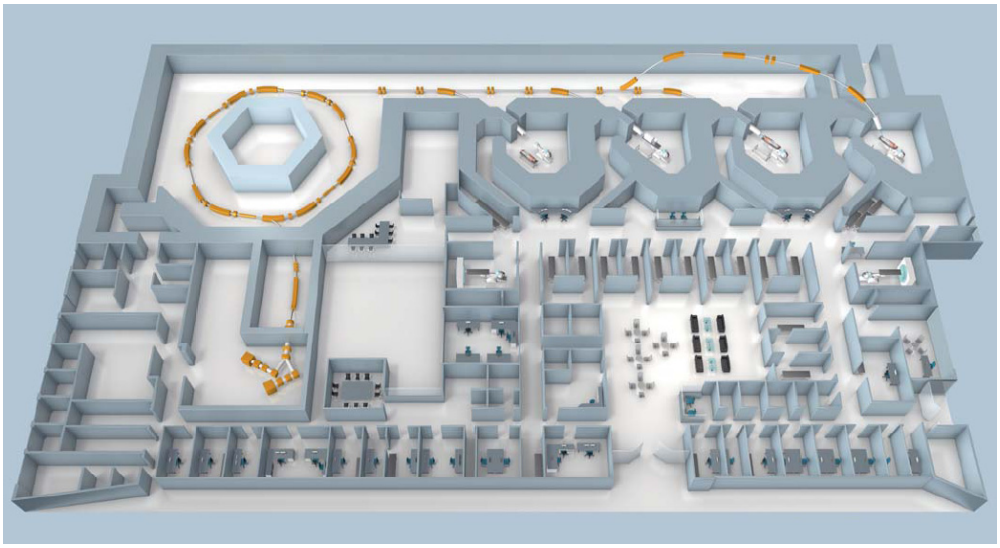

Figure 1.4. Layout of the Siemens Particle Therapy Simulation and Test Centre, in Marburg (Source: http://www.medical.siemens.com)

1.4. Reference dosimetry and international standards

The effects of ionizing radiation are related to radiation dose. For conventional radiotherapy, dose is prescribed in terms of absorbed dose to water, in units of Gray (J/kg). For particle beam radiotherapy, dose prescription is done in terms of photon iso-effective dose, but absorbed dose to water is still required for the QA process, and in order to compare results for different patients, independently of the models used to estimate biological effectiveness [KARGER2010].

International standardization organizations have compiled protocols and codes of practice based on the state of the art in different facilities. The International Agency of Atomic Energy (IAEA) published in 2000 a compilation of dosimetry standards for external beam radiotherapy (TRS-398) including protocols for protons and carbon ions [IAEA2000], and the International Commission on Radiation Units and Measurements (ICRU) has released a report (ICRU Report 78) on "Prescribing, Recording and Reporting" proton therapy [NEWHAUSER2009], and a similar one on carbon ion therapy is in preparation.

Since the IAEA recommended in TRS-398 to perform reference dosimetry of particle therapy with ionization chambers, it has become the standard procedure [JAKEL2004,

TORIKOSHI2007, LIN2009, GILLIN2010]. Ionization chambers show a high accuracy and reproducibility in their measurements, and they are relatively easy to handle and cost-effective. However, their main disadvantage is that they require a good number of corrections for deviations from calibration conditions, some of them not yet fully understood in exposure to ion beams.

Ionization chambers are used not only for reference dosimetry, but also for a number of daily QA measurements, and in the treatment plan verification which is done before the irradiation of a new patient plan [KARGER1999].

1.5. Scope of the thesis

The objective of our project was to use all available tools, including experimental measurements and Monte Carlo simulations, to reduce uncertainties in the dosimetry of absorbed dose for particle therapy. The IAEA [IAEA2000] estimates overall uncertainty at about 2% of the dose for proton beams, and 3% for carbon ion beams, which are high compared to the 1% of photon beams. This uncertainty can be reduced by a deeper understanding of the beam quality correction factors used in ionization chamber dosimetry. In particular, the biggest contribution arises from the uncertainty in the ratio of stopping powers between water and air ($s_{w,air}$).

Detailed work on this topic has been published in the last years [GEITHNER2006, PAUL2007, HENKNER2009, LUHR2011], predominantly with a calculation approach based on Monte Carlo simulations. The studies reported so far in the literature were consistent with each other, but all of them showed a strong dependence on the choice of the used stopping power tables. This is particularly due to the still missing consensus on the values of the ionization potential for air and water. The approach pursued in this work was to partially overcome this lack of consensus with experimental measurements, which were then used to improve computational approaches based on Monte Carlo simulations. For the latter, the choice was made to use the Monte Carlo code FLUKA [FASSO2005, BATTISTONI2007], which had already been used with satisfactory results by HIT colleagues in the scope of particle therapy [PARODI2009]. We investigated the variation of the water-to-air stopping power ratio with the penetration depth, and assessed the impact of the investigated effects in real patient plans, simulating plan verification with ionization chambers.

The most relevant contributions from this thesis are the experimental data presented in section 5.3, which could be used to narrow the uncertainties in the current international recommendations on dosimetry for light ions, and the description of the variation of $s_{w,air}$ with the residual range in a treatment field, presented in section 5.5 and analyzed in detail in chapter 6.

CHAPTER 2 Basics of particle therapy

2.1. Physics of particle therapy

The favourable dose deposition of ion beams for radiotherapy, presenting a peak which can be used to deliver conformal dose to a tumour while sparing surrounding tissues (see Figure 2.1), is determined by the characteristics of electromagnetic and nuclear interactions of the projectiles with the target medium. This section presents the basics of such physical interactions, stressing the aspects which have the largest impact on therapy.

2.1.1. Stopping of charged particles

The energy loss of a charged particle passing through matter is almost completely due to electromagnetic interactions with the atoms in the medium, while nuclear interactions play a minor role, as covered in section 2.1.5. The biggest contribution to the energy loss is caused by the medium atomic electrons (*electronic stopping*), with a very small fraction being attributable to the positive cores (*nuclear stopping*[1]), as shown in Figure 2.2.

For example, for a proton beam with an energy of 100 MeV, corresponding to a range of 7.7 cm in water, the nuclear stopping represents less than 0.05% of the stopping power of the medium [ICRU1994], and it becomes dominant only for very low energies, of the order of 10 keV/u [SCHARDT2010].

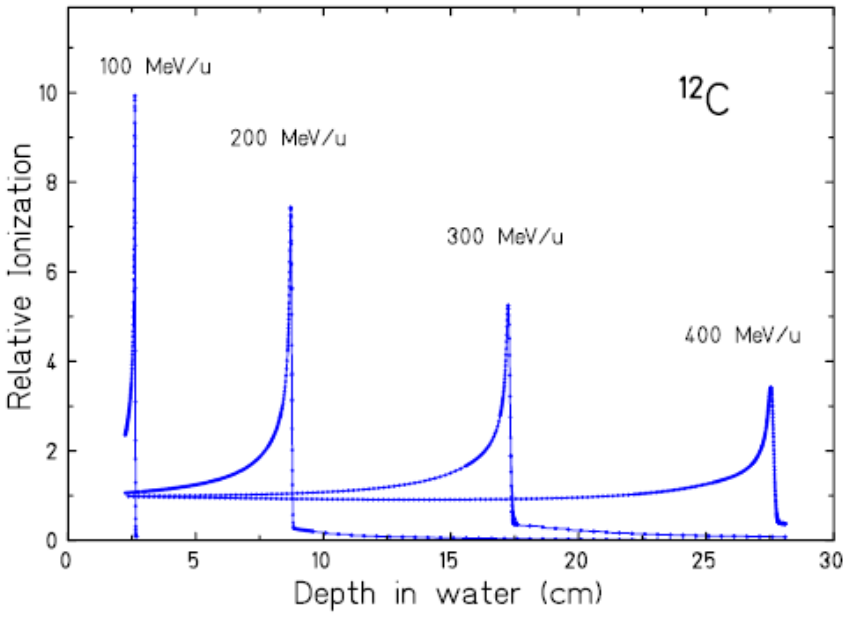

Figure 2.1. Experimental depth dose distributions of ^{12}C ions and in water for different initial energies (Source: [SCHARDT2010])

[1] The term *nuclear stopping* is often used to design the electromagnetic interactions with the atomic nuclei and does not relate to the interactions via the nuclear strong force.

The stopping power in a medium, defined as the average ion energy loss per unit path length [ICRU1994], is described by the Bethe-Bloch equation, proposed in its initial form by Bethe [BETHE1930] and Bloch [BLOCH1933]. A detailed review of this equation, including all the relevant corrections and modifications, can be seen in [ZIEGLER1999].

The equation is considered to be valid above approximately 1 MeV/u [ICRU1994]. It expresses the mass stopping power of a medium, in terms of the stopping number $L(\beta^2)$, as

$$\frac{S}{\rho} = \frac{4\pi r_e^2 m_e c^2}{\beta^2} \frac{1}{u} \frac{Z}{A} z^2 L(\beta^2), \tag{2.1}$$

where r_e is the classical electron radius, $m_e c^2$ is the electron rest mass energy, β is the particle velocity as a fraction of the speed of light, u is the atomic mass unit, Z/A is the atomic to mass number ratio of the target medium, and z is the atomic number of the projectile.

The stopping number, $L(\beta^2)$, is usually expressed as a power series of z up to second order, $L(\beta^2) = L_0 + zL_1 + z^2L_2$. The complete expression for the stopping number can be written as

$$L(\beta^2) = \left[\left(\frac{1}{2} \ln \frac{2m_e c^2 \beta^2 \Delta E_{\max}}{1-\beta^2} - \beta^2 \right) - \ln\langle I \rangle - \frac{C}{Z} - \frac{\delta}{2} \right] + zL_1 + z^2 L_2 \tag{2.2}$$

.

- $f(\beta^2)$, representing the first expression in brackets, accounts for most of the dependence of the stopping number with the particle velocity. The quantity ΔE_{max} is the largest possible energy loss in a single collision. It can be approximated to $\Delta E_{max} \approx 2m_e c^2\beta^2/(1-\beta^2)$ with an accuracy better than 0.1 % [ZIEGLER1999], which yields a simplified expression for $f(\beta^2)$,

$$f(\beta^2) = \ln \frac{2m_e c^2 \beta^2}{1-\beta^2} - \beta^2 . \tag{2.3}$$

- ln <*I*>, logarithm of the mean ionization potential of the medium, encloses most of the dependence on the target material. The unit of *I* must be coherent with that of $m_e c^2$.

- C/Z, shell correction term, accounts for the internal structure of the target atoms, playing a role only for low energies, in the order of a few MeV/u.

- δ/2, density correction factor, accounts for polarization effects in solid media, and is only important for ultrarelativistic energies, above 1 GeV/u.

- zL_1, Barkas first-order correction, models the difference between negatively and positively charged projectiles, with decreasing importance with increasing particle energy.

- z^2L_2, Bloch second-order correction, only relevant at very low energies, models ion-electron interactions with a high impact parameter.

An example of the relative importance of the corrections is shown in Table 2.1, with the different contributions to stopping power of aluminium for protons. The energies relevant for particle therapy are in the range from a few tens up to hundreds of MeV/u.

Percent contribution towards Stopping Number L						
Proton Energy (MeV)	*L_0*	*$f(\beta)$*	*Shell+ ln<I>*	*$\delta/2$ Density Corr.*	*L_1 Barkas Corr.*	*L_2 Bloch Corr.*
1	95.95	309.5	- 207	- 0.0004	5.239	-1.187
5	98.84	227.7	- 126.1	- 0.0007	1.308	-0.1479
10	99.25	208.2	- 107.3	- 0.0016	0.8124	-0.0632
50	99.7	180.5	- 80.48	- 0.0133	0.3116	-0.0101
100	99.79	173.2	- 73.15	- 0.0388	0.2141	-0.0049
1,000	99.93	157.8	- 56.85	- 0.9614	0.0661	-0.001

Table 2.1. Contribution to stopping power for protons in aluminium, in percent, of the different terms of the Bethe-Bloch expression (equation (2.2)). Source: [ZIEGLER1999]

In the clinical energy range, the biggest contribution (and the biggest source of uncertainty) originates from the *ln <I>* term. Although the values of *I* can be calculated theoretically (from atomic structure in elements, and using the so-called *Bragg's additivity rule* [ICRU2005] for compounds), the related uncertainties are too high and it is common practice to adjust *I* to the experimental data, where it is available, and to interpolate it where not [GOTTSCHALK2004].

Since $L(\beta^2)$ varies slowly with β^2, the term on $1/\beta^2$ from equation (2.1) dominates in the energy region of therapeutic interest (see Figure 2.2). At high velocities, the atoms lose their electrons and the projectile charge is equal to the atomic charge number Z. At lower velocities (for light ions below about 10 MeV/u [SCHARDT2010]) the mean charge state decreases due to the interplay of ionization and recombination processes and Z in equation (2.1) has to be replaced by the effective charge Z_{eff}, which can be described by the empirical formula [BARKAS1963]

$$Z_{eff} = Z\left[1 - \exp\left(-125\beta Z^{-2/3}\right)\right]. \tag{2.4}$$

The maximum energy-loss rate determines the position of the Bragg peak. It is reached at a projectile velocity of $v_p \approx Z^{2/3} v_0$, where $v_0 = e^2/\hbar$ is the Bohr velocity, and occurs at a specific energy of about 25 keV for protons and 350 keV/u for carbon ions.

An extensive analysis of the physical processes which influence the stopping of charged hadrons in matter can be consulted in the ICRU Reports 49 and 73 [ICRU1994, ICRU2005].

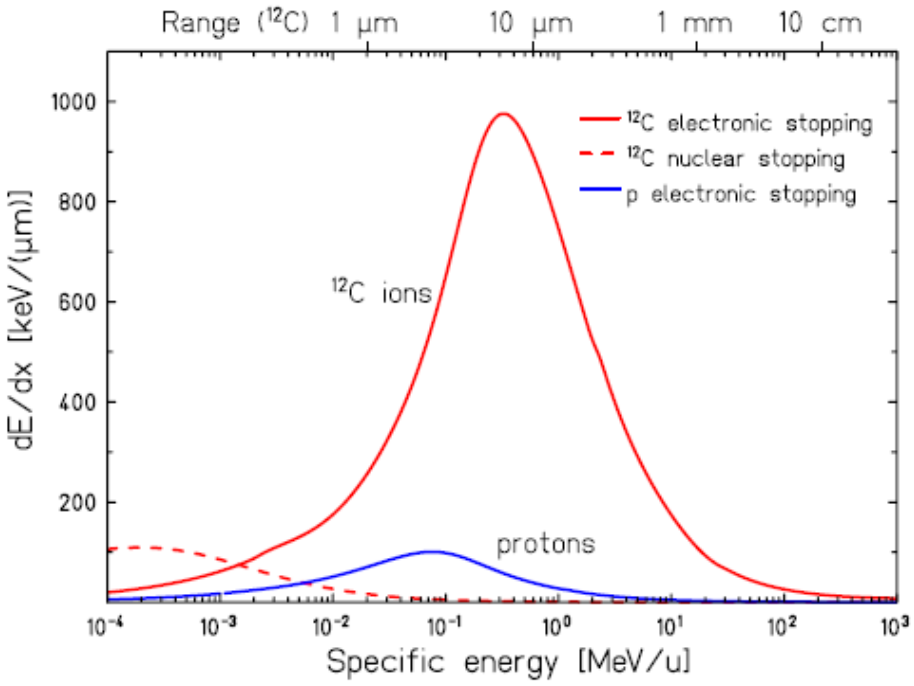

Figure 2.2. Stopping power of ^{12}C ions and protons in water. The top axis label additionally shows the corresponding range in water for carbon ions (Source: [SCHARDT2010])

2.1.2. Range of particles in matter

Given the stopping power of a charged particle in a medium, the pathlength P of a particle with kinetic energy T can be simply calculated by numerical integration [JANNI1982],

$$P(T) = \int_T^0 \left(\frac{dE}{dx} \right)^{-1} dE \,. \tag{2.5}$$

This procedure is called CSDA, or continuous slowing down approximation. For heavy charged projectiles it is nearly the same as the mean range R, the average traversed absorber thickness. The reason for this is that heavy ions are very little scattered and travel almost on a straight line. The ratio between range and pathlength is called *detour factor*, and it takes values above 0.99 for all clinical beams [ICRU1994, ICRU2005, SIGMUND2009].

Since energy loss occurs via successive ionizations, it is affected by statistical fluctuations, which leads to the fact that two particles with exactly the same initial energy will most certainly differ slightly in their penetration depth. This effect is called *range straggling*, and it causes a broadening of the peak in the depth dose distribution, even for purely monoenergetic beams (see Figure 2.1).

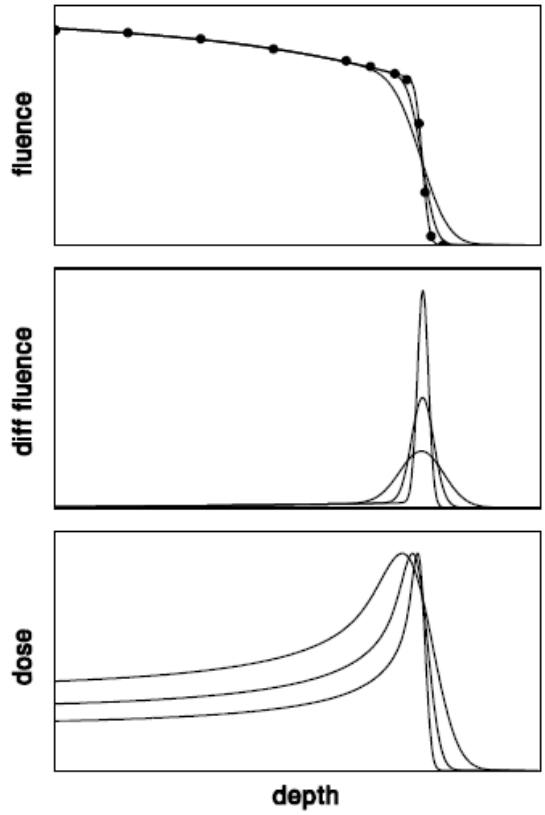

Figure 2.3. Possible measurements of fluence, differential fluence and dose distribution of three proton beams of the same energy with different initial energy spreads, to illustrate R = d_{80} (source: [GOTTSCHALK2004])

The fluctuations in energy loss follow a Gaussian distribution for a sufficiently thick absorber [SCHARDT2010]. The variance of the range straggling σ_R^2 is related to the variance of the energy losses σ_E^2. The width of the range straggling can be expressed by

$$\sigma_R = \frac{R}{\sqrt{m}} f\left(\frac{E}{mc^2}\right), \tag{2.6}$$

where m and E are the projectile's mass and energy and f is a slowly varying function which accounts for the medium dependence [ROSSI1952]. The $1/\sqrt{m}$ dependence causes protons to have a higher straggling than light ions, by a factor of 3.5 with respect to carbon ions.

In an actual beam, the range is the distance at which half of the initial particles have stopped [GOTTSCHALK2004]. Such a definition is based on the knowledge of the particle fluence, but it is the dose distribution what is most often measured or characterised. The work by [BORTFELD1997] relates the two concepts via the expression $R_0 = d_{80}$, which means, the mean range equals the distal 80% point of the Bragg peak. Figure 2.3 shows how this applies for different beam energy spreads.

The word "range" is often used in the radiotherapy environment in different contexts, each time referring to different concept. Usually, the clinical prescription of extended dose distributions is done in terms of d_{90} (point at which the dose falls at 90% of its maximum

value), which is sometimes called *clinical range*. In dosimetry, the so-called *practical range* is commonly used, referring to d_{10} [IAEA2000]. Different definitions are used for convenience in [KEMPE2008] and [LUHR2011]. In conclusion, care needs to be taken when working with particle ranges.

It is useful to establish a power law relation between ranges and initial energies of particle beams, which has the form $R_0=\alpha \cdot T^{\beta}$ [BORTFELD1997]. As shown in Figure 2.4, penetration depths of up to 40cm are obtained with energies of approximately up to 250 MeV for proton beams, and up to 500 MeV/u for carbon ion beams.

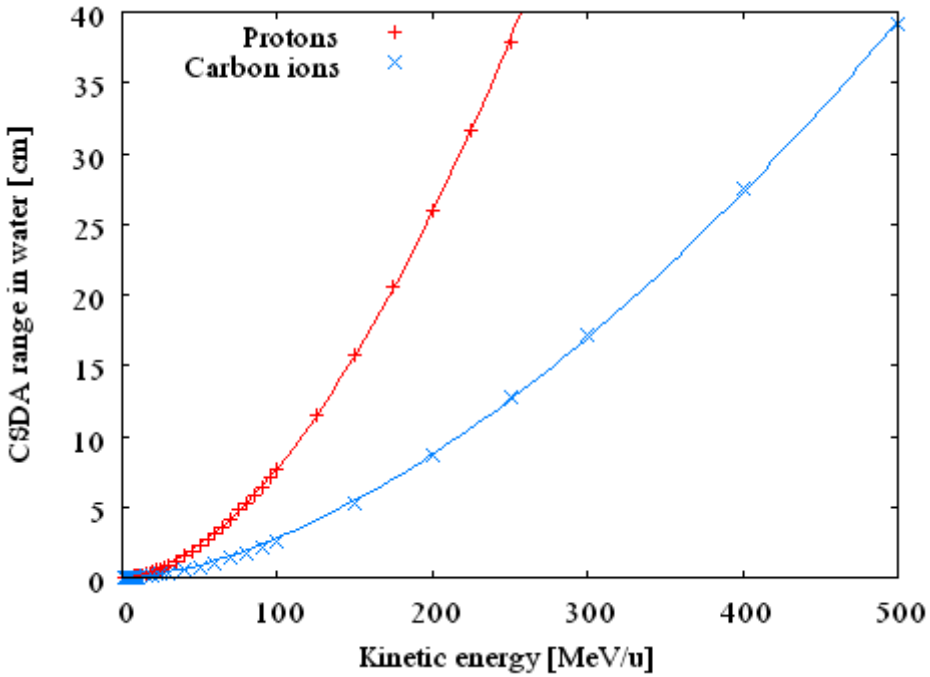

Figure 2.4. Range-energy relationship for protons and carbon ions in water. Data from [ICRU1994] and [SIGMUND2009] fit to $R_0=\alpha \cdot T^{\beta}$ with $\beta=1.74$ for protons, and $\beta=1.65$ for carbon ions.

2.1.3. Multiple Coulomb scattering

A beam of charged particles traversing a medium tends to "open up", increasing its section and angular divergence as it travels. This process is a consequence of the particle *multiple scattering*, i.e., the result of a sum of discrete individual Coulomb scattering events by atomic nuclei. By basic kinematics, the ratio of masses between the incident ion and the deflecting target determines the magnitude of the scattering. For this reason, atomic electrons are basically irrelevant when it comes to scattering of ion beams, since their mass is at least three orders of magnitude lower than that of the incident ions. Also for this reason, heavier ions suffer from less scattering than protons (see section 2.1.3), and therefore, they have a better lateral penumbra for clinical use.

The basics of the multiple scattering theory were set by Molière [MOLIÈRE1947, MOLIÈRE1948], who first studied the single scattering in the Coulomb field of a nucleus (Rutherford scattering), and then went on to analyse the combined, statistical effect of

several nuclei. Bethe [BETHE1953] and Fano [FANO1954] contributed with some corrections to Molière's model, ant the resulting theory is regarded as complete and valid [GOTTSCHALK1993].

A first approximation would assume that multiple scattering can be computed by quadratically adding up the single scattering produced at each step, using the Central Limit Theorem. This approach yields a Gaussian distribution for the scattered angle. However, in order to apply such Theorem, the single scattering contributions must be *small* enough (see [GOTTSCHALK1993] for a more detailed explanation), which does not apply for Rutherford scattering.

Molière's theory replaces the Gaussian single parameter by a more complicated set of parameters which depend on the scatterer and on the kinematics of the incident particle. The resulting angular distribution is a three term power series, the first of which is a Gaussian. For small angles, the function can be approximated by a Gaussian distribution, which is not directly the first term of the series. Some approximate formulas have been presented (cf. work from Hanson, Highland, Lynch and Dahl, among others). We present here the most modern one, which has been found to agree within 2% with the experimental data [GOTTSCHALK1993]. A complete summary of the different Gaussian approximations to Molière's theory, including a comprehensive list of references, can be found at [GOTTSCHALK2004].

Lynch and Dahl [LYNCH1991] suggest that the scattering angle distribution can be expressed by a Gaussian function,

$$f(\theta,\phi)\theta d\theta d\phi = \frac{1}{2\pi\theta_L^2} e^{-\frac{1}{2}\left(\frac{\theta}{\theta_L}\right)^2} \theta d\theta d\phi, \tag{2.7}$$

where the mean scattering angle, θ_L, is expressed by Highland's formula [HIGHLAND1975] with revised constants,

$$\theta_L = \frac{13.6\,\text{MeV}}{pv} z\sqrt{\frac{L}{L_R}}\left[1+0.088\log_{10}\left(\frac{L}{L_R}\right)\right], \tag{2.8}$$

where p, v and z are the momentum, velocity and charge of the projectile and L and L_R are respectively the target thickness and the radiation length. The formula is valid for thin scatterers, but it can be applied to thick targets by properly integrating over infinitesimal targets in quadrature.

2.1.4. Linear Energy Transfer and track structure

Fast charged particles deposit energy in matter via ionizations. Those ionizations are excitations of target electrons, which, if given enough kinetic energy, can be also ejected away from their atoms. If they are energetic enough, they will, in turn, cause further ionizations. These energetic secondary electrons are called *delta rays* and form a

characteristic track structure as they are ejected surrounding the path of the primary particle. Their kinetic energy is usually very low: the most probable energy loss in individual proton collisions is of the order of 20 eV, and in light elements, 80% of the collisions cause losses lower than 100 eV [ICRU1994]. Since part of that energy has to be spent to overcome the binding energy, most delta electrons have a kinetic energy of only a few eV. Note that an electron of 10 keV has a range in water of only a 2.5 μm (see Figure 2.5). This feature will be considered again in the followings sections when discussing the appropriate transport thresholds to use in Monte Carlo simulations of ion beams.

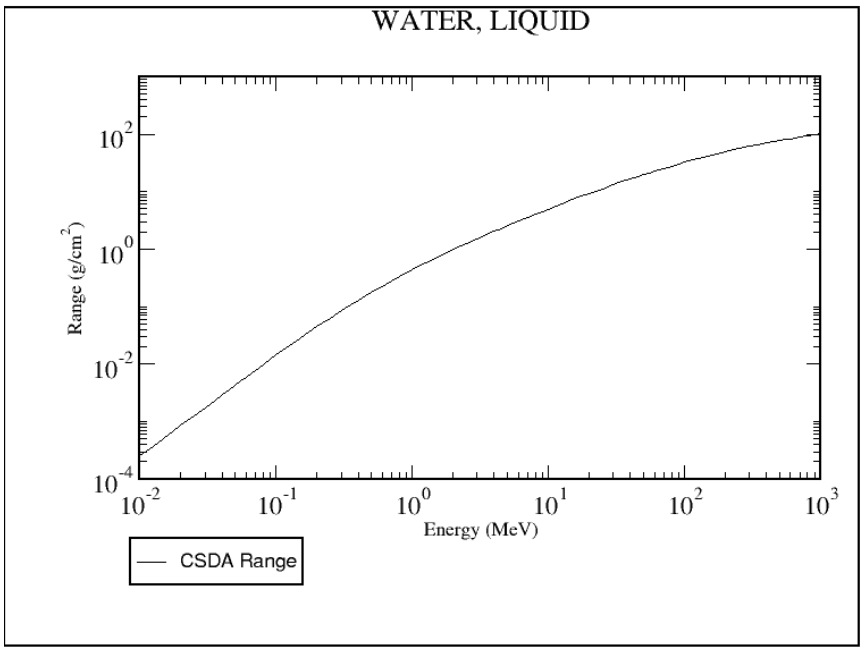

Figure 2.5. CSDA range of electrons in water (from NIST, ESTAR database [BERGER2005])

Due to the aforementioned spatial pattern of the energy transferred to the electrons via ionization processes, the transverse dose profile follows a $1/r^2$ distribution, causing a track structure which is the basis for the biological models [SCHOLZ1996] described in section 2.2.

There can be, however, a few delta electrons with a sufficient kinetic energy to travel a non negligible distance in matter, getting away from the track of the primary ion. The energy which they deposit can be difficult to account for, since it is carried away from the point of interaction. Because of this, the concept of *restricted stopping power* was introduced, which refers to the stopping power (as described in section 2.1.1), but including only the collisions where an energy lower than a certain threshold is transferred. The concept is very useful, for example, in Monte Carlo simulations, where some collisions deposit energy locally (through the restricted stopping power), and other collisions eject a delta electron, which is explicitly transported.

When talking about dose deposition, the concept of LET (*Linear Energy Transfer*) is preferred to the concept of stopping power. Although they denote basically the same

quantity, the former puts the focus on the energy absorbed by the medium, while the latter refers to the slowing down of an incident projectile. LET, generally expressed in MeV/mm or keV/um, is closely related to the biological effects caused by ionizing radiation.

2.1.5. Nuclear interactions and fragmentation

In addition to electromagnetic interactions, hadrons experience nuclear interactions mediated by nuclear strong and weak forces.

According to ICRU Report 63 [ICRU2000], nuclear interactions fall into two categories: elastic, and non-elastic. Elastic nuclear interactions occur when a projectile is scattered by a target nucleus and they both keep their internal state constant (the total kinetic energy is conserved). Non-elastic interactions are those which do not conserve the kinetic energy: the target nucleus or the projectile (or both) either undergoes fragmentation or changes its quantum state. The interactions where the ion species conserve their identity before and after the collision (changing only their quantum state) are called *inelastic*.

Non-elastic interactions mediate most of the processes with influence on particle therapy. They occur normally as a two step process (see Figure 2.6). In first place, the two nuclei overlap and form an excited system, which is later de-excited as fragments leave the system or change their internal quantum state.

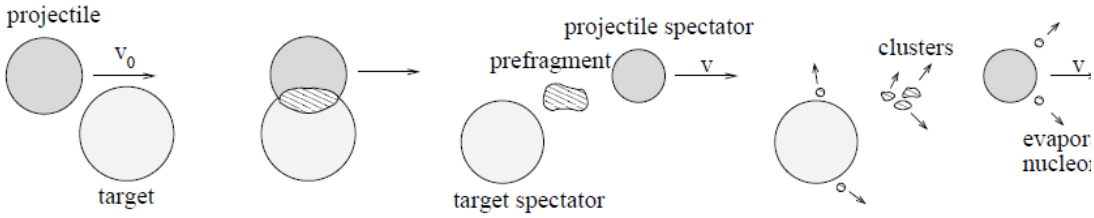

Figure 2.6. Fragmentation as a two step process (source: [HAETTNER2006])

These nuclear interactions modify the particle fluences: as a beam travels through matter, the *primary particles* undergoing nuclear non-elastic interactions will be replaced by lighter fragments, extract ions from the target material, and build up neutrons and other secondaries. Figure 2.7 shows the build up of different fragments from a carbon ion beam.

The numbers which characterize those interactions are the charge-changing and neutron emission cross sections. The cross sections for protons are available in [ICRU2000], while data for other ions, such as carbon ions, are scarcer, and therefore its associated uncertainties are higher [BÖHLEN2010].

Nuclear effects are fairly visible in a depth dose distribution. For primary particles heavier than protons (see Figure 2.7 and Figure 2.10) the characteristic tail is caused by light fragments, mainly protons, deuterons and alpha particles. Projectile fragments retain most of the velocity and mass of the primary particle, but because of their lower charge, their electromagnetic interaction with the target is weaker, so they can reach beyond the range of the primaries, forming a tail.

A precise knowledge of the fluence of different species is important to model the effects of charged particle beams. Different ion species deposit energy in different ways, and thus originate different radiobiological effects (cf. section 2.2) or detector response. Moreover, some calculations involved in particle beam dosimetry, which is the main topic of this thesis, also use intensively the fluence distributions of several radiation fields, as calculated by Monte Carlo simulations.

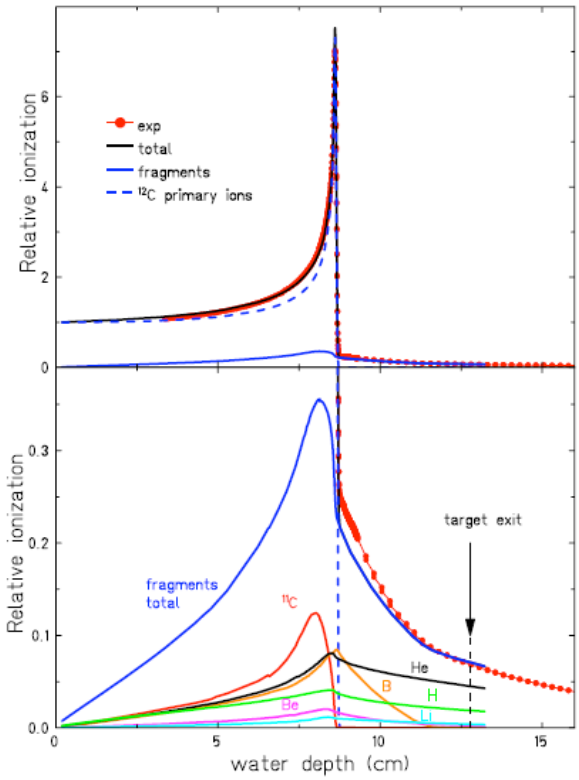

Figure 2.7. Depth dose distribution of a 200 MeV/u carbon ion beam. Black solid line represents the full dose, with the blue dashed and solid lines depict the contribution from primary ions and fragments (as calculated with Monte Carlo code PHITS [NIITA2006]). The bottom image shows a zoom of the dose contribution from the main fragments (source: [GUNZERTMARX2008])

2.2. Radiobiology and particle therapy

The goal of radiotherapy is the eradication of tumoural cells with radiation, and cell killing is achieved by DNA damage. The killing power of a certain radiation type depends on the type and intensity of the induced lesions. Here the terms single strand break (SSB) and double strand break (DSB) become relevant. SSBs are lesions where only one strand of the double DNA helix is damaged, so they are easy to repair by cellular DNA repair mechanisms. In DSBs, on the contrary, both strands are severely injured, which makes repair a lot more difficult, if not impossible. Most cell killing is, therefore, achieved by causing clustered DSBs in the DNA.

Damage to DNA can be *direct* (if the ionizing particle causes the DNA damage), or *indirect* (when the ionizing particle creates a free radical which, in turn, provokes a DNA damage). Indirect damage is often reduced in a cell environment with suppressed oxygen supply (hypoxia) which typically yields a larger radioresistance of the irradiated tissue.

For therapeutic purposes, it is extremely important to understand the survival of cells when irradiated with a certain dose. The commonly accepted relation between probability of cell survival S and absorbed dose D is the linear-quadratic (LQ) model, which is expressed

$$S(D) = exp\ (-\alpha D - \beta D^2). \tag{2.9}$$

In the expression above, α and β are parameters (in units of Gy^{-1} and Gy^{-2}, respectively) which depend on the nature of the cells. The ratio α/β is considered as a characteristic number of tissues which indicates their radiosensitivity.

In order to compare the effect of photon radiotherapy with charged particle radiotherapy, the concept of RBE (radiobiological effectiveness) was introduced, as the ratio of photon dose to the dose with any other particle to produce the same biological effect (see Figure 2.8). The actual value of the RBE will depend on the chosen endpoint, so that when looking at survival we can talk about RBE_{50} (survival of 50%), RBE_{10} (survival of 10%), and so on.

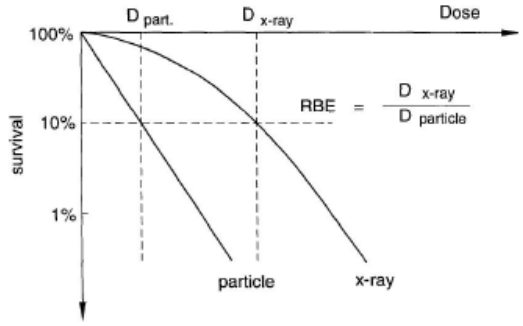

Figure 2.8. Definition of RBE, illustrated for cell survival curves (Source: [KRAFT2000]).

Charged particles have indeed different RBEs at different energies. A high RBE itself is not an advantage (the same effect could be achieved with a higher photon dose); the advantage is a selectively increased RBE in the Bragg peak area over the entrance channel, which can be used to cause more damage in the tumour than in healthy tissue. The RBE concept is also used, in combination with the LQ model, to account for the effect of different treatment fractionation schemes [IAEA2000].

Proton radiotherapy traditionally uses a RBE value of 1.1 (see Figure 2.9, left), although there are studies showing a dispersion of values depending on tissue type (see, for example, [PAGANETTI2002]), and calling for a finer modelling [CARABEFERNANDEZ2011].

In carbon ion therapy, the calculation of RBEs is way more complex, since it varies along the beam path due to differences in LET and particle spectra (see Figure 2.9, right). There

are two approaches to account for the biological effect of carbon ions beams actually used for patient treatments, namely, the GSI approach and the HIMAC approach.

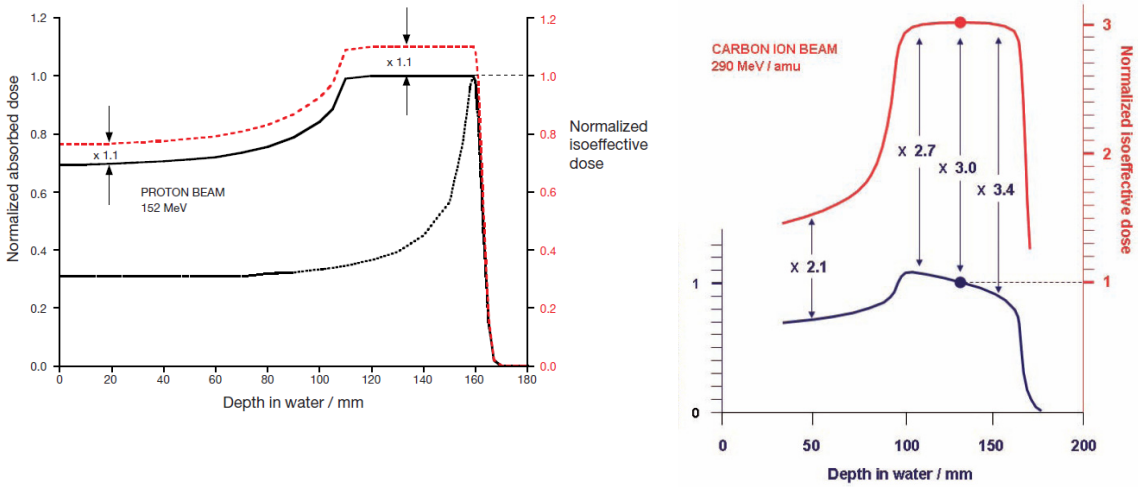

Figure 2.9. Effect of RBE. Biologically equivalent SOBPs (spread out Bragg peaks) constructed by scaling the physical dose with the assumed RBE for protons (left) and carbon ions (right) (source: [IAEA2008]).

In the clinical experience at GSI and HIT, the RBE is computed using the Local Effect Model, which assumes that the damage to cells is primarily caused by δ electrons and, at the nanometre scale of the DNA critical target, there is no difference between δ electrons originated from different primaries. The particular effects are then explained by different local dose distributions. Recently this model was extended to additionally account for correlations of DSBs over larger distances of a few hundred nanometres [SCHOLZ1997, ELSÄSSER2010].

The Japanese approach developed at HIMAC is based on a combination of radiobiological experimentation and a large amount of clinical experience with neutron therapy. A comparison of clinical results obtained with neutrons with those obtained with photons indicated a RBE value of 3.0. The RBEs distribution for carbon ions beams were then linked to those of neutrons after a series of radiobiological experiments with radiation of different LET [KANAI1997].

While the German approach is believed to be more sophisticated and powerful (e.g., in terms of prediction ability), due to the improved modelling, the Japanese one accumulates much more patient experience. There have been attempts to relate both calculation methods [UZAWA2009], but as of today, there is no unique solution to the problem of relating the clinical results gathered with these two approaches.

Among light ion beam therapy, the choice of optimal projectile was not (and is still not) a trivial issue. In addition to the physical properties of the dose distribution (covered in section 2.1.1), the highest gain in the RBE for the Bragg peak area was sought, in combination with the lowest possible OER. The topic was studied in Berkeley in the 1970's, and it was concluded that neon and carbon ions were the most suitable candidates for light ion therapy

[CHU2006]. Also at GSI, radiobiological studies [SCHOLZ2003] pointed to carbon as the most favourable ion species. However, the topic remains open, and a detailed analysis of the physical and biological properties of the ions does not suffice for a final judgement, which will be ultimately supported only by clinical data.

2.3. Practical aspects of particle therapy

2.3.1. Accelerators for particle therapy

The energies required for particle therapy can be achieved with synchrotrons, cyclotrons or linear accelerators. The choice depends on constraints such as the particle type, the desired delivery system, the available space, the cost, etc.

A cyclotron is a compact accelerator which delivers a continuous beam of constant extraction energy at a high intensity. Proton cyclotrons for therapy are available from industry, while no carbon ion cyclotrons providing the required extraction energy have been constructed yet, due to size constraints[2]. However, a ^{12}C cyclotron is projected for the French site ARCHADE [JONGEN2010].

Since the cyclotron produces a beam of a fixed energy, passive systems are used to decrease the beam energy according to the maximum tumour depth. The energy spread is reduced using a spectrometer-type beam line. The beam losses caused by the energy degraders are overcome with a sufficiently high intensity produced by the cyclotron. Synchrotrons are a more complex, but flexible solution. The same synchrotron can accelerate both protons and different species of ions. It is much larger than the cyclotron, and no off-the-shelf solutions are available.

Synchrotrons allow the change of the extraction energy on a cycle to cycle basis: the beam is injected at low energy, then accelerated to the desired energy level and finally extracted. Therefore the synchrotron is ideally suited for fully active beam delivery techniques (see section 2.3.2). The extraction energy is adjusted with the accelerator in discrete steps from one cycle to the next to cover the complete tumour thickness. These energy steps correspond typically to a change of the beam range in tissue in the order of 1-2 mm.

At present, all hadrontherapy facilities with light ion beams are synchrotron-based, and among the protontherapy facilities, most of them use cyclotron accelerators. No linear accelerators have yet been used in hadrontherapy facilities, but in the latest years, solutions based on combined cyclotron-linear accelerators have been investigated [AMALDI2010].

[2] The magnetic rigidity of a particle is defined as the momentum per unit charge (p/q). According to Lorentz's Law, in order to bend a charged particle, the product of the magnetic field times the bending radius has to equal the magnetic rigidity (Br=p/q). Carbon ions of clinical range have more than two times higher magnetic rigidity than protons, which, with a constant magnetic field, would require magnets to be more than two times bigger [BERGER2005].

2.3.2. Choice of projectile

Particle therapy with protons and carbon ions is a reality, with several centres in operation and thousands of patients treated already. However, those are not the only candidate ions for particle therapy treatments: in Berkeley, where the technique was born, patients were treated also with helium, neon, argon and silicon ions [CHU2006], and the HIT facility in Heidelberg is designed to perform treatments not only with protons and carbons, but also with oxygen and helium ions [COMBS2010].

The physical and biological characteristics of a particle beam vary sensibly with the particle species, which can be used in clinical practice to enable the best possible treatment. This is for example illustrated in Figure 2.10, which shows four depth dose distributions for protons and helium, carbon and oxygen ions. It can be noted that heavier particles have a sharper peak and a higher peak to plateau ratio, since they experience less range straggling (see section 2.1.2), but they also have a much more pronounced tail from nuclear fragmentation (section 2.1.5), which introduces a minor unwanted dose beyond the peak. Figure 2.11 shows transversal dose distribution for protons and carbon ions of similar range, illustrating the benefit of reduced multiple Coulomb scattering (carbon ions) to achieve a steeper fall-off of the dose at the border of the tumour region.

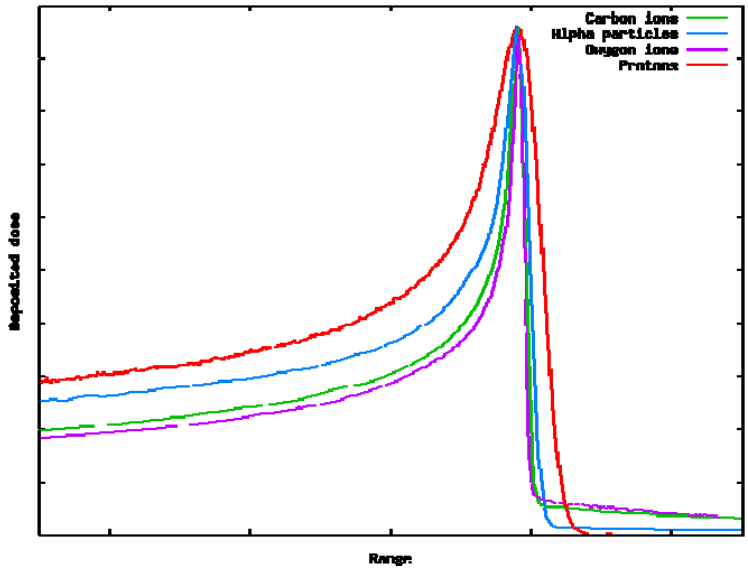

Figure 2.10. Depth dose distributions in water for pure monoenergetic beams of different ions with similar range and initial energy spread. Calculated with the Monte Carlo code FLUKA [FASSO2005, BATTISTONI2007]. The higher straggling of lighter ions, and the pronounced tail of the heavier particles can be clearly appreciated.

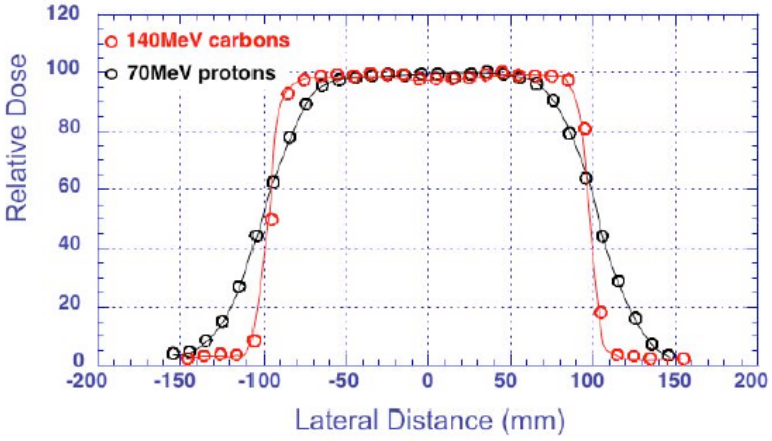

Figure 2.11. The lateral penumbra of a carbon ion beam is much sharper than that of a proton beam (source: [CHU2006]).

2.3.3. Delivering dose to the tumour

Once the charged particles are accelerated to the desired energy, they are transported to the treatment room through a line of bending and focusing magnets. For efficiency reasons, each accelerator normally feeds several treatment rooms. Most proton facilities are equipped with a gantry inside the treatment rooms, which allows bending the beam to hit the patient from arbitrary angles around the centre of rotation. In contrast, since bending magnets for carbon ions have to be quite large[3], in carbon ion treatment rooms the beam is delivered with a fixed angle (generally horizontal, vertical, or at 45º). In fact, only one carbon ion gantry has ever been built, in the HIT facility (Heidelberg, Germany) and it is scheduled to start clinic operation in 2012 [HABERER2004].

Once in the treatment room, the beam is shaped, both in transversal and longitudinal directions, to deliver conformal dose to the tumour. Since response of tissue to radiation is highly non-linear, very high accuracy is desired both in the coverage of the treatment volume and of the healthy tissue.

Two main families of delivery techniques exist (see Figure 2.12): passive scattering and active scanning. The passive delivery systems involve broadening the beam through a compound scattering system which modifies its primary Gaussian lateral distribution, complemented by passive shaping devices to adjust its energy (longitudinal conformation) and lateral distribution. The active scanning starts from a fine and focused (quasi) mono-energetic pencil beam which is deflected by magnetic dipoles to model the desired field.

[3] The magnetic rigidity of a particle is defined as the momentum per unit charge (p/q). According to Lorentz's Law, in order to bend a charged particle, the product of the magnetic field times the bending radius has to equal the magnetic rigidity (Br=p/q). Carbon ions of clinical range have more than two times higher magnetic rigidity than protons, which, with a constant magnetic field, would require magnets to be more than two times bigger [BERGER2005].

There are three problems to be solved independently in order to achieve a conformal dose deposition, and their combined solution can rely on different active, passive or mixed techniques.

First, the beam has to be extended in the transversal direction in order to cover the entire field. This can be achieved by broadening the beam with passive systems (single or double scatterers, see [GOTTSCHALK2004]), or with dipole magnets (using wobbling magnets or as part of a raster scanning technique [HABERER1993, PEDRONI1995]).

Second, the beam profile has to be extended in the longitudinal direction in order to span the complete depth of the target volume (more about the rational for this is explained in section 2.3.4). If the accelerator allows beam extraction at different energies with dynamic intensity modulation, this can be done by constructing the treatment field in a "slice by slice" manner.

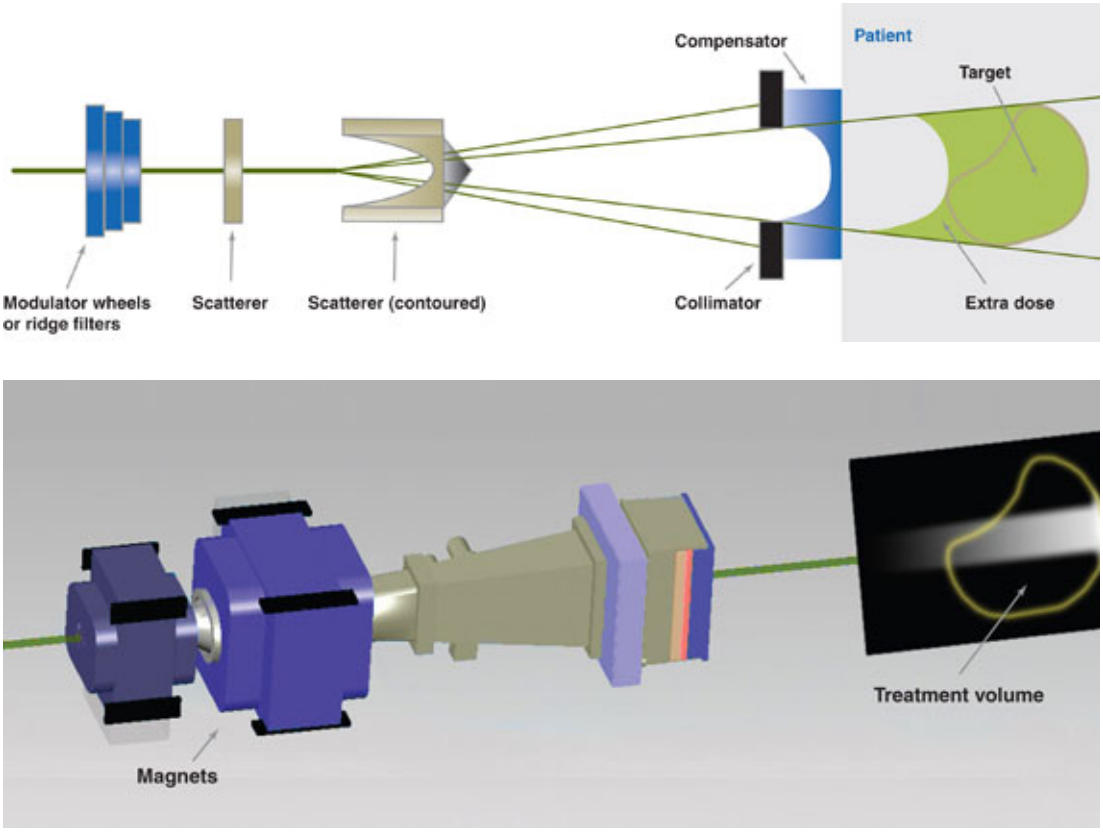

Figure 2.12. Schematic view of a passive scattering (top) and active scanning (bottom) beam delivery systems (source: [MARC2010]).

If the beam energy extraction is fixed, different kinds of range modulators can be used to produce a Spread Out Bragg Peak (SOBP) [GOTTSCHALK2004], or, if used in combination with scanning magnets, to select the desired range for every spot in the treatment field [PEDRONI1995]. Often, a combination of both passive and active elements are used like, for instance, the ripple filter described in [WEBER1999], used to broaden the Bragg peaks of monoenergetic light ion beams and compensate for its reduced straggling (section 2.1.2), allowing the construction of a SOBP with fewer energy spots.

Finally, the treatment field has to be adapted to match exactly the tumour position within the anatomy of the patient. Facilities equipped with a passive scattering system use large transversal fields and SOBPs, which are modelled with patient-specific collimators and range compensators. In contrast, facilities using energy selection and active scanning magnets use a "dose painting" strategy, where the beam is directed in turn to every voxel in the treatment plan, and stays on it the required time to deliver the desired dose. In order to monitor the dose delivered to the target (and thus adjust the time of the beam residence at each voxel), some dosimetry equipment (generally ionization chambers and position sensitive detectors) has to be part of the beam line. The calibration of such equipment (yielding the factors converting dose to water to machine monitor units, MU) is part of the regular QA process, and is explained in more detail in chapter 3.

Active scanning is considered the most modern approach, since it yields a more flexible patient treatment, with a more conformal dose distribution, eliminating the need for patient-specific hardware and facilitating adaptive planning strategies. Moreover, it spares the extra dose to the patient from neutrons and other secondaries produced in collisions of the beam with the passive elements in the beam line. However, it is sensitive to intrafractional motion, mainly caused by respiration. Mitigation strategies (such as gating, extended margins or target tracking) are required when treating moving targets with scanned beams [BERT2011]. In those cases, passively shaped treatment solutions might be easier to apply.

2.3.4. From dose prescription to treatment planning

A radiotherapy treatment planning is prescribed by a radiation oncologist. The physician delimitates the tumour volume and the organs at risk in high resolution CT images of the patient anatomy, with the aid of clinical examination and possibly other imaging techniques such as MRI (Magnetic Resonance Imaging) or PET (Position Emission Tomography). The clinical protocols in use at the centres determine the target dose in the tumour and the maximum allowed dose in the organs at risk (OAR).

Several concepts related to target delineation are used in daily practice, as well as in the literature [ICRU2007]. The Gross Tumour Volume (GTV) is the gross palpable, visible or clinically demonstrable location of the malignancy, including affected lymph nodes or other metastases. The Clinical Target Volume (CTV) is a volume containing the GTV and all the surrounding areas with a high probability of malignant cells, based on the judgment of the oncologist. The Internal Target Volume (ITV) is a volume which includes the CTV, with a margin for uncertainty coming from factors internal to the patient: physiologic movements and variations in tumour size, shape and position. Finally, the Planning Target Volume (PTV) surrounds the CTV with margins to compensate for both internal and external uncertainties, such as patient positioning and setup uncertainties. While the definition of the GTV, CTV and PTV are compulsory and part of the treatment prescription, the delineation of the ITV is considered optional.

After target delineation and dose prescription, a Treatment Planning System (TPS) is used to construct a treatment plan. Its aim is to achieve a homogeneous RBE-weighted dose within the target volume, while depositing the minimum possible dose at the surrounding tissues.

The TPS solves the problem of how to deliver the prescribed dose distribution with the available number of fields, typically defined the treatment planners. Higher dose conformity is usually possible by an increased number of fields, at the cost of a longer treatment time. The incident angle of each field is chosen to minimize dose to organs at risk. The TPS optimization is an iterative process, which consists in minimizing a cost function. The treatment fields can be optimized separately (the TPS attempts to deliver a homogeneous dose with each field, which is called *single field optimization*) or as a whole (the TPS attempts to find a homogeneous total dose distribution, allowing large inhomogeneities in the individual fields). The latter is called *intensity modulated* therapy or *multiple field optimization* [LOMAX2001, GEMMEL2008].

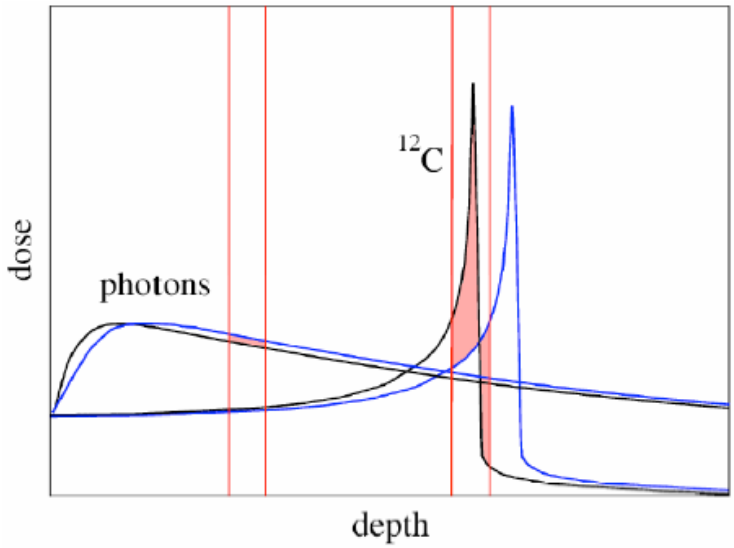

Figure 2.13. For photon treatment, range errors have a small impact in dose distribution. In contrast, for light ions, due to their sharp dose distribution, a similar error in range could result in much more severe dose mismatch (from [CHU2006]).

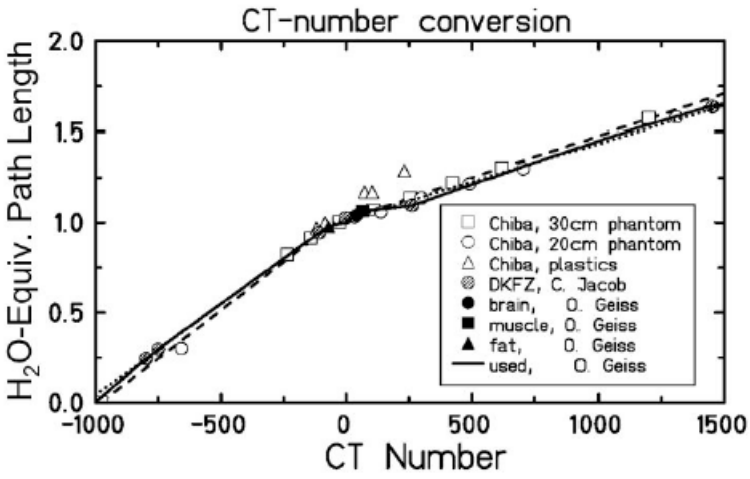

Figure 2.14. Conversion curve of CT numbers to water-equivalent path lengths (from [CHU2006]).

While more conformal dose distributions can be achieved with intensity modulation, single field optimized plans might be more robust and therefore preferable in some cases (a plan is considered *robust* when it does not produce large changes in the dose distribution when affected by small changes in patient geometry or particle range). As shown in Figure 2.13, the consequences of range errors are more dramatic in particle therapy than in traditional radiotherapy. To perform the optimization, the TPS needs to estimate the dose distribution originated by the beam inside the patient. This is achieved by constructing a *pencil beam* model of the beam in water and converting the patient anatomy information from the CT into a water equivalent system. CTs are 3D maps of the photon attenuation of tissues, expressed in HU (Hounsfield units). For a material with an attenuation coefficient μ, the corresponding HU value is given by

$$HU = \{[\mu - \mu(water)] / \mu(water)\} * 1000. \quad (2.10)$$

HU values range from -1000 (air) to a few thousands, with a value of 0 defined for distilled water. The calibration of HU to WEPL (water equivalent path length) has to be done specifically for every CT machine in use, and revised as part of the QA process. The resulting, experimentally determined HU-WEPL calibration is a vital part of every treatment planning system. Figure 2.14, from [CHU2006], shows an example of such a conversion curve. There is no simple function relating CT number and ion stopping power. In a first step the relationship can be approximated with two linear regimes of different slope [MINOHARA1993]. Methods to calibrate the ion range to Hounsfield units have been investigated at PSI [SCHNEIDER1996, SCHAFFNER1998] for protons, and at NIRS [MATSUFUJI1998, KANEMATSU2003] and at GSI [JÄKEL2001, RIETZEL2007] for carbon ions. These studies show that for soft tissues in typical patient treatments, uncertainties up to 1-2% in range can be expected.

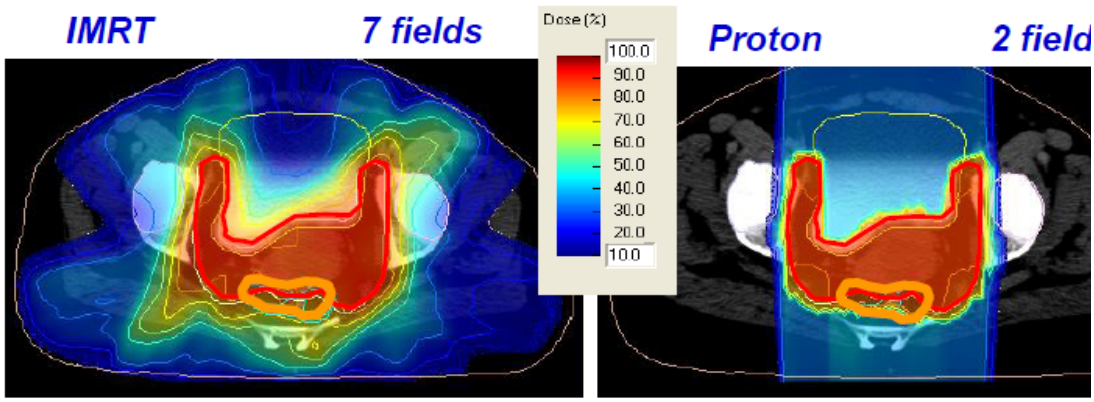

Figure 2.15. Comparison of a photon IMRT plan (left) with 7 fields, and a proton plan with 2 fields (right), for the same patient. It is evident that the proton plan achieves a much more conformal dose with fewer fields (from [GEORG2010]).

The comparison of treatment plans (such as the one shown in Figure 2.15) provide a clear picture of the benefit of charged particle radiotherapy over photon radiotherapy, even in its most advanced fashion like IMRT (Intensity Modulated Radiotherapy). The ballistics of charged hadron beams allows for improved tumour-conformal dose distribution and for substantially reduced integral dose to healthy tissue with fewer treatment fields than IMRT.

2.3.5. Machine and patient QA

Charged particle radiotherapy requires a high level of quality control over the entire process, from the initial planning to the final treatment delivery. Comprehensive quality assurance (QA) programs are deployed in every facility to ensure that no patient is treated inadequately.

Several QA protocols and sets of recommendations exist, usually adapting well-established procedures from conventional radiotherapy to the particularities of particle therapy. Compilations and recommendations reported in [ICRU2007] and [MAUGHAN2008] provide a good set of directives, at least for proton therapy. Each facility adopts the existing recommendations to their own QA strategy.

A considerable amount of time is devoted to quality assurance procedures, so a compromise has to be achieved between performing the necessary tests to ensure safe and accurate treatments, while minimizing the required time.

QA procedures exist for every single element of the treatment process, from the CT imaging to the dose delivery, including every piece of software and hardware of the machine. QA strategies involve a set of checks to be performed with a set recurrence (e.g., daily, weekly, monthly) or after a relevant change of the system.

QA can be subdivided in two types: machine QA and patient QA. Machine QA refers to all processes which are related to the maintenance and precision of the facility and includes, for example, measurement of ranges and beam lateral profiles, alignment of the treatment table, functioning of room safety systems, etc. On the other hand, patient QA refers to the set of specific processes relevant to the irradiation of a specific patient. It may include a technical review of the plan, Monte Carlo simulations, theoretical dose-to-water calculations, and the irradiation of a verification plan. Patient QA is generally more complex in scanned beam facilities [GILLIN2011]. At HIT and Marburg facilities, plan verification is performed using a water phantom and a matrix of ionization chambers based on the system described in [KARGER1999].

The work presented in this thesis is particularly relevant to all QA measurements involving dosimetry with ionization chambers. In particular, dose to MU calibration (section 3.4.1) and treatment plan verification (section 3.4.2) can directly benefit from the results shown here, as it will be addressed in the following chapters.

CHAPTER 3 Relevant aspects of dosimetry for Particle Therapy

3.1. Introduction

Dosimetry is the determination of absorbed dose in matter or tissue resulting from exposure to ioniziging to radiation. It can be performed under reference or non-reference conditions. Dosimetry under reference conditions refers to the determination of a dosimetric quantity (generally, the absorbed dose to water) following established protocols, in order to achieve cross-facility comparable results within a given precision. Dosimetry under non-reference conditions refers to a set of dosimetric processes which need to be undertaken when achieving reference conditions is either unfeasible or unfavourable. This includes dosimetry with tissue equivalent materials, as well as measurements for monitor calibration, commissioning and QA.

Dedicated international protocols exist for proton therapy dosimetry under reference conditions [ICRU1998, ICRU2007]. Heavier ions are covered by the International Atomic Energy Agency (IAEA) recommendations on dosimetry for external radiotherapy [IAEA2000]. All standards are based on absorbed dose to water, despite the fact that dose prescription for particle therapy is normally done in terms of photon iso-effective dose. Biological dosimetry in terms of cell survival has been proposed [GEMMEL2010], but this approach is only justified for radiobiology studies, or in the verification of new technologies, such as gating for moving targets. Extensive reviews have been published recently [KARGER2010, CUTTONE2011], comprising all details of dosimetry for particle beams. In this chapter, only the aspects relevant to the work presented in this Thesis are introduced.

3.2. Dosimetry equipment

3.2.1. Calorimeters

Absorbed dose to water can be measured directly from its definition (deposited energy per unit mass) by water calorimetry. Water calorimeters determine dose by measuring the temperature rise in a water tank induced by the energy deposited by a radiation field.

The standards for absorbed dose for photon beams are already based on calorimetry measurements in primary standards laboratories [IAEA2000]. Water calorimeters have been successfully used with proton and carbon ion beams ([BREDE2006] and others), but no primary standard has been developed yet for proton or carbon ion beams, although some laboratories are reported to be working on that topic (see [KARGER2010] for more details).

In any case, the scope of calorimetry is in principle restricted to standards laboratories, as its use requires a high effort and precision and a deep knowledge of the thermal properties of the device.

3.2.2. Ionization chambers

When ionizing radiation passes through a gas, interactions with the gas molecules produce ion pairs, typically charged molecules and free electrons. Ionization chambers use this principle to detect ionizing radiation. They are composed of a gas chamber and two electrodes producing an electric field inside it. The ion-electron pairs are attracted towards the conductors, and the collected electrons produce an electric signal which is related to the magnitude of the dose deposited within the chamber volume.

Depending on their shape, ionization chambers are divided into thimble and plane-parallel. Chambers of different sizes are available, depending on their purpose. Farmer-type chambers (thimble type, with a sensitive volume of the order of 0.5 cm^3) are used for reference dosimetry and monitor calibration (section 3.4.1), while the so-called pinpoint chambers (thimble, sensitive volume about 0.01 cm^3) are more suitable for high-gradient areas, commissioning, or plan verification measurements (section 3.4.2).

Plane-parallel chambers can also be used for reference dosimetry, but their main application is the registration of depth-dose distributions. Scanned and scattered beams require a different approach. For scattered beams, the chamber size is chosen small compared to the field size, in order to ensure lateral equilibrium of the secondary electrons [IAEA2000]. In contrast, for pencil beams in beam scanning facilities, bigger chambers are used, measuring the laterally integrated dose. Such chambers (called Bragg peak chambers) are often used in combination with the PTW PeakFinder™ system [PTW2008], which combines two Bragg peak chambers and an adjustable water column and allows automatic acquisition of a complete depth dose distribution by programming the registration steps along the field. Such system (see Figure 3.1) was used to measure all the depth dose distributions shown in this Thesis (chapters 4 and 5).

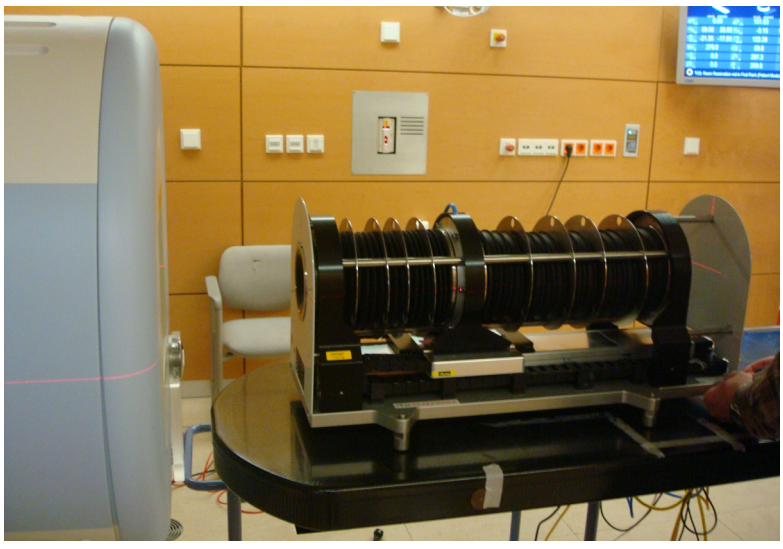

Figure 3.1. PeakFinder™ used for depth dose measurements positioned on the treatment table at HIT. The beam comes from the nozzle on the left side.

3.3. Dosimetry under reference conditions

In the absence of calorimetry-based standards for proton or light ion beams, the IAEA TRS-398 [IAEA2000] has published a standard based on ionization chambers.

The *beam quality index* (Q) of a radiation beam is a property of the beam which can be used to predict or estimate the effects of such radiation, or which can be used to differentiate between different beams of the same kind. [IAEA2000] defines a different quality index for each radiation type used in external beam radiotherapy; for protons and light ions, the selected property is the *residual range* (R_{res}), defined as

$$R_{res} = z - R_p, \tag{3.1}$$

where z is the depth of the measurement, and R_p is the *practical range* taken as R_{10}, the depth beyond the peak at which the dose falls off below 10% of the maximum dose (see Figure 3.2). This definition of R_p works for protons, but it might be problematic with heavier ions, in which the fragmentation tail (see section 2.1.5) can shift the 10% threshold away from the peak. The use of $R_p = R_{50}$ can then be a solution, as it has been proposed in [LUHR2011].

Plane-parallel or cylindrical ionization chambers are recommended for reference dosimetry of proton and light ion beams [IAEA2000]. Cylindrical chambers have a slightly lower uncertainty in their correction factors (as detailed later in Table 3.2); however, their use is recommended only at depths ≥ 0.5 g/cm^2 for protons, and ≥ 2 g/cm^2 for light ions. At lower depths, plane-parallel chambers are demanded.

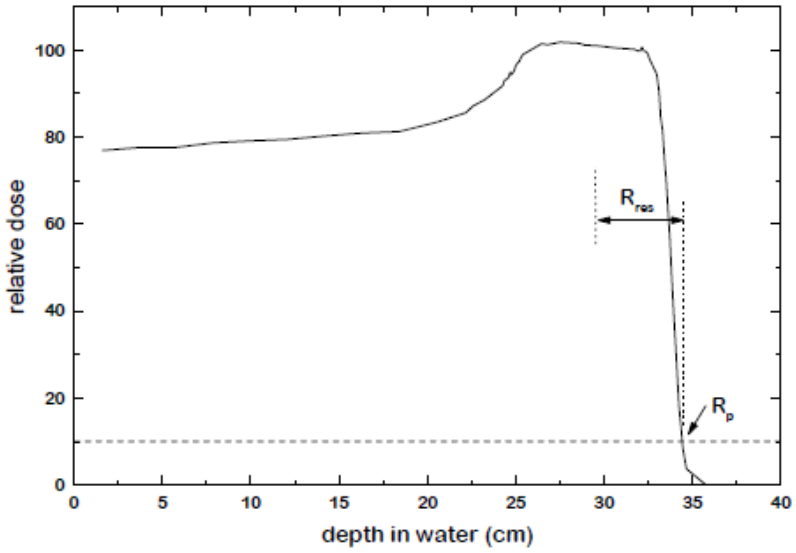

Figure 3.2. Definitions of practical range (R_p) and residual range (R_{res}). Figure adapted from [IAEA2000].

The protocol recommends the chambers to be positioned at the middle of the SOBP, with an exception for monoenergetic proton beams, where the positioning is at a depth of 3 g/cm^2, at the plateau area. Such recommendations are only suitable for passive-scattering systems

which construct the SOBPs with a modulating device (see section 2.3.2). For scanning-based facilities, where the SOBP is constructed by successive irradiation with monoenergetic beams of different energies, the calibration is done for monoenergetic beams and the chambers are placed at the plateau area, only at a few mm of depth [JÄKEL2004].

The absorbed dose to water for a beam with quality Q, expressed in Gray (1 Gy = 1 J/kg), is given by

$$D_{w,Q} = M_Q N_{D,w,Q_0} k_{Q,Q_0}, \tag{3.2}$$

where M_Q is the reading of the ionization chamber positioned at a reference point, N_{D,w,Q_0} is the chamber calibration factor at the reference quality Q_0, and k_{Q,Q_0} is the so-called *quality factor*, which accounts for the difference between the ^{60}Co gamma ray beam used for calibration at the standards laboratory, and the proton or light ion beam under study. It is determined specifically for every chamber.

The readout of M_Q is corrected by non-reference air density (effects of temperature, pressure, relative humidity), and also for recombination and polarization effects, as described in detail in [HARTMANN1999] and [IAEA2000]. The effective point of measurement is taken at the inner surface of the first chamber for plane-parallel chambers, and at a distance of 0.75 times the inner radius for cylindrical chambers [IAEA2000], as justified in [JÄKEL2000].

The quality factor k_{Q,Q_0} consists of three contributions,

$$k_{Q,Q_0} = \frac{(s_{w.air})_Q (W_{air})_Q p_Q}{(s_{w.air})_{Q_0} (W_{air})_{Q_0} p_{Q_0}}, \tag{3.3}$$

where $s_{w,air}$ is the water-to-air stopping power ratio, W_{air} is the energy to form an electron-ion pair in air, and p is a product of geometric, chamber-specific perturbation correction factors, for the respective beam qualities Q and Q_0.

The values of the quantities entering the k_{Q,Q_0} factor for the ^{60}Co reference beam (Q_0) are known with sufficient accuracy from the experience with conventional radiotherapy. On the contrary, the determination of these quantities for an arbitrary beam of quality Q in proton and light ion beams is subject to a higher uncertainty. In particular, for light ion beams, the fragmentation of the primary particles (discussed in section 2.1.5) makes the evaluation of the factors sensibly harder, since a rigorous calculation needs to average over the complete energy and particle spectrum of primaries and fragments. [IAEA2000] provides values of $s_{w,air}$ for protons and ion beams. For light ions, in absence of experimental data, the fix value of 1.13 (±2%) is adopted, neglecting any dependence with the residual range. For protons, the dependence of $s_{w,air}$ with R_{res} is given by

$$s_{w.air} = a + bR_{res} + \frac{c}{R_{res}}, \tag{3.4}$$

where the constants take the values a = 1.137, $b = -4.3 \cdot 10^{-5}$ and $c = 1.84 \cdot 10^{-3}$, with a combined uncertainty of 1% in $s_{w,air}$, and units of g/cm^2 for R_{res}. Improving the accuracy of the $s_{w,air}$ value for carbon ions is a main part of the research presented in this thesis, and it is covered in detail in Chapter 5.

A literature analysis performed in TRS-398 estimates W_{air} for protons and light ion beams, calculated as a weighted median from previous experimental values. In the case of protons, a value of W_{air}/e = 34.23 J/C is adopted, with an uncertainty of 0.4%. For light ions, the weighted median is calculated from a set of values for ion species from helium to argon, yielding W_{air}/e = 34.5 J/C, with a standard uncertainty of 1.5%. The data compilation shown in [KARGER1999] suggests no marked dependence of W_{air} with energy or particle type above 1 MeV/u, but the scarcity and dispersion of the data calls for a deeper investigation using calorimetry, which is out of the scope of this work.

The product of perturbation factors p_Q is taken to be unity for both protons and light ions, due to the lack of experimental data. p_Q is defined as $p_Q = p_{cav} p_{cel} p_{dis} p_{wall}$, where each element is described in Table 3.1. The uncertainty in the quality factor k_{Q,Q_0} is given by quadratic propagation of the individual uncertainties of its components, and shown in Table 3.2 below. It is worth remarking that plane-parallel chambers have a slightly higher uncertainty due to a higher error in the determination of wall effects for the ^{60}Co beam used for calibration. It can be seen from the data that the water-to-air stopping power ratio is the biggest source of error in k_{Q,Q_0}, both for protons and for light ion beams.

3.4. Dosimetry under non-reference conditions

In some occasions, dosimetric conditions in clinical practice differ significantly from the reference conditions, as the protocols are adapted to the specific situation of the facility, and to the clinical needs. In the following sections, the details of monitor calibration and patient plan verification as performed at the HIT facility are outlined. In fact, they rely on the use of ionization chambers, and therefore, they can benefit directly from the work presented in this Thesis.

3.4.1. Monitor calibration

The dose delivered to a patient in external beam radiotherapy has to be monitored, and transmission ionization chambers are usually used for this purpose. The beam monitor has to be calibrated, i.e., a correlation factor between the monitor units (MU) given by the beam monitor and the dose delivered to the patient needs to be established.

The procedures for monitor calibration differ significantly between facilities with passive beam delivery and those with active scanning, as displayed in Figure 3.3.

p_{cav}	Factor which corrects for effects related to the air cavity, predominantly the scattering of electrons in the inner side, making the electron fluence inside the cavity different from that in the medium in the absence of the cavity.
p_{cel}	Factor correcting for the influence of the central electrode of the chamber.
p_{dis}	Factor which applies to cylindrical ionization chambers when the reference point is taken at the central axis.
p_{wall}	Factor correcting for the non-medium equivalence of the cavity wall and any waterproof materials surrounding it.

Table 3.1. Definition of the perturbation factors in p_Q

Protons	**Cylindrical chambers**		**Plane-parallel chambers**	
Component	protons	^{60}Co + protons	protons	^{60}Co + protons
$s_{w,air}$	1.0	1.2	1.0	1.2
W_{air} / e	0.4	0.5	0.4	0.5
p_Q (combined)	0.8	1.1	0.7	1.7
Total uncertainty in k_{Q,Q_0}	-	1.7	-	2.1

Light ions	**Cylindrical chambers**		**Plane-parallel chambers**	
Component	light ions	^{60}Co + light ions	light ions	^{60}Co + light ions
$s_{w,air}$	2.0	2.1	2.0	2.1
W_{air} / e	1.5	1.5	1.5	1.5
p_Q (combined)	1.0	1.0	1.0	1.8
Total uncertainty in k_{Q,Q_0}	-	2.8	-	3.2

Table 3.2. Estimated relative uncertainties (in %) for the quality factors and corresponding components for proton and light ion beams, including the uncertainty in the quantities related to the reference radiation [IAEA2000].

.

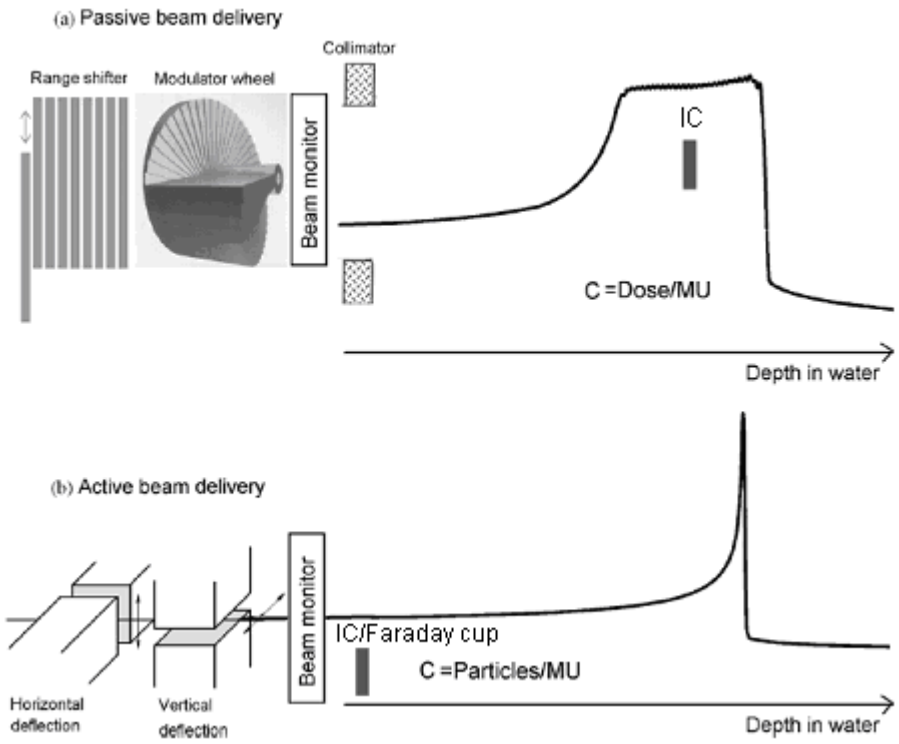

Figure 3.3. Differences in monitor calibration between different ion beam delivery systems. For passive delivery (a), the IC is placed at the centre of the SOBP, and the calibration is done in terms of dose/MU, whereas in active delivery (b), the reference dosimeter is placed at the entrance channel of a pristine Bragg peak and the monitor units are converted directly to the number of irradiated particles (adapted from [KARGER2010]).

In passively scattered systems, the MU calibration is done in terms of dose/MU. The dose is measured generally with an ionization chamber (IC) in a large and homogeneous field, and the IC is placed in the centre of the SOBP, as recommended for reference conditions. The calibration factor is obtained simply dividing the measured dose to the respective number of MUs counted by the upstream beam monitor, typically a large plane-parallel IC in the beam line. This method can applied in a straightforward way to protons, but for heavier ions, it is worth remarking that, due to the biological optimization in terms of RBE-weighted dose (cf. section 2.2), the SOBPs are in general not flat (see Figure 2.9), so care has to be taken when positioning the reference dosimeter in the field, as the irradiated dose will depend on the exact point of positioning.

The factor obtained at the reference position has to be corrected in order to derive the dose/MU factor at an arbitrary point of the treatment field, taking the patient-specific collimators and range compensators (cf. section 2.3.3) into account. Several models have been described for this purpose [KARGER2010], but nevertheless, it is common to calibrate each treatment field by measurements [TORIKOSHI2007, SAHOO2008].

For scanning facilities, the number of monitor units has to be controlled separately for each pencil beam of each available energy. Monitor unit calibration is even more important in scanning facilities, since the treatment planning systems specify the number of particles to be

delivered at every energy and scan point. The calibration coefficient has therefore the units of particles/MU, instead of dose/MU, and the dosimeter is placed at the entrance channel of the pristine peak, in absence of a physical SOBP. In practice, the number of particles can be determined directly (for example, by fluence measurements with a Faraday cup, as in [LIN2009] or [PEDRONI1995]) or indirectly, via dose measurements [JAKEL2004]. In the latter case the calibration factor is calculated as

$$C = \frac{N_{part}}{N_{MU}} = \frac{D_w(z)}{S(z)/\rho} \cdot \frac{\Delta x \Delta y}{N_{MU}}, \tag{3.5}$$

where N_{part} and N_{MU} are the particle number and the readout of the beam monitor per spot in calibration, $D_w(z)$ is the dose absorbed in water at a depth z along the beam direction, $S(z)/\rho$ is the mass stopping power of the primary particle at depth z, and Δx and Δy are the distances between different scan points in the X and Y directions. Alternatively, the calibration can be done over the complete radiation field, instead of on a spot by spot basis. The product $D_w(z) \cdot \Delta x \Delta y$ is then substituted by the integrated dose-area product at a depth z, $DAP(z)$, which can be easily measured with plane-parallel ionization chambers [GILLIN2010].

3.4.2. Plan verification

Plan verification is part of the patient-specific QA. It checks whether the delivered dose distribution complies with that calculated by the treatment planning system (TPS). To perform plan verification, the treatment field is irradiated in a phantom and detectors are placed in key positions in the field, in order to find possible relevant mismatches. Although several other systems have been proposed and are currently under investigation (e.g. tissue equivalent materials, 3D gels), plan verification is mainly done using ionization chambers in a water phantom [KARGER1999, LOMAX2004], due to their low LET dependence and to the possibility of electronic read-out of the measured dose.

For the verification measurement, the treatment plan is recalculated for the geometry of a water phantom using forward dose calculation tools included in the TPS.

For passive beam delivery techniques, the dose distribution in the treatment field is defined by a set of well-known, verified mechanical components (see section 2.3.2). Therefore, for a given setting of these devices, it may be sufficient to verify the dose at one single point within the treatment field.

For scanning systems, the dose distribution is constructed by adding up a number of independently delivered pencil beams of different energies at different scan positions. Consequently, the dose has to be verified for a representative set of positions. Single dose measurements with an ionization chamber would be very ineffective, as each individual measurement would require a complete application of the treatment field. The verification can only be done efficiently by simultaneous measurements.

An optimized dose verification system was developed for carbon-ion treatments with scanning beams at the GSI pilot project [KARGER1999]. It consists of 24 ionization chambers connected to a multi-channel electrometer and mounted in a block structure which

can be moved automatically via a computer-controlled system. The chambers are positioned in a compact assembly and do not shadow each other in beam's eye view. A similar approach is used at PSI [LOMAX2004], and a commercial implementation of the system (MP3-P Water Phantom, PTW Freiburg, Germany) is currently used in the Heidelberg and Marburg facilities (see Figure 3.4).

Since the main objective of plan verification is to spot possible errors in dose delivery, any difference between the planned dose distribution and the measured dose distribution has to be studied carefully, in order to rule out external sources of uncertainty which might lead to erroneous results. This includes minimizing uncertainties in the model used for dose calculation, and improving the stability and reproducibility the positioning system and readout electronics.

Additional uncertainties, however, may occur due to variations in the beam quality factor k_{Q,Q_0} with depth (see section 3.3) affecting the dose to water calibration of the ionization chambers, or due to interplays between adjacent chambers of the matrix. Such effects have been studied in detail in this work; the results are presented in Chapter 6.

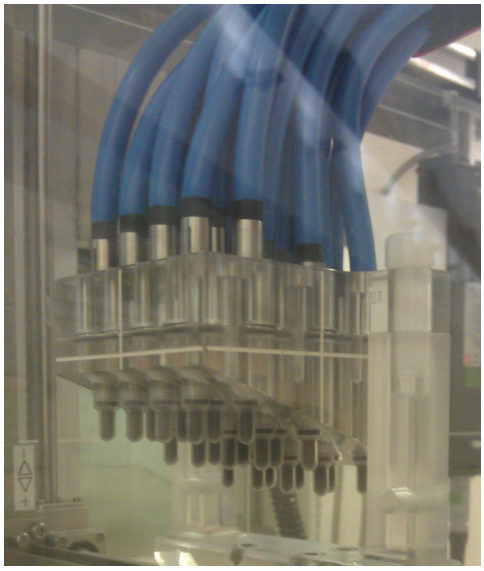

Figure 3.4. PTW Water Phantom (PTW Freiburg, Germany) used for plan verification and QA measurements of proton and light ion beams.

CHAPTER 4 Monte Carlo simulations and experimental validation

4.1 Introduction

Monte Carlo (MC) calculations are a standard tool in many areas of research, in particular in physics. The name Monte Carlo refers to any technique in which certain expressions or complex models are evaluated by taking successive random samples from a given distribution, and interpreting statistically the global results after several iterations. The technique dates back to the 1940s. It was developed in the framework of the Manhattan Project by Stan Ulam and John von Neumann [METROPOLIS1987], and its name is a reference to the famous casino in Monaco.

MC particle transport codes are used to simulate interactions and transport of particles in media. From the knowledge of the physics of the elementary collision processes, analog (or "event by event") MC simulations explicitly create, track and range out a number of primary particles, as well as the secondary particles which are additionally be created in the interactions. In some cases, the so-called "condensed histories" approach (as opposed to the "analog" approach) is used, where a number of small interactions are grouped together, and its effect is considered as a grouped single step. Multiple scattering of charged particles is a clear example of a process where the condensed history approach is widely used.

Apart from their wide application in basic research, they are also of increasing importance in applied fields such as medical physics. The main strength of MC simulations lies on its accuracy and the possibility to make calculations for arbitrary geometries where analytical calculations might be too complex or experimental measurements unfeasible. However, the goodness of the results of any MC simulation is, in general, as good as the physical models behind it, which are, in turn, as good as the experimental data by which they are supported. For this reason, an adequate configuration of the simulation program, if possible based on experimental measurements, is always needed.

For the work presented in this thesis, the MC code FLUKA [FASSO2005, BATTISTONI2007] was chosen, after the previous satisfactory performance demonstrated for proton and light ion therapy [SOMMERER2006, PARODI2007, PARODI2009]. Versions 2008.3d and 2011.2 were used during the research period, but all the results shown refer to the latest calculations with the last released FLUKA 2011.2 version.

4.2 The FLUKA code

FLUKA is a general purpose MC transport and interaction code originally created at CERN for high-energy physics. Since, 1991 it has been extended to cover a wider range of energies and related applications including radiation therapy. FLUKA is currently widely used for basic research, as well as in applied physics, including dosimetry, medical physics, radiation protection and space radiation. The code is written in Fortran, and it can simulate the interaction and propagation in matter of about 60 different particles, including photons,

electrons, neutrinos, muons, hadrons and all of the corresponding antiparticles The code can also transport polarized photons (e.g., synchrotron radiation) and optical photons.

Particle type	Transport limits (primary particles)	Transport limits (secondary particles)
Charged hadrons	10 keV – 10 PeV	1 keV – 10 PeV
Neutrons	thermal – 10 PeV	thermal – 10 PeV
Muons	10 keV – 1 PeV	1 keV – 1 PeV
Electrons	10 keV – 1 PeV	1 keV – 1 PeV
Photons	1 keV – 1 PeV	100 eV – 1 PeV
Heavy ions	< 10 PeV/n	< 10 PeV/n

Table 4.1. Transport limits for different particle types in FLUKA (source: FLUKA manual)

FLUKA implements the relevant physical models (described in section 2.1) as a set of separate packages. For particle therapy, the relevant models are summarized here. The electromagnetic physics is grouped into the EMF (ElectroMagnetic FLUKA) package. The continuous energy losses due to electromagnetic interactions are calculated using the complete Bethe-Bloch formula (equation (2.2)), taking into account the effective charge at low velocities and using Bragg's additivity rule for compounds (see section 2.1.1). The Barkas and Bloch corrections are part of the FLUKA code since the 2011 version. The nuclear stopping power is derived by means of a screened Coulomb potential and corrected for relativistic effects at high energies. The production of delta-rays (section 2.1.4) is described by a binary collision model, and controlled by a production threshold. Restricted stopping power is calculated by subtracting the calculated energy loss due to delta-ray production above the set threshold from the total stopping power. Molière theory is implemented to deal with multiple Coulomb scattering (section 2.1.3), and single scattering is also available, although its use is only recommended in certain cases (for example, near boundaries), due to its computational cost.

The implementation of nuclear interactions (section 2.1.5) is more complex. For nucleus-nucleus interactions of heavy ions with energies between 100 MeV/u and 5 GeV/u, the rQMD (relativistic Quantum Molecular Dynamics) [ANDERSEN2004] is used. For lower energies, a model based on the Boltzmann master equation (BME) [CERUTTI2006] was developed. .. For protons, hadron-nucleus interactions are described by the PEANUT model [FERRARI1998, BATTISTONI2006] which includes an intra-nuclear cascade stage followed by a pre-equilibrium stage, and then equilibrium particle emission. The latter stage (including evaporation, Fermi break-up, fission or γ-deexcitation) also applies to the treatment of excited pre-fragments resulting from the abovementioned nucleus-nucleus collisions. All these models have been recently benchmarked for therapeutic carbon ion beams in [BÖHLEN2010] and for therapeutic proton beams in [RINALDI2011].

4.3 Choice of physics settings for particle therapy simulations

Since FLUKA is a general purpose particle transport and interaction code, the physics settings have to be optimized in order to perform a time-efficient, yet accurate simulation for the desired application. The latest versions of the program include a default set of parameters for hadrontherapy simulations, activated with the card DEFAULTS with option HADROTHERAPY.

This set of defaults activates the maximum possible accuracy for the handling of particle scattering and ionization fluctuations (producing range straggling), sets a tabulation ratio of 1.03 for the logarithmic lookup tables of stopping power (maximum ratio between two consecutive energies of the tabulation), defines a maximum at 2% for the kinetic energy lost by a particle in a single step, and sets a default threshold for delta ray production of 100 keV, corresponding to a range of 0.14 mm in water [BERGER2005]. The transport threshold for charged hadrons is also set to 100 keV.

The default set HADROTHE was used in all our calculations. In addition to these defaults, a few other physics settings were tuned, following the same approach as in [PARODI2007]. The evaporation model was activated for accurate description of nuclear processes at its maximum accuracy (although it should not be relevant for our application with light targets), because of its minimal computational overhead. Fragments and nuclear recoils were also transported in detail, including energy loss, multiple scattering and nuclear interactions.

The δ-ray production threshold was adapted to meet the requirements of the specific simulations, since simulation time grows enormously with lower δ-ray thresholds, as the number of electrons to be transported increases dramatically, and electron transport is a very demanding task. For the validation described in the following section a threshold of 30 keV was selected (instead of the default value of 100 keV) in lieu of increased accuracy and for consistency with the accordingly lowered electron transport threshold down to 30 keV, as conservatively adopted in [PARODI2007, PARODI2009].

4.4 Experimental-based validation of FLUKA simulations

Once the physics settings are properly configured, two tasks remain in order to achieve a correct simulation of hadrontherapy applications. First, an accurate description of the beam delivery must be implemented into FLUKA. For a scanning system, the pencil beam model can be considered a reasonable approximation. The key parameters of this model are the beam size, given as full-width half maximum (FWHM) of a Gaussian distribution in the transversal plane, and the momentum spread, expressed as the FWHM of the particle momentum Gaussian distribution. In this work the beam sizes were taken from the beam libraries of HIT and Marburg Siemens Test Centre facilities (section 1.3). These values refer to the beam at the isocenter, but the parallel beam approximation is reasonable due to the large distance from the nozzle (~6m) of the scanning magnets. The momentum spread values were adjusted to best reproduce available experimental data, as suggested in [SOMMERER2006].

Second, the mean ionization potential of water I_w (see section 2.1.1) has to be adjusted. By default, FLUKA sets I_w=75 eV, but there is currently a lack of consensus about its exact value, and other values between 75 and 80 eV have been reported in the literature [ICRU1994, SIGMUND2009, BICHSEL2000]. We observed that a difference of 1 eV in the I-value yields a difference in range of about 0.15%-0.2%. Therefore, the simulated range in water of the particles was adjusted to experimental data, following the procedure proposed in [SOMMERER2006]. As justified in section 2.1.2, ranges are, everywhere in this chapter, taken at the 80% distal dose fall-off level.

The experimental particle ranges in water were obtained from depth dose distributions measured for monoenergetic beams at a number of representative energies, covering depths between 2 and 30 cm in water. The depth-dose distributions (DDDs) were measured with a PTW PeakFinder (section 3.2.2), placed at a distance of 5 cm from the beam nozzle. The curves for carbon ions were measured at the QA room of the HIT therapy centre (section 1.3.1), and the curves for protons were measured at the treatment room 1 of the Siemens Test Centre in Marburg (section 1.3.2). All curves, along with the FLUKA simulated depth dose distributions, are plotted in Figure 4.1.

The differences between the measured ranges and the ranges calculated with FLUKA can have two components. First, there can be a systematic offset, affecting equally the beams of all energies. This is most likely caused by uncertainties in the absolute calibration of the water column. If this is the case, a simple correction shift can be applied to match experimental data and simulation. On the contrary, if the difference between experimental and simulated ranges shows dependence with energy, the most likely cause is an over- or underestimation of the stopping power of water. This is the basis for the suggested experimental-based adjustment of the I_w value in the simulation. Figure 4.2 shows the observed range difference (experimental-simulated) for different values of $I_{w,}$ in the simulation for carbon ions (top) and protons (bottom).

As it can be derived from the plots, a value of I_w=78.0 eV minimizes the energy-dependent error for both protons and carbon ions. The constant offset (which can be attributed to an uncertainty in the determination of the reference position of the water column) is below 0.2 mm for all energies considered: the FLUKA simulation with I_w=78.0 eV reproduces the ranges of the therapeutic beams within 0.2 mm. This value is in good agreement with the latest value recommended by ICRU in its addenda to report 73 [SIGMUND2009].

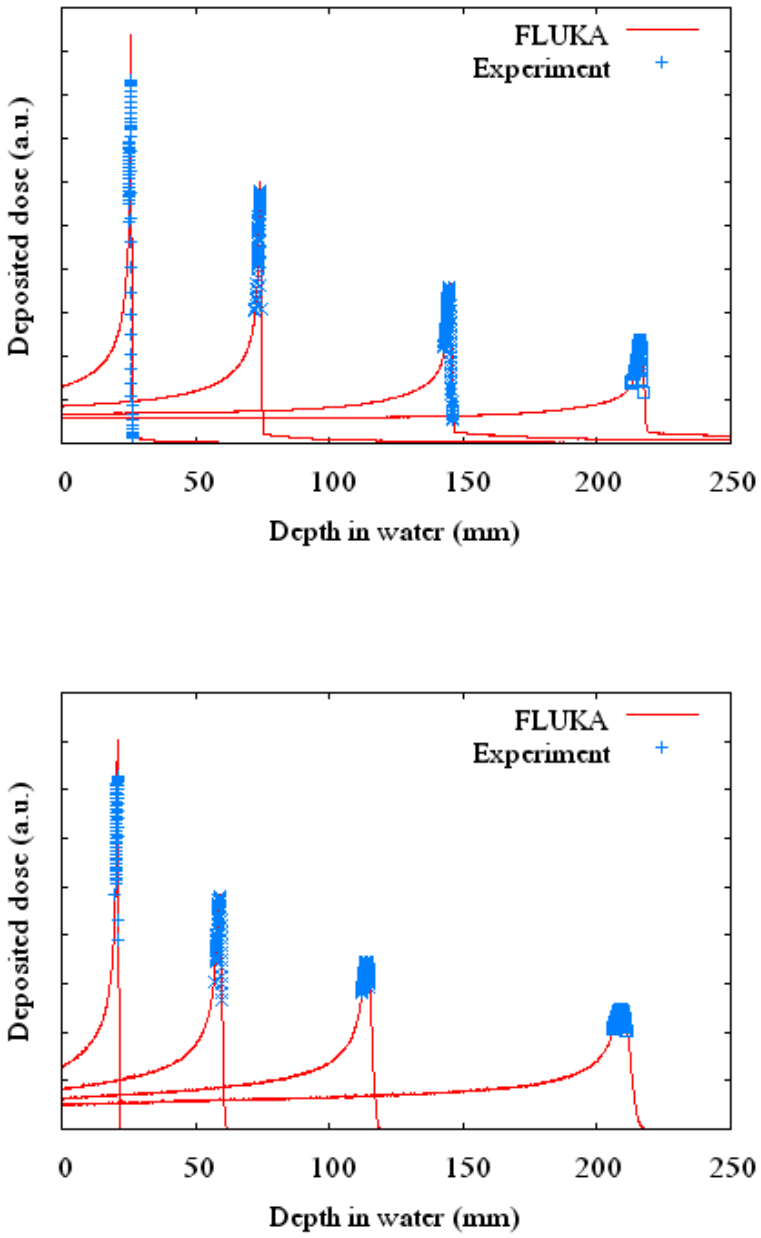

Figure 4.1. Simulated depth dose distributions and experimental data measured at HIT for carbon ions (top) and in STCM for protons (bottom).

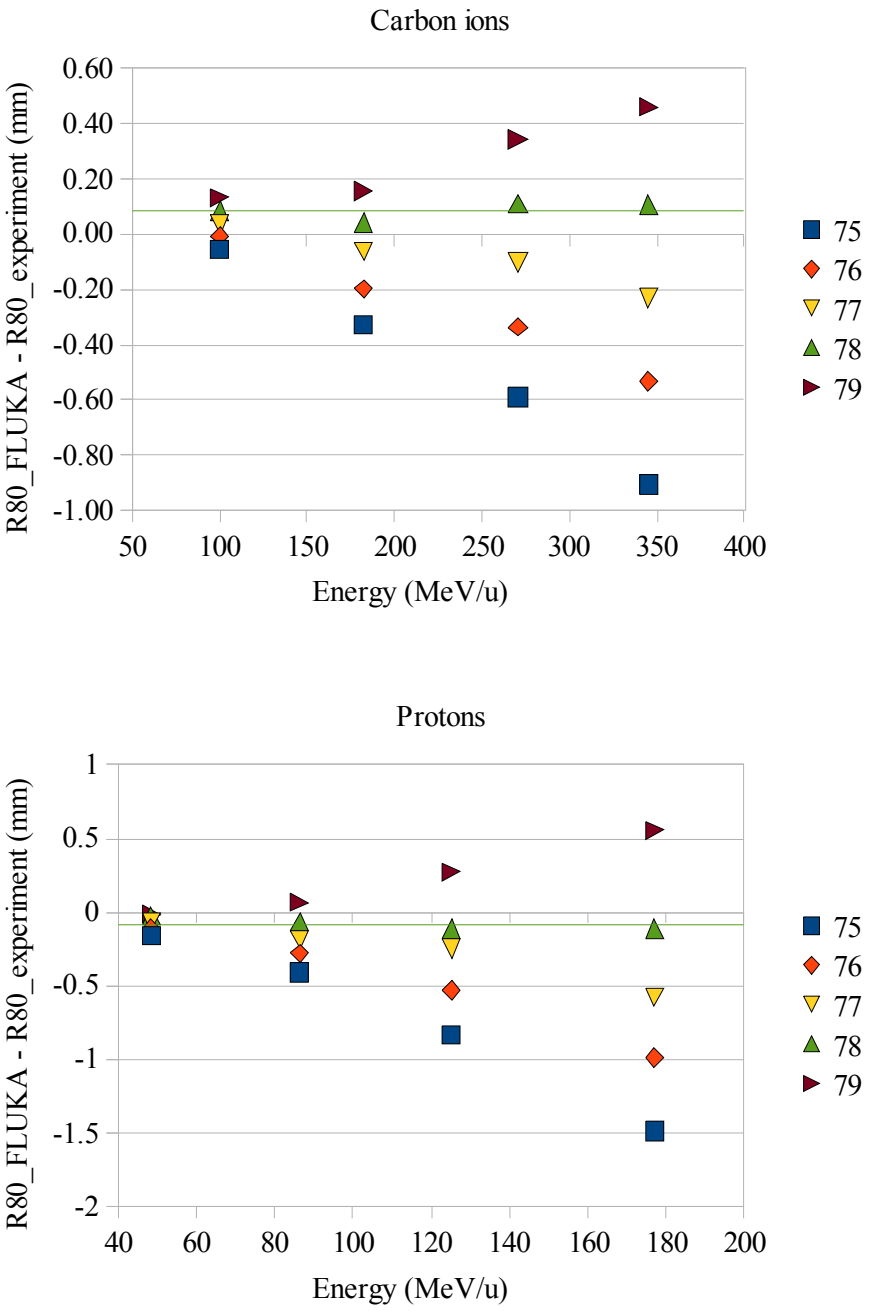

Figure 4.2. Difference in range (80% distal fall-off) between the simulated and measured curves, for different values of the mean ionization potential of water I_w in the simulation for carbon ions (top) and protons (bottom).

When working with particle ranges in water, it is important to keep in mind that the variation of water density with temperature can lead to errors. In particular, in Monte Carlo particle transport codes (and FLUKA is not an exception), water is usually defined with a density of 1 g/cm^3. However, for a normal room temperature of 22ºC, the value of water density is 0.9978 g/cm^3, and inside a patient body at 36.5 ºC, it goes down to 0.9935 g/cm^3 [HAYNES2010]. The variation of water density with temperature is usually not considered in Monte Carlo works, as it is typical to account for it, along with other possible unknown effects (for example, the presence of impurities in water), in the choice of the mean ionization potential. For the simulations presented in this work, both this experimental-based validation and the simulations presented in chapters 5 and 6, the value of ρ=0.998 g/cm^3 was used, valid for the interval 19º-23º C, the typical room temperatures in an air-conditioned facility. This is in line with the approach followed, for example, in [LECHNER2010], where a value of 0.997 g/cm^3 was used, corresponding to a measured room temperature of 24 ºC.

The methods and results presented in this section do not aim to achieve clinical accuracy for the FLUKA simulation system, as that would require a higher amount of data and a more detailed analysis. They were conceived as a test for the chosen physics settings, and a means to gain understanding of how FLUKA reproduces the irradiation with therapeutic proton or carbon ion beams. The presented choice of physics settings was a meaningful and experimental-driven choice, and this configuration was used in the investigations presented in chapters 5 and 6.

CHAPTER 5 Experimental and computational assessment of $s_{w,air}$ in ^{12}C ion beams

5.1. Introduction

Water-to-air stopping power ratio is the biggest source of uncertainty in the calculation of the quality factor for dosimetry of light ion beams with ionization chambers, as pointed out in section 3.3. The report TRS-398 [IAEA2000] defines it, for a generic ion beam, as

$$s_{w,air}(\vec{r}) = \frac{\sum_i \int_0^\infty \Phi_{E,i,water}(\vec{r}) \cdot (S_i(E)/\rho)_w \, dE}{\sum_i \int_0^\infty \Phi_{E,i,water}(\vec{r}) \cdot (S_i(E)/\rho)_{air} \, dE}, \tag{5.1}$$

where $\Phi_{E,i,water}$ is the point fluence in water, per energy E and particle species i, and S/ρ are the mass stopping powers in air (*air*) and water (*w*). Here $s_{w,air}$ is expressed as a point-like quantity to stress the fact that it is not, in principle, homogeneous throughout the irradiation field.

The aforementioned report recommends the value $s_{w,air} = 1.13$ for carbon ion beams, with a standard 1-sigma uncertainty of 2%. This value originates from an analysis from [HARTMANN1999], which justifies the choice "for practical reasons" on the basis of the experimental data available at that time (see Figure 5.1), under the assumption that the value of $s_{w,air}$ does not depend heavily on the particle type. The data shown in the figure is obtained by directly dividing the tabulated stopping powers for water and for dry air for primary ion beams of charge Z from 1 to 6, without taking into account the fluence spectra of the fragments.

The often quoted value of 2% for the overall standard uncertainty of $s_{w,air}$ was derived in [HARTMANN1999] from an analysis of the uncertainties derived from ignoring fragmentation of primary particles and neglecting range-dependence of the stopping powers. The results of that analysis are presented in Figure 5.2 and show deviations up to 4% in the peak area for monoenergetic Bragg peaks, but a variation in the order of 1% for extended SOBP dose deliveries similar to the ones used for therapy.

Several publications over the last years [GEITHNER2006, PAUL2007, HENKNER2009] have studied the value of $s_{w,air}$ for light ion beams. All these studies observe a variation of the stopping power ratio with penetration depth, namely, a raise of a few percent at the distal edge of the investigated pristine and spread-out Bragg peaks. This effect suggests that a finer parameterization of the stopping power ratio with range would be advisable, as recently proposed by [LUHR2011].

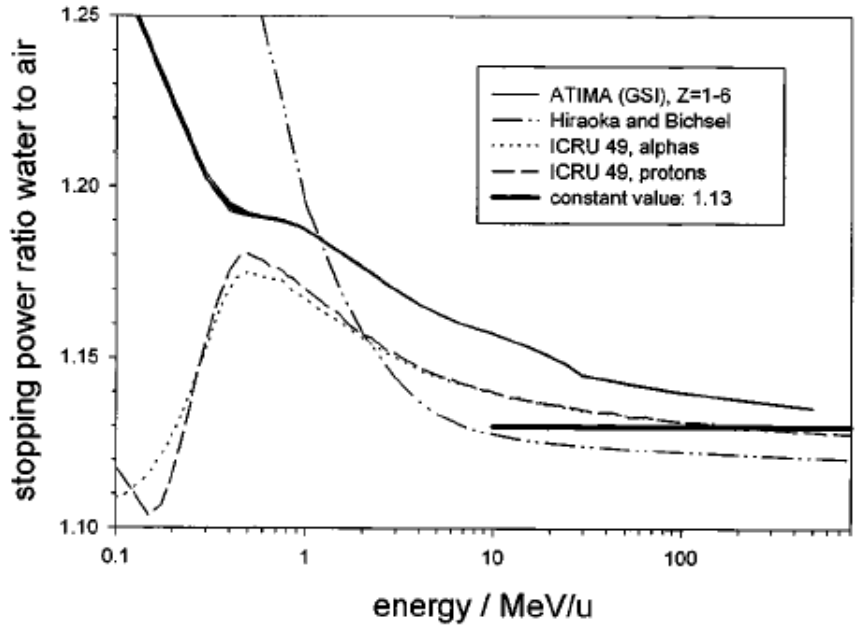

Figure 5.1. Direct ratio of water to air stopping powers for protons and other light ions according to different stopping power tables as of 1999 [SCHWAB1990, ICRU1994, HIRAOKA1995], motivating the current adoption of the constant value of 1.13 for carbon ion beams (Source: [HARTMANN1999]).

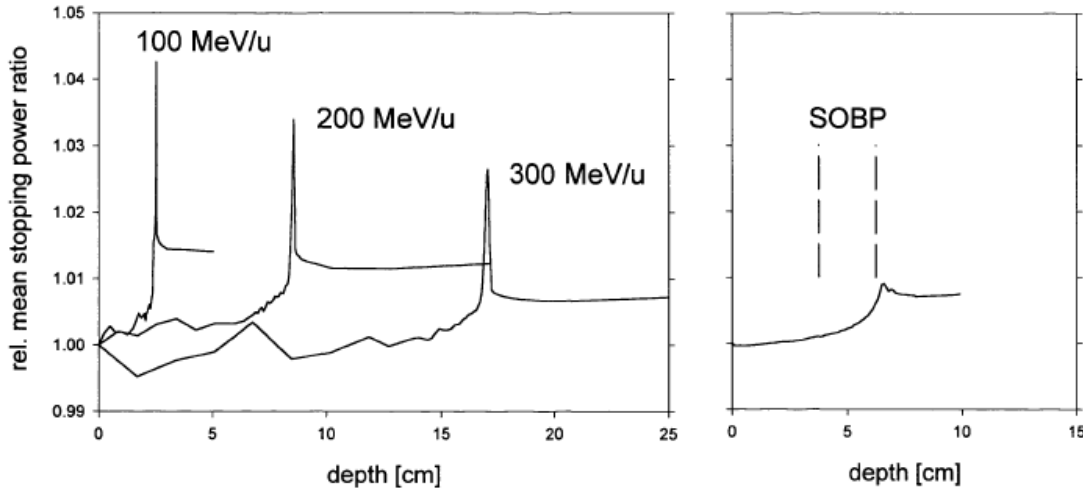

Figure 5.2. Mean water to air stopping power ratio of carbon ions as a function of penetration depth, normalized to unity at zero depth, for monoenergetic beams (left) and a SOBP centred at 5 cm (right, as marked by the dashed vertical lines), calculated with equation (5.1). (Source: [HARTMANN1999]).

However, these works also show a very strong dependence on the stopping power tables of the used Monte Carlo codes and analytical expressions. Therefore, they additionally account for the dependence on the stopping power tables by using the computational models with different pairs of I-values as input. As it can be clearly seen in Figure 5.3, the choice of mean ionization potentials for air and water has a very important effect in the value of $s_{w,air}$, with an apparent dependence on the ratio of I-values (I_{air}/I_w), as pointed out in [PAUL2007]. Additionally, the cited works calculate $s_{w,air}$ using equation (5.1) with unrestricted stopping powers, not performing explicit tracking of delta ray electrons. At the view of the results of [MEDIN1997] for proton beams, where discrepancies up to 0.6% in $s_{w,air}$ are reported as a result of including secondary electrons in the calculation, studying the effect of explicit delta ray transport is of relevance.

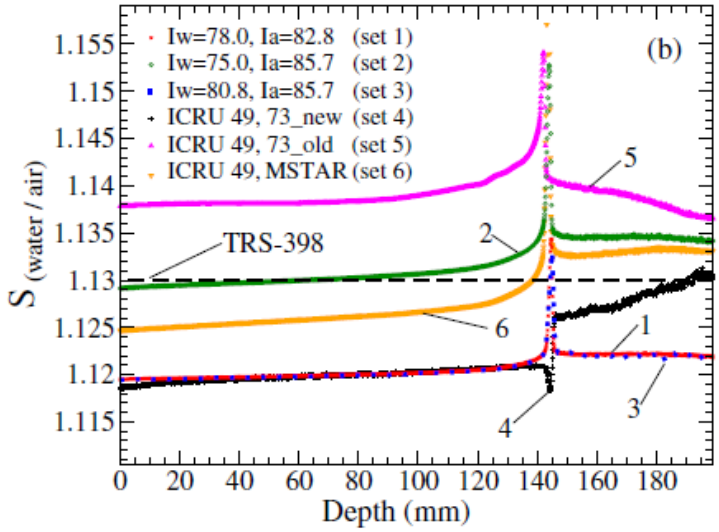

Set	I_w (eV)	I_{air} (eV)	I_{air}/I_w	Mode
1	78.0	82.8	1.06	SHIELD-HIT
2	75.0	85.7	1.14	SHIELD-HIT
3	80.8	85.7	1.06	SHIELD-HIT
4	78.0 (Z>2)	82.8 (Z>2)	1.06 (Z>2)	tabulated data
	75.0 (Z≤2)	85.7 (Z≤2)	1.14 (Z≤2)	
5	67.2 (Z>2)	82.8 (Z>2)	1.23 (Z>2)	tabulated data
	75.0 (Z≤2)	85.7 (Z≤2)	1.14 (Z≤2)	
6	75.0	85.7	1.14	tabulated data

Figure 5.3. Monte Carlo calculations performed with the SHIELD-HIT code [DEMENTYEV1999, GUDOWSKA2004] to determine the $s_{w,air}$ ratio for a carbon ion beam of 270 MeV/u initial energy when using different sets of I_w and I_{air} (adapted from [LUHR2011]). The I-value sets correspond to different published data. Discrimination with atomic number Z indicates that the available data tables have been calculated using different I-values for different particles.

The aim of the work presented in this chapter is to determine experimentally a coherent ratio of I-values (I_{air}/I_w), and then use the obtained ratio as an input to the Monte Carlo code FLUKA (cf. Chapter 4) to calculate $s_{w,air}$ in pristine peaks and SOBPs. Finally, the calculated $s_{w,air}$ values are fit to a single empirical expression, describing the variation of water-to-air stopping power ratio along the residual range of the treatment field.

5.2. Dependence of $s_{w,air}$ with the kinetic energy of the particles

Under certain conditions, the stopping power ratio, as defined in equation (5.1), can be approximated by the ratio of average stopping powers in water and in air of the primary particle.. In fact, if the treatment beam is studied at the entrance channel (immediately after it has exited the beam exit window and the beam monitoring system), the contribution to the stopping power ratio from secondary fragments can be neglected. Above approximately 1MeV/u, electromagnetic stopping powers are well described by the Bethe-Bloch formula (cf. section 2.1.1), which can be expressed in terms of the stopping number $L(\beta^2)$, multiplied by the atomic number to mass number ratio (Z/A) of the target, and a factor depending on the projectile velocity and physical constants. In the ratio of stopping powers, the factors which do not depend on the target material cancel out, yielding

$$s_{w,air} \cong \frac{\left(S_{^{12}C}(E)/\rho\right)_w}{\left(S_{^{12}C}(E)/\rho\right)_{air}} = \frac{(Z/A)_w L(\beta^2)_w}{(Z/A)_{air} L(\beta^2)_{air}}. \qquad (5.2)$$

Previously derived approximate expressions for the water-to-air stopping power ratio [PAUL2007, LUHR2011] leave out the correction terms when calculating the stopping number, using the simplified expression $L(\beta^2) = f(\beta^2) - \ln I$, where $f(\beta^2)$ is defined in expression (2.3). The effect of the correction terms for our beam energies is below 10^{-4} in the stopping number L, as discussed in section 2.1.1. This effect is equivalent to a difference of less than 0.005 eV in the I-values, which thus supports the usage of the simplified expression.

In the aforementioned previous works, the velocity of the projectile was calculated with the classical expression, $v^2=2E_0/m$, E_0 being the projectile kinetic energy, and m its mass. It is more precise to perform a fully relativistic treatment of the ions, using the expression

$$\beta^2 = 1 - [mc^2/(E_0 + mc^2)]^2. \qquad (5.3)$$

For a beam of 430 MeV/u, the difference between using the relativistic and the classical expression was of 0.0033 in $s_{w,air}$, which is equivalent to a difference of up to 2.5 eV in I_w, for a fixed value of I_{air}.

Combining equation (5.3) with equations (5.2) and (2.3) and adopting a value of 1.11195 for $(Z/A)_w/(Z/A)_{air}$ [ICRU1984] yields

$$s_{w,air} \cong \frac{\left(S_{^{12}C}(E)/\rho\right)_w}{\left(S_{^{12}C}(E)/\rho\right)_{air}} = 1.11195 \cdot \frac{\left[\ln\frac{2m_e c^2\beta^2}{1-\beta^2} - \beta^2\right] - \ln I_w}{\left[\ln\frac{2m_e c^2\beta^2}{1-\beta^2} - \beta^2\right] - \ln I_{air}}, \qquad (5.4)$$

which expresses the value of $s_{w,air}$ as a function of the velocity of the projectile and of the material I values, for a monoenergetic beam composed only of primary particles.

5.3. Experimental measurement of $s_{w,air}$

5.3.1. Principle

The *water equivalent thickness* of the air gap in the beam line (see Figure 5.1) can be measured as the shift which the gap causes in a depth dose distribution (DDD) in water. Using the notation of [ZHANG2010], it can be expressed as

$$z_w = z_{gap}\frac{\rho_{atm}}{\rho_w}\frac{\bar{s}_{air}}{\bar{s}_w}, \qquad (5.5)$$

Where z_{gap} denotes the size of the air gap, z_w the measured water equivalent thickness, and $\bar{s}$ represents the average mass stopping power (of water or air) between E and E-Δ, Δ being the energy lost at the air gap, which is in the order of 1-2 MeV/u. Therefore, the stopping power ratio between atmospheric air (denoted *atm*) and water (*w*) seen by a purely monoenergetic carbon ion beam of energy *E* without secondary fragments, denoted $s_{w,atm}(E)$, can be written as

$$s_{w,atm}(E) = \frac{\bar{s}_w}{\bar{s}_{atm}} = \rho_w^{-1}\left(z_w \Big/ z_{gap}\rho_{atm}\right)^{-1}. \qquad (5.6)$$

The proposed experiment measures the quotient $z_w/z_{gap}\rho_{atm}$ for a number of beam energies, studying the different water equivalent thicknesses of various air gaps. The necessary corrections to convert $s_{w,atm}$ to $s_{w,air}$ (this is, to correct for the effect of water moist in the atmosphere) are discussed later in this chapter.

5.3.2. Measurement of Bragg peak positions

The measurements were taken at QA room and treatment room H1 of the HIT facility (cf. section 1.3.1). Carbon ion beams of five different nominal energies were used: 100.07 MeV/u, 182.32 MeV/u, 270.55 MeV/u, 344.94 MeV/u, and 430.1 MeV/u, with beam sizes ranging between 12.9 mm and 9.8 mm (nominal FWHM at isocenter) and a nominal intensity of $5\cdot10^6$ particles/s.

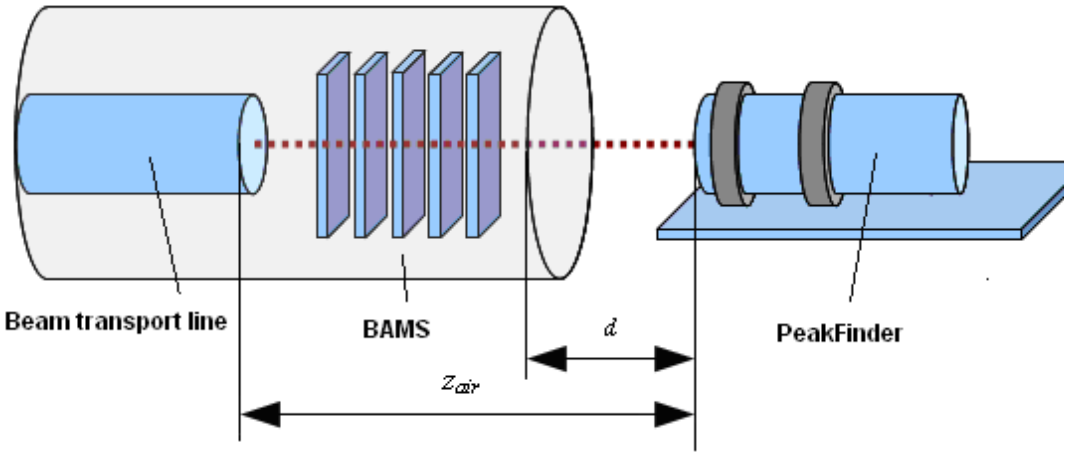

Figure 5.4: Scheme of the experimental setup.

The measurement scheme, depicted in Figure 5.4, is the same in both rooms. The beam exits the transport line and goes through the Beam Application and Monitoring System (BAMS), consisting of three ionization chambers and two multi-wire proportional chambers. The combined water equivalent thickness of exit window and BAMS is approximately 1.4 mm. Then, the beam traverses a distance *d* of air before hitting a PTW PeakFinder™ water column (Model T41030 Water Column, with servo control unit T41027 from PTW Freiburg; see Figure 3.1). It consists of two parallel-plate ionization chambers separated by a variable thickness of water. The first chamber is placed at the entrance (*reference chamber*), and the second (*field chamber*) moves along the device in the direction of the beam. The charge measured at the field chamber is scaled by the charge collected at the reference chamber, which makes measurements more robust against beam current fluctuations and allows them to be comparable for different beam intensities. The water column measures the DDD in water with a minimum step size of 0.01 mm. The device is filled with distilled water, which can be considered pure enough for our purpose. Only a small amount of an anticorrosive agent called Cillit [BWT2003] is added, but experimental measurements carried out at HIT estimate that it causes a raise of less than 0.05% in the absolute stopping power of water, which has a negligible effect in our experiment.

The PeakFinder™ was carefully positioned at a distance *d* from the beam nozzle (see Figure 5.1) either manually (QA room) or using the robotic treatment table (treatment room H1). The total size of the air gap z_{gap} is this distance *d*, plus the air gap between the exit of the vacuum window and the end of the BAMS, which amounts to 38.4 cm. This distance is considered to be filled with air, despite the presence of the BAMS, as the displaced volume of air is already accounted for in the water equivalent thickness of the BAMS. Each series of measurements contained distances varying from 5 to 150 cm.

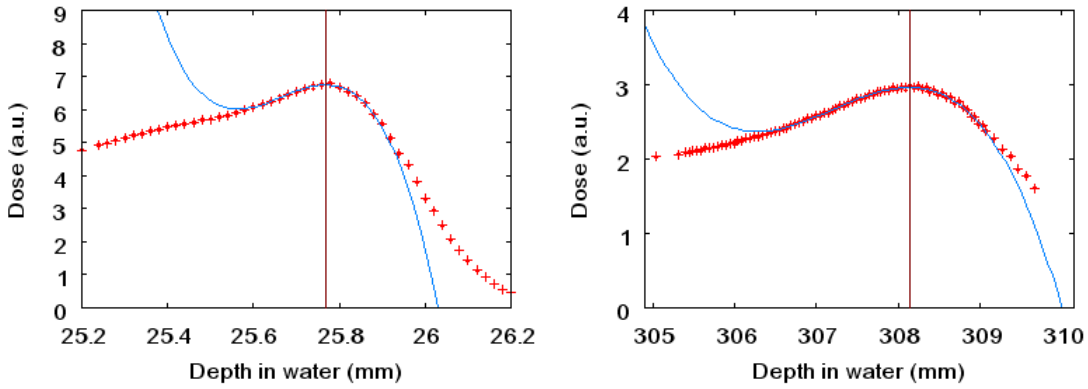

Figure 5.5: Determination of peak position by polynomial fit on E=100.07 MeV/u (left) and E=430.10 MeV/u. The peak of higher energy is broader due to straggling, as reflected by the different scale of the horizontal axis

Method	Range at 80%	Range at 90%	Peak position Gaussian fit	Peak position Polynomial fit
Standard deviation (µm)	2.3	1.7	1.3	1.2
Maximum difference (µm)	7.5	4.1	4.8	3.7

Table 5.1. Statistical variation in the reference point of a DDD (range or peak position) determined by different methods, for 10 consecutive measurements with a ^{12}C beam of 100.07 MeV/u in water.

In order to calculate the shift between depth dose distributions, a reference point in the DDD had to be established. Two choices arose here: choosing the range (as defined in section 2.1.2) as the reference, or choosing the position of the Bragg peak. In order to identify the best possible strategy, we analyzed the statistical variation in the reference point of the DDD, comparing range determination (at 80% and 90%), and peak determination methods (via fit to a Gaussian function of the upper 95% part, and fit to a polynomial function of the upper 90%). The results of this analysis, for a carbon beam of 100.07 MeV/u, are shown in Table 5.1.

At the view of the results, the reference of the DDD was set at the position of the Bragg peak, obtained by fitting its upper part (points above 90% of the maximum intensity) to a third grade polynomial (Figure 5.5), and determining its numerical maximum. This method is considered more robust, since, unlike the Gaussian function, it adapts to the asymmetric shape of the peak, allowing more points to be considered for the fit, and thus making it less sensitive to statistical fluctuations.

5.3.3. Alignment of the PeakFinder™

The water column was aligned vertically and horizontally with the laser markers indicating the isocenter (see Figure 5.6). While azimuthal angles are perfectly tolerable and do not affect the depth dose distribution (because the lateral dose is integrated at the Bragg peak chambers), a polar angle θ between the beam axis and the central axis of the water column would distort the range measurements, shortening the apparent range by a factor of $\cos(\theta)$.

The maximum polar angle allowed by the visual alignment procedure is determined as follows. The thickness of the reference lines on the water column and the laser markers is 1 mm. We estimate the accuracy of the visual positioning to be within 1mm, as the eye would certainly recognize a mispositioning when the laser marker does not touch the reference line. This uncertainty has to be considered four times, two for the horizontal markers and two for the vertical markers. By quadratic propagation of uncertainties, we can estimate that, if we consider the beam axis to be centred at one side of the water column, the projection of the axis will cross the opposite side of the water column at a point which is within 2 mm of its centre (standard uncertainty). Therefore, the standard uncertainty in the angle, provided that the distance between sides of the water column is of 700 mm, would be $\Delta\theta=\tan^{-1}(2/700)=0.16^{\circ}$. For a peak with a range of 30 cm (range of the peak with highest considered energy) a misalignment of $\Delta\theta=0.16^{\circ}$ would translate in an error of the peak position of ~ 1μm, one order of magnitude smaller than the minimum step size. Our measurements are therefore free from misalignment errors, even for the worse possible case.

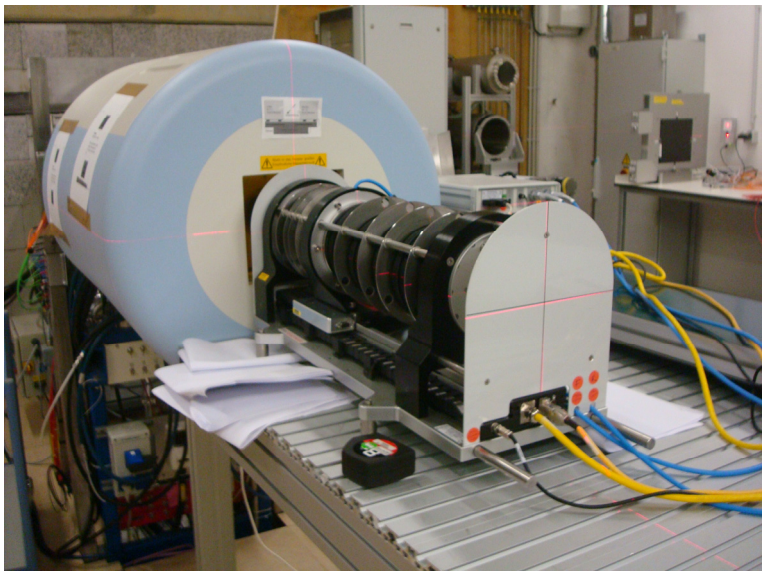

Figure 5.6. Water column positioned in front of the beam nozzle at the QA room of HIT. The red laser markers at the planes of the isocenter are aligned with the black marks on the surface of the water column.

Figure 5.7. Measurement of angle between the beam and the water column using a calibrated electronic level.

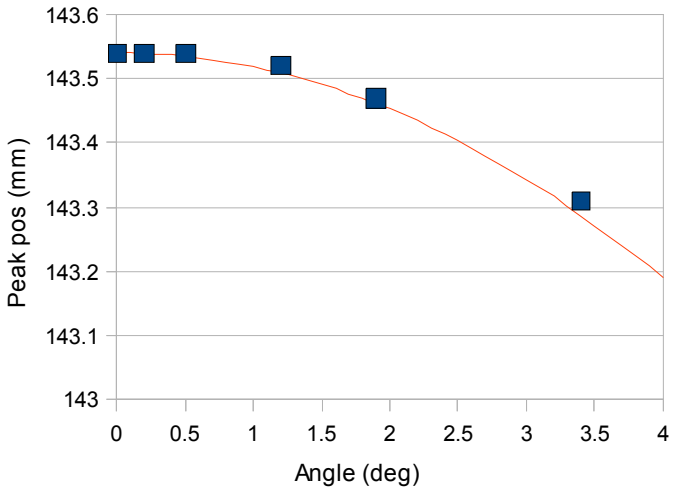

Figure 5.8. Range shortening of a 270 MeV/u carbon ion beam with a polar angle simulating a vertical misalignment of the water column. The solid line plots the range at 0º multiplied by cos(θ).

However, we carried out some additional measurements, positioning the water column forming different angles with the beam line in the vertical plane. These angles were measured using an electronic level, as shown in Figure 5.7. Its effect was studied using a monoenergetic carbon ion beam of medium range (270 MeV/u, with a range of about 14 cm). The results from such measurements are plotted in Figure 5.8: as expected, no shortening of the range is seen below a mispositioning angle of 0.5º, and the points decay with cos(θ).

5.3.4. Atmospheric conditions

During the experiments, the atmospheric conditions were carefully monitored. Temperature, air pressure and relative humidity were measured before and after every DDD acquisition, and its influence on water density, air density and moist content in air was taken into account in the analysis.

The dependence of water density with temperature was obtained from [HAYNES2010] The water column was placed in the experiment room several hours before the measurements, to ensure that the temperature of the water was the same as the measured room temperature. The density of atmospheric air was calculated by treating dry air and water vapour as ideal gases, yielding

$$\rho_{atm} = \rho_{vap} + \rho_{air} = \frac{p_{vap} M_w + p_{air} M_{air}}{RT}, \tag{5.7}$$

where p_{air} and p_{vap} are the partial pressures of dry air and water vapour, M_{air} and M_w the respective molar masses (in case of air, averaged assuming the composition of dry air reported by [WILLIAMS2010]), R the ideal gas constant and T the temperature. The p_{vap} was calculated from the measured relative humidity and the air saturation pressure, which was derived using the expression $p_{sat} = 2.504 \cdot 10^9 \cdot \exp(-5417/T)$, from [NASA2011].

$s_{w,air}$ is defined for dry air, so the content of water moist in the atmosphere was determined, and its effect subtracted from the observed air stopping power. Being $s_{w,atm}$ the observed stopping power ratio between water and atmospheric air, calculated with equation (5.6), and $f=\rho_{vap}/\rho_{atm}$ the mass fraction of water vapour in air, the stopping power ratio was calculated by

$$s_{w,air} = \frac{1-f}{(s_{w,atm})^{-1} - s_{vap,w} f}, \tag{5.8}$$

where $s_{vap,w}$ is the ratio of stopping powers between water vapour and liquid water for a carbon ion beam, which takes a value of 1.015 for all energies considered [SIGMUND2009].

5.3.5. Experimental values of $s_{w,air}$ derived from range shift measurements

The experimental procedure described in the previous sections was carried out repeated times, in order to acquire as much statistics as possible during the available beam time. In Figure 5.9, a compilation of all the data series taken is shown. Each series of {air gap, peak position} was fitted to a straight line, and from its slope and the atmospheric conditions, a value for $s_{w,air}$ was calculated.

The resulting values for the five different energies are plotted in Figure 5.10. Although a description of how $s_{w,air}$ varies with energy is preferable, the measured data can be summarized into a single value by calculating the weighted mean. The calculations in [LUHR2011] show that $s_{w,air}$ varies less than 0.3% in the plateau region (up to a residual range of 15 mm). The application of equation (5.4) yields, in fact, a maximum difference of 0.3% between the maximum and the minimum energies considered. Therefore, we can summarize the measured data in $s_{w,air} = 1.132 \pm 0.003$ (statistical) $\pm$ 0.003 (variation over the considered energy range), this value being valid for the plateau area. This value cannot be applied to the complete treatment field, as the variation of the stopping power ratio at the Bragg peak area is in the order of 2% for pristine peaks, and about 1% for SOBPs [HARTMANN1999, GEITHNER2006, LUHR2011].

5.3.6. Energy dependence of $s_{w,air}$

In order to consider the dependence of $s_{w,air}$ with the projectile energy, the data was fitted to equation (5.4), varying the I-values of water and air to reproduce the experimental data. For the fit we did not use the nominal energies, but we calculated the average energy of the ions inside the air gap. To do so, we deduced the energy which the ions lose in traversing the beam exit window and the BAMS, using the stopping power tables for water from [SIGMUND2009], to obtain the energy with which the particles hit the air gap *d* (see Figure 5.4). Then, assuming a constant stopping power of air along the gap, we calculated the average gap size for all the measurements with every beam energy, and subtracted the predicted energy loss after traversing half the average gap The resulting energies are detailed in Table 5.2.

Nominal energy (MeV/u)	Energy after BAMS (MeV/u)	Average gap size (WEPL in mm)	Average energy inside air gap (MeV/u)
100.07	96.9	0.56	96.3
182.32	180.3	0.52	179.9
270.55	268.9	0.74	268.5
344.94	343.5	0.73	343.2
430.10	428.8	0.73	428.5

Table 5.2. Comparison of nominal energies and estimated average energies inside the air gap. The values from the last column are used for the fit in Figure 5.10.

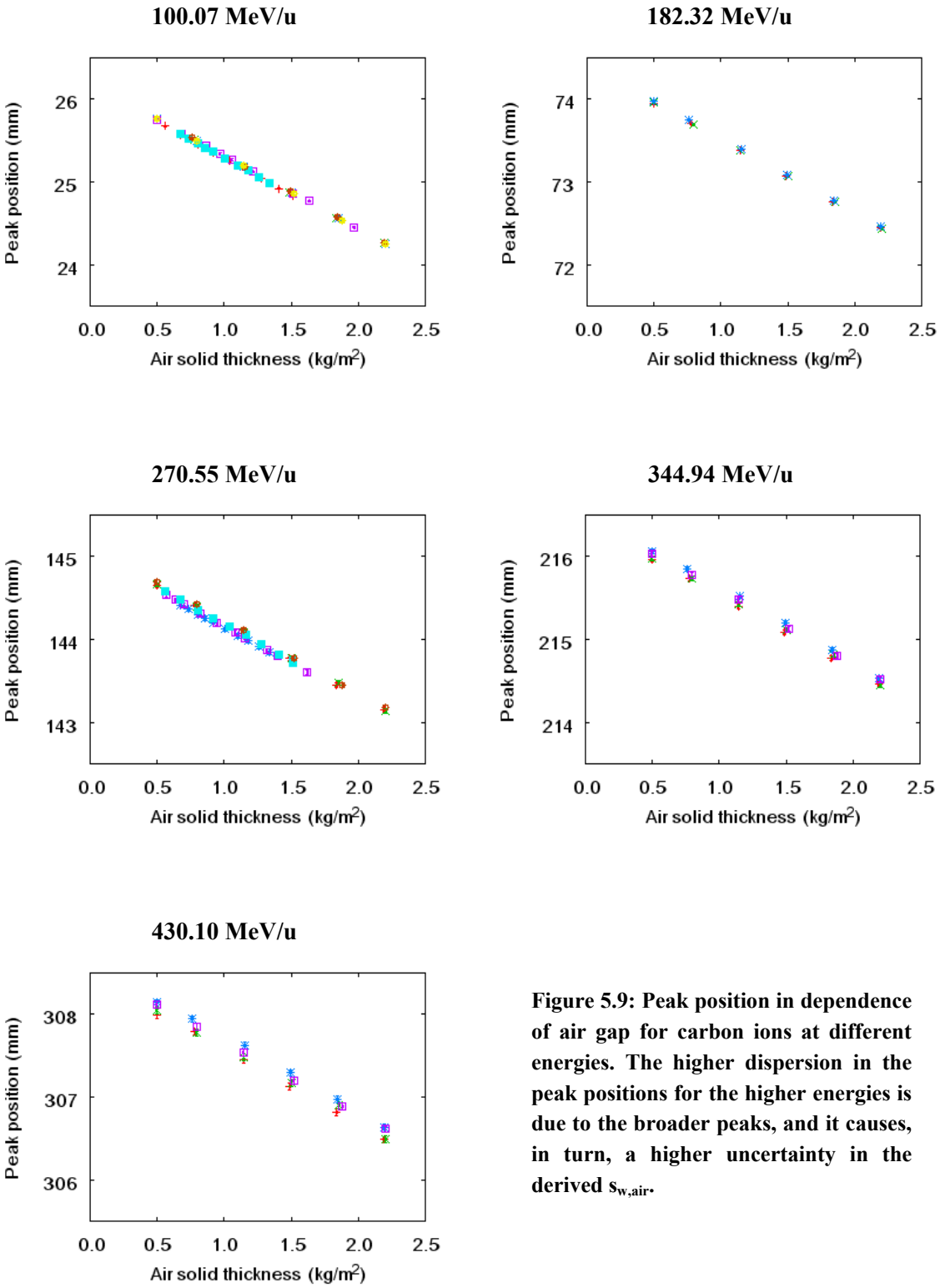

Figure 5.9: Peak position in dependence of air gap for carbon ions at different energies. The higher dispersion in the peak positions for the higher energies is due to the broader peaks, and it causes, in turn, a higher uncertainty in the derived $s_{w,air}$.

The free parameter used for fitting $s_{w,air}(E)$ was not I_a or I_w independently, but the ratio I_a/I_w. The actual value of I_w was found not relevant to the result of the fit. After obtaining similar

results with values between 65 and 90 eV, widely spanning all the previously cited values in the literature, the differences between them were one order of magnitude below the standard uncertainty of the resulting values (see Table 5.3). This is caused by the slow variation of the logarithm function, which causes equation (5.4) to depend primarily on the ratio I_a/I_w, rather than on their individual values.

The resulting fit can be seen in Figure 5.10 (solid blue line), compared to the experimental data and the average value. The dotted lines show the 95% confidence intervals for the fit and for the weighted mean, obtained by expanding the statistical component of the uncertainty by a coverage factor of 2.776, corresponding to the 95% level of the t-distribution for 4 degrees of freedom.

I_w (eV), fixed value	**I_a/I_w, obtained from the fit**
65	1.161 ± 0.024
78 (ICRU value)	**1.157 ± 0.023**
90	1.154 ± 0.023

Table 5.3. Sensitivity analysis for the result of the fit. Resulting (I_a/I_w) for different starting I_w values

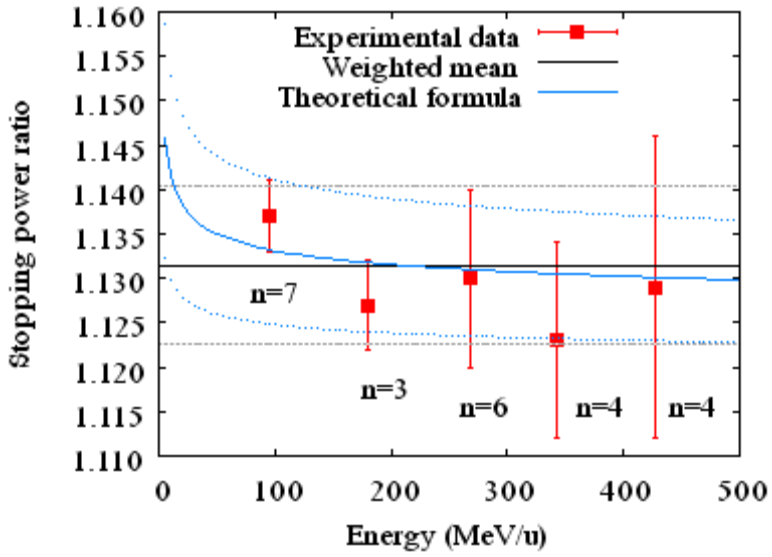

Figure 5.10: Water-to-air stopping power ratio vs. beam energy. The error bars of the experimental points show the combined standard uncertainties, and the label below them represents the number of repeated measurement series for each point. The weighted average is shown in black. The blue line shows the fit to expression (5.4) for I_{air}/I_w = 1.157. Dotted lines indicate the 95% confidence intervals for the fit and for the weighted mean.

5.3.7. Estimation of uncertainties

The experimental determination of stopping power ratio from the water equivalent thickness of air is affected by uncertainties at various levels. First, each pair of points {air gap, peak position} has an associated error. This error has an impact on the second level, the uncertainty on the determination of the slope of the fit to a straight line, which dominates the uncertainty in obtaining $s_{w,air}$ from expression (5.8). Finally, as the measurements were carried out repeated times, the dispersion of the data is considered by calculating the weighted average of the independent measurements and its associated uncertainty. The data analysis was performed in accordance with [BIPM2008].

5.3.7.1. Uncertainty in the solid thickness of air

The mass solid thickness of air is defined $t = \rho_{atm} z_{gap}$, the product of the geometrical extension of the air gap (in beam direction) by the density of air. Its error, Δt, originates from the limited precision in measuring the atmospheric conditions, as well as from the positioning uncertainty. It takes values of about $\Delta t = 3$ g/m^2, as shown with more detail in Table 5.4.

5.3.7.2. Uncertainty in the Bragg peak position

The systematic uncertainty of the position of the Bragg peaks, including the precision of the PeakFinder™ servo control and the uncertainty in finding the peak with the polynomial fit, is estimated via repeatability studies. For each energy, the water column was moved away and repositioned in the same place (simulating the movement between two points), and the peak of the resulting dose distributions was calculated. The process was repeated between three and six times (constrained by limited beam time), and the uncertainty in the peak determination u_{peak} was taken as the standard deviation of the sample. Apart from u_{peak}, the step size of the curve was taken into account. Although the minimum step size of the PeakFinder is 10µm [PTW2008], bigger steps had to be chosen, in order to speed up the data acquisition. The contribution from the stepping to the uncertainty, u_{step}, was estimated as half of the step size. Both contributions, as well as the combined uncertainties, are summarised in Table 5.5.

The combined standard uncertainties are indeed more accurate than the nominal precision of the water column, estimated by the vendor at 0.1 mm [PTW2008]. Since only the difference between peak positions is taken into account in this work, the uncertainty derived from the determination of the exact reference point of the water column was excluded from the analysis.

5.3.7.3. Uncertainty in the slope of the fit

The data series (see Figure 5.9) were fit to a straight line via a least squares fit. Since usual estimators for the uncertainty in a fit only take into account the uncertainties in the ordinate axis, a different approach based on bootstrapping, suggested in [BIPM2008A], was used to estimate the uncertainty in the slope m, in order to account for the uncertainties in both axes. For each series of points, several derivate series were artificially resampled, choosing each point randomly from a Gaussian probability distribution centred on the measured value and

Quantity, *symbol*	**Typical value**	**Typical uncertainty**	**Sources**
Temperature, T	22.5 ºC	0.13 ºC	Precision of equipment (0.1 ºC), possible variation during measurement
Air pressure, p	1000 mb	0.45 mb	Precision of equipment, (0.4 mb) possible variation during measurement
Relative humidity, Φ	25%	0.7 %	Precision of equipment, (0.5%), possible variation during measurement
Water saturation pressure, p_{sat}	27 mb	0.2 mb	From ΔT
Partial pressure of water moist, p_{vap}	8 mb	0.2 mb	From $\Delta\Phi$ and Δp_{sat}
Partial pressure of dry air, p_{air}	$p - p_w$	0.5 mb	From Δp and Δp_{vap}
Partial density of water moist, ρ_{vap}	$6 \cdot 10^{-3}$ kg/m^3	10^{-4} kg/m^3	From Δp_{vap} and ΔT
Partial density of dry air, ρ_{air}	1.16 kg/m^3	$7 \cdot 10^{-4}$ kg/m^3	From Δp_{air} and ΔT
Total density, ρ	1.16 kg/m^3	$7 \cdot 10^{-4}$ kg/m^3	From $\Delta\rho_{air}$ and $\Delta\rho_{vap}$
Mass fraction of water moist, *f*	**0.005**	**0.00015**	**From $\Delta\rho$ and $\Delta\rho_{vap}$**
Air gap distance, z	10-150 cm	0.2 cm	Precision of calibrated meter, margins in positioning device
Solid thickness, *t*	**0.1-2 kg/m^2**	**0.0025 kg/m^2**	**From $\Delta\rho$ and Δz**

Table 5.4. Typical values and uncertainties for the quantities used to calculate the solid thickness of air traversed by the beam, *t*, and the mass fraction of water moist, *f*.

Energy (MeV/u)	**Estimation of u_{peak}**		**Half step size u_{step} (µm)**	**Combined uncertainty u_C (µm)**
	Number of series	Standard deviation (µm)		
100.07	6	5.8	10	12
182.32	3	2.9	10	10
270.55	3	3.3	25	25
344.94	3	10.1	25	27
430.10	6	31.4	25	40

Table 5.5. Uncertainties in the peak position for different energies derived from repeatability studies, including mechanical uncertainty of the water column and error of the fit.

Quantity, *symbol*	**Typical value**	**Typical uncertainty**	**Effect on $s_{w,air}$**	**Sources**
Mass fraction of water moist, f	0.005	0.00015	~ 10^{-4}	See Table 5.4
Slope of the fit, m	0.89 mm/(kg/m^2)	0.010-0.040 mm/(kg/m^2)	0.01-0.05	Dispersion of points, propagation of Δz_p and Δt
Average temperature for all pairs $<T>$	22.5 ºC	0.3 ºC	Propagated through ρ_w	Variation during measurements
Density of water, ρ_w	**0.998 g/cm^3**	**7·10^{-5} g/cm^3**	**~ 10^{-5}**	**Propagation of $\Delta<T>$ through [HAYNES2010]**
Vapour to liquid water stopping power ratio, $s_{vap,w}$	1.015	0.002	~ 10^{-5}	Estimated from the tables in [SIGMUND2009]
Water to air stopping power ratio, $s_{w,air}$	**1.13**	**0.01-0.05**		**Propagated from equation (5.8) and data from this table**

Table 5.6. Uncertainty analysis for water-to-air stopping power ratio, calculated from equation (5.8).

with sigma equal to the standard uncertainty of the measured point. A least squares fit was performed on every resampled distribution, each of them yielding a different value for the slope. The standard deviation of this set of slopes was taken as the standard uncertainty of the slope.

5.3.7.4. Uncertainty in the final value of $s_{w,air}$

Following quadratic propagation of uncertainties from equation (5.8) via

$$u(s_{w,air}) = \sqrt{\left(\frac{\partial s_{w,air}}{\partial \rho_w} u(\rho_w)\right)^2 + \left(\frac{\partial s_{w,air}}{\partial f} u(f)\right)^2 + \left(\frac{\partial s_{w,air}}{\partial s_{vap,w}} u(s_{vap,w})\right)^2 + \left(\frac{\partial s_{w,air}}{\partial m} u(m)\right)^2}, \qquad (5.9)$$

we can conclude that the uncertainty in the slope dominates clearly the uncertainty in the stopping power ratio, with the quadratic term $(\partial_m s_{w,air}\ \Delta m)^2$ being various orders of magnitude larger than any other term, as shown in Table 5.6.Since the final values of $s_{w,air}$ were calculated as the weighed mean of repeated measurements, their standard uncertainty was calculated as the standard deviation of the weighed mean. Let $\overline{s_{w,air}}$ be the weighted mean calculated from *n* data sets, and $u_i(s_{w,air})$ the standard uncertainty of the i-th value, the uncertainty of the mean is obtained [GRAYBILL1959] as

$$u(\overline{s_{w,air}}) = \frac{1}{\sqrt{\sum_{i=1}^{n} u_i(s_{w,air})^2}}. \qquad (5.10)$$

5.3.7.5. Uncertainty in the fit parameter I_a/I_w

The data was fitted using the tool *gnuplot* (*http://www.gnuplot.info*). Since equation (5.4) is not linear, the asymptotic standard errors given by the program for the parameter of the fit might not represent correctly its standard uncertainty. The bootstrapping approach explained in section 5.3.7.3 was used to calculate the uncertainty of the obtained parameter (I_a/I_w). Several data tables (N=25000, a value above which no statistical fluctuations were observed) were constructed by sampling from the measured values and uncertainties of $s_{w,air}$, and for each of them, the data was fit to equation (5.4). The standard uncertainty for (I_a/I_w), shown in Table 5.3, is then taken as the standard deviation of the set of obtained parameters from the fits.

5.3.8. Discussion of the experimental results

Water-to-air stopping power ratio was measured for monoenergetic carbon ion beams of five different energies, by determining the water equivalent thicknesses of air gaps of different sizes. The data from the five different beam energies was combined in an average value of $s_{w,air}$ = 1.132 ± 0.003 (statistical) ± 0.003 (variation over energy range), valid for monoenergetic carbon ion beams at the plateau area of the depth dose distribution. A theoretical expression describing the variation of the stopping power ratio with kinetic energy, sw,air(E), was derived from the Bethe-Bloch formula and fit to the measured data, yielding a coherent pair of I_w and I_{air} values with I_{air}/I_w=1.157±0.023.

The presented data is perfectly consistent with the previously published data [IAEA2000, GEITHNER2006, PAUL2007, HENKNER2009]. The fact that the stopping power ratio depends primarily on the ratio of mean ionization potentials, I_w/I_{air}, allows us to calculate $s_{w,air}(E)$ using expression (5.4) without depending on a specific I-value. The current value of the uncertainty in I_w/I_{air}, around 2%, arises from a combination of factors (as described in section 5.3.7) but has mainly a statistical origin. More series of measurements would, of course, reduce the statistical uncertainty. In particular, it would be interesting to continue with measurements at low beam energies, since the peaks are sharper and the uncertainty in the peak position is lower.

Although interesting, measurements in the low-energy area, where the raise in $s_{w,air}$ is more pronounced, cannot be carried out with the current setup. The presence of a reference chamber in the PeakFinder™ limits its usability to beams with a range of at least 1.5 cm in water. The use of another instrument, like, a robotic system to hold ionization chambers, such as the one described in [KARGER1999], could solve this problem. However, it would not be easy to achieve the μm precision required for such measurements, and without automation in the acquisition of the depth dose distributions, the amount of beam time required would, in practice, make it unfeasible.

Care needs to be taken when interpreting the fit to equation (5.4). Even if it extends to low energies and describes the expected rise in the stopping power ratio with decreasing energy, the assumptions used in its derivation might lead to increased uncertainties if used outside the *clean area*, i.e., the portion of the range where the beam is composed mainly of the primary particles, with low energy straggling and fragmentation. For a complete study of the variation of $s_{w,air}$ with penetration depth, including the effect of fragmentation, a full Monte Carlo study is required. Such study is carried out in the following sections.

The described experimental procedure can be used with slight modifications with other ion species such as protons, alpha particles and oxygen ions.

5.4. Monte Carlo calculation with FLUKA

5.4.1. Introduction

In the literature, water-to-air stopping power ratios have been calculated using different implementations of the Spencer-Attix cavity theory (see [PODGORSAK2005] for a detailed description). For ions heavier than helium, all studies considered [GEITHNER2006, PAUL2007, HENKNER2009], carried out with the MC code SHIELD-HIT, used unrestricted stopping powers, not performing explicit tracking of delta ray electrons. While the earlier work from Geithner *et al.* calculated explicitly the contribution from track-ends to $s_{w,air}$, its results, showing a very low impact from track-end particles, caused subsequent works to neglect this contribution (all these SHIELD HIT calculations used 25 keV as a transport cut-off for all the tracked charged hadrons). For protons, the work presented in [MEDIN1997], performed with MC code PETRA, did include explicit tracking of delta ray electrons and energy deposition by track-ends. Regarding the transport thresholds (cf. section 2.1.4), the commonly used value of 10 keV in electron and photon dosimetry [PODGORSAK2005] was used in [MEDIN1997] for secondary electrons, whereas 1 MeV

was chosen as transport cut-off for protons. The SHIELD-HIT calculations used 25 keV as a transport cut-off for all charged hadrons.

On the basis of these works, we decided to use explicit delta ray tracking, with a delta ray production threshold of 30 keV. The value is chosen as a compromise between accuracy and speed of the simulation, being slightly higher than the value of 10 keV used in [MEDIN1997] [MEDIN1997] but lower than the 100 keV default typically suggested for hadrontherapy applications. This threshold was already used for the dose calculations presented in chapter 4. For consistency, the transport cut-off for electrons particles was also set to 30 keV. Due to the low impact for ion track ends predicted in [GEITHNER2006], they were not included in the analysis.

The calculation here presented was carried out in two steps. In a first step, the stopping power tables were generated, taking into account the experimental-based determination of $I_{air}/I_w=1.157\pm0.023$. The dependence on I_w/I_{air} was implemented by using a fixed value for I_w (as determined in chapter 4) and attributing all the variation to I_{air}. Four tables were generated, for water with $I_w=78$ eV and for air with $I_{air}=90.2$, 88.4 and 92.0 eV (corresponding to I_{air}/I_w ratios of 1.157, 1.134 and 1.180 respectively, spanning the complete range under consideration of uncertainty).

In a second step, the irradiation into a water phantom of pristine peaks, SOBPs and treatment plans was simulated. The resulting fluences in water for each irradiation field were scored independently into four scoring 3D meshes, each of them using a different stopping power table to multiply by the fluence events, in order to construct, for every voxel, the numerator and the denominator of equation (5.1). The data was then combined offline into three $s_{w,air}(\vec{r})$, one for each I_{air}/I_w value, expressing the calculated stopping power ratio throughout the field, for every irradiated plan.

The two steps are addressed in detail in the following subsections.

5.4.2. Restricted stopping power tables for air and water

Restricted stopping power tables (in water and in three versions of air with different I values) were calculated for all stable and metastable isotopes for elements lighter than oxygen. In order to avoid unpredictable behaviour of the code upon production of a strange isotope, tables for extremely uncommon and unstable isotopes lighter than ^{16}O were also created. The stopping power tables in water are displayed in Figure 5.11.

The tables were extracted from the standard FLUKA output (OUT file), using the DELTARAY card with WHAT(1)=0.0003 (δ ray threshold at 30 keV) and option PRINT activated. If the card HI-PROPE is present, the tables in the output file under the heading HEAVYION show the restricted and unrestricted stopping power tables for the selected ion. Data for hadronic particles lighter than alpha particles is shown in separate headings, regardless of the content of the HI-PROPE card.

Restricted stopping powers of electrons are, however, not shown in the output file, so a tweak was used to extract the tables calculated by the FLUKA internal physics models. A

script was written to shoot successive electron beams of different energies into a target of 10^{-4} g/cm^2 of air or water, and extract the energy deposited in the target, using a USRBIN scorer with region binning. The target thickness was chosen small so that that the energy loss was low compared with the energy steps. Random fluctuations were not activated (via IONFLUCT card), in order to extract the nominal energy loss from electromagnetic interactions. The energies were chosen in logarithmic steps from 30 keV up to 10 MeV, widely spanning all possible energies of the secondary electrons. The script implementing this method was tested with a ^{12}C beam, and its results compared to the stopping power tables displayed in the output file. The results of the comparison are shown in Figure 5.12, with almost a perfect match between both tables.

The obtained table was also compared to the nominal stopping power for electrons from ESTAR database [BERGER2005] (Figure 5.13), with a reasonable result: the curves follow the same trend, with the restricted stopping power being consistently lower than the unrestricted one.

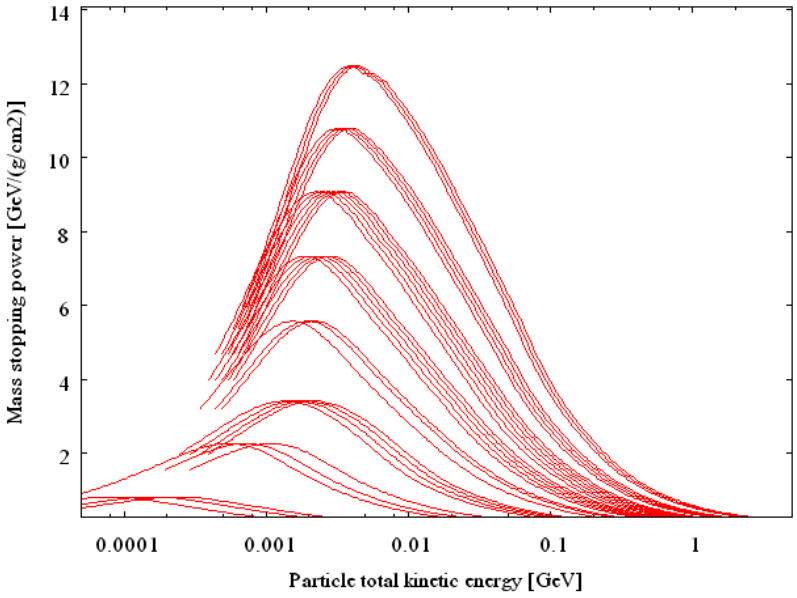

Figure 5.11. Restricted stopping power tables in water for several isotopes from p to ^{16}O, as calculated with FLUKA. The δ-ray production threshold was set at 30 keV.

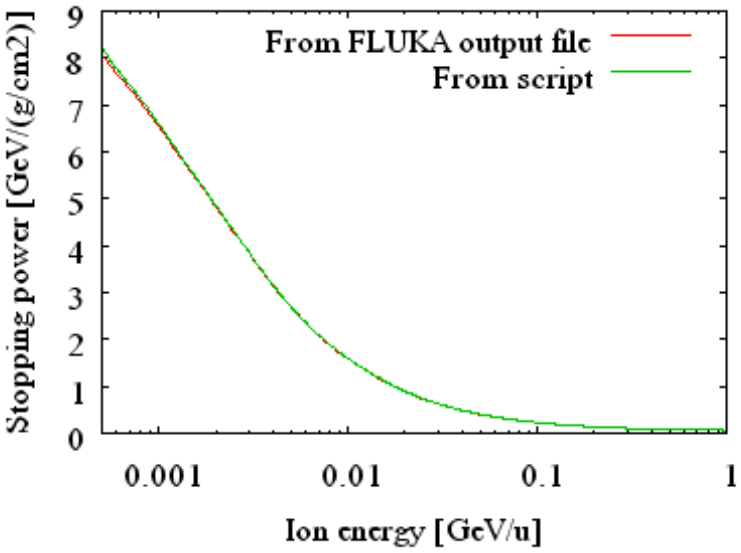

Figure 5.12. Restricted (δ threshold=30 keV) stopping power of ^{12}C in water, as calculated with the script, compared to the table shown in the FLUKA output file.

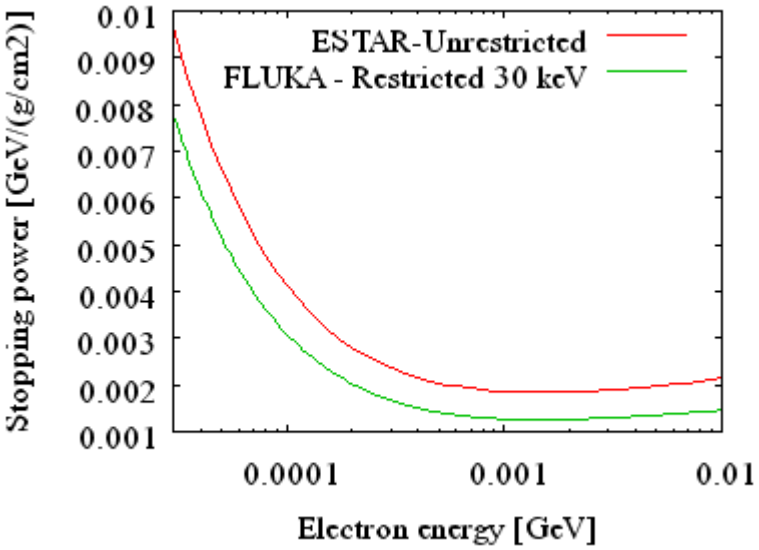

Figure 5.13. Restricted stopping power of electrons in water calculated with FLUKA for a δ-ray threshold of 30 keV, compared to the unrestricted stopping power from ESTAR database [BERGER2005].

5.4.3. Implementation with FLUKA

The FLUKA implementation consisted of the following points:

- *Beam sources*. Three types of sources were implemented: monoenergetic pencil beams of different energies, SOBPs constructed by adding monoenergetic pencil beams of different energies with the same transversal coordinates, and cubic volumes. The SOBPs and cubic volumes were constructed using the treatment planning software TRiP [KRAMER2000, KRAMER2000A]. The FLUKA subroutine *source.f* was modified to read TRiP treatment plan files (in rst format).

- *Geometry*. A simple geometry consisting of a cubic volume of water in vacuum was used, simulating the water phantom.

- *Physics configuration*. The physics settings were configured as described in chapter 4, including an I-value of 78 eV for water. A delta ray threshold of 30 keV was set with DELTARAY card. With this configuration, about 10% of the energy is deposited discretely by explicitly tracked delta electrons. Transport cut-offs for electrons was also set at 30 keV using EMFCUT card.

- *Scoring*. Four overlapping three-dimensional USRBIN meshes were created into the treatment field, with a voxel size of 2 mm in the transversal directions and one third of a mm in the longitudinal direction. USRBIN detectors were configured to score track length fluence per voxel for all charged particles (ALL-CHAR option). When a particle hits a voxel, its track-length fluence within the bin is scored in the four meshes and multiplied with the stopping power of the associated media, for the given particle energy. This is done by activating the card USRWEI and modifying the subroutine *fluscw.f* to read from the previously calculated stopping power tables and interpolate them to obtain the multiplication factor.

  The introduced USRBIN scorers *fluw* and *fluair* contain, for a voxel at a position $\vec{r}$, the quantities $\sum_i \int_0^\infty \Phi_{E,i,w}(\vec{r}) \cdot (S_i(E)/\rho)_w \, dE$ and $\sum_i \int_0^\infty \Phi_{E,i,w}(\vec{r}) \cdot (S_i(E)/\rho)_{air} \, dE$, respectively. The quantity scored by *fluw*, the sum of track length fluence in water multiplied by stopping power of water, is by definition the deposited dose of the particle. In order to ensure the consistency of the code, a dose scorer was also configured, overlapping with the *fluw* scorer. As expected, both scorers yielded the same values, with only a minor discrepancy, mainly caused by neglecting energy depositions from track-ends in the *fluw* scorer. Figure 5.14 shows an example of this verification for the three pristine Bragg peaks considered.

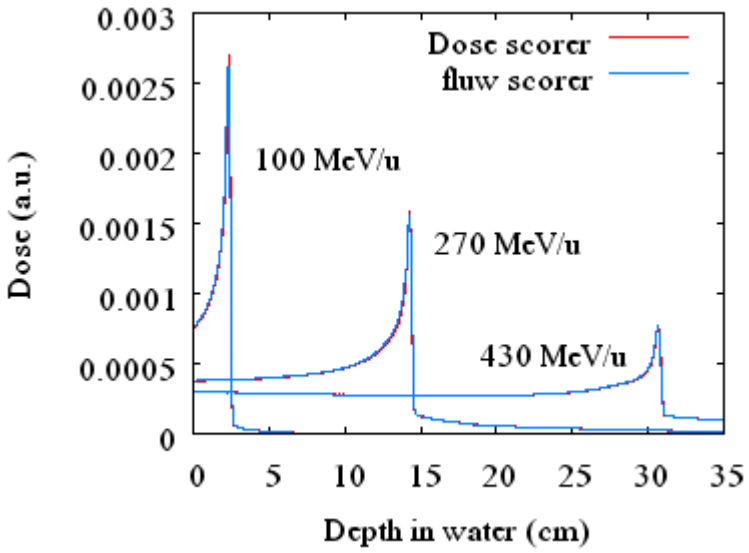

Figure 5.14. Comparison of dose and *fluw* scorers, yielding similar depth dose distributions, for three pristine 12C Bragg peaks

- *Running*. The user interface FLAIR [VLACHOUDIS2009] was used to conduct the simulations. Simulation time (on a HP xw9400 workstation, 1 x Six-Core AMD Opteron Processor 2427, 8 GB memory) was of the order of 2 s per primary particle (running on a single core). Total particle numbers of the order of 10^6 primaries were used, depending on the specific simulation.

- *Post-processing*. The usual FLUKA approach was used to estimate statistical uncertainties, by splitting the number of primaries into 5 to 10 separate independent runs, and combining the results using the subroutines *usbsuw* and *usbrea*. The resulting usrbin files were combined with a script in order to obtain $s_{w,air}(\vec{r})$ as *fluw* $(\vec{r})$ divided by *fluair* $(\vec{r})$.

5.4.4. Results

5.4.4.1. Longitudinal variation of $s_{w,air}$ in pristine peaks

Three monoenergetic pencil beams of 100.07, 270.55 and 430.10 MeV/u were simulated. The results are shown in Figure 5.15. As expected, the stopping power ratio grows steadily along the plateau area and hits its highest point towards the distal edge of the Bragg peak. The experimental values measured in section 5.3 are also shown in the plot. The three peaks show a very similar behaviour, regarding the dependence of $s_{w,air}$ with the residual range, as it can bee seen in Figure 5.17. The residual range has been calculated using a definition for the practical range R_p at the 25% level. The main observable difference is in the tail region ($R_{res} < 0$), and it is due to the increasing importance of nuclear fragmentation with increasing initial beam energy, resulting in an increase amount of long ranging light fragments in the dose tail beyond the Bragg peak.

5.4.4.2. Longitudinal variation of $s_{w,air}$ in SOBPs

When several pristine peaks are combined together to form a spread out Bragg peak, the peaks in the $s_{w,air}$ towards the distal edge of the field will merge, and thus the combined raise effect is expected to be smaller than for single pristine peaks. Previous works have reproduced this effect, as explained in section 5.1.

We calculated the water-to-air stopping power ratio in nine SOBPs at depths of 5, 15 and 25 cm in water, with sizes of 10, 30 and 50 mm. The spread out Bragg peaks were generated with the GSI treatment planning software TriP [KRAMER2000, KRAMER2000A]. The results, displayed in Figure 5.16, show a very slight bump at the beginning of the SOBP (corresponding to the most proximal peaks), and the expected raise at the distal end.

It is interesting to plot these data together as a function of the residual range (Figure 5.17). From this figure, we can conclude that the influence of the width and depth of the SOBP is minimal, with the only relevant effect being the aforementioned raise at residual ranges close to zero.

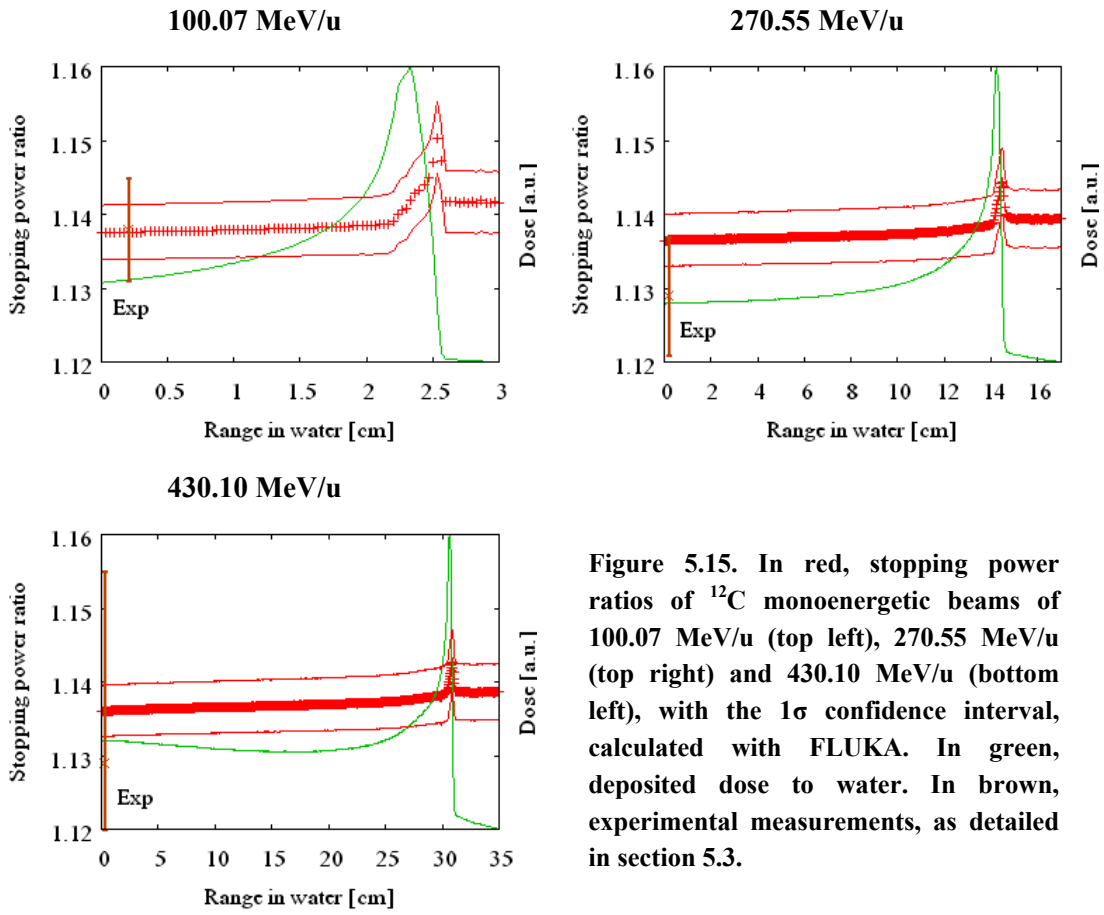

Figure 5.15. In red, stopping power ratios of ^{12}C monoenergetic beams of 100.07 MeV/u (top left), 270.55 MeV/u (top right) and 430.10 MeV/u (bottom left), with the 1σ confidence interval, calculated with FLUKA. In green, deposited dose to water. In brown, experimental measurements, as detailed in section 5.3.

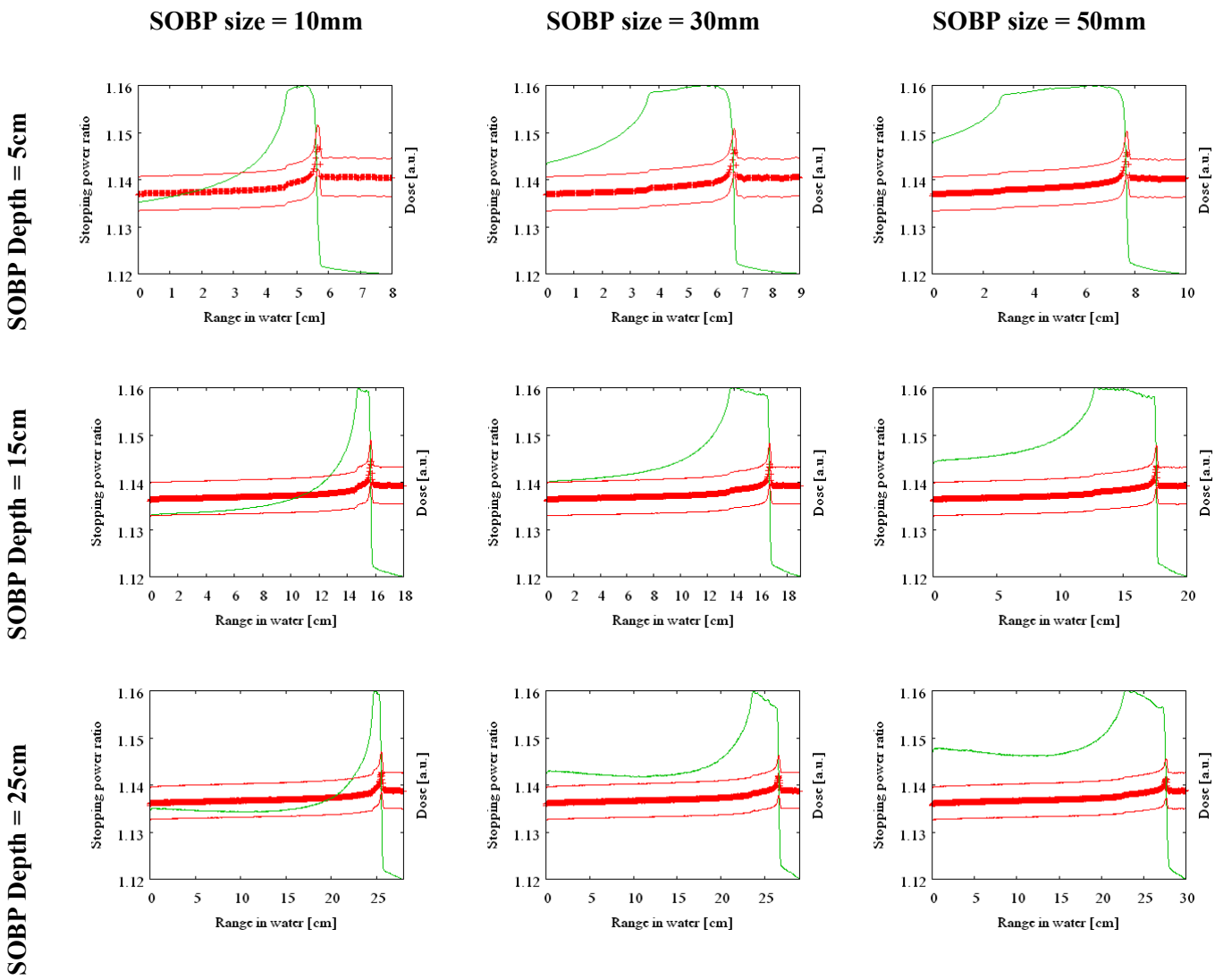

Figure 5.16. In red, stopping power ratios of SOBPs of ^{12}C of different depths and sizes, with the 1σ confidence interval, calculated with FLUKA. In green, deposited dose to water.

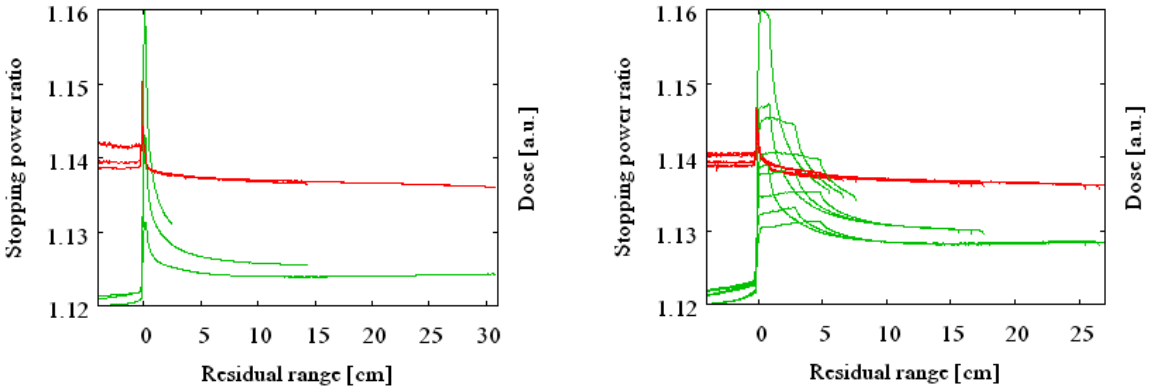

Figure 5.17. $s_{w,air}$ (in red) and depth dose distribution (in green) for pristine peaks of 100.07, 270.55 and 430.10 MeV/u (left) and for nine ^{12}C SOBPs in water (right), plotted as a function of residual range, calculated with FLUKA.

5.4.4.3. Transversal variation of $s_{w,air}$

Provided that there is charge particle equilibrium (or the lateral dose is integrated, as it happens, for example, in the PeakFinder detector; see section 3.2.2), the longitudinal variation of $s_{w,air}$ with residual range can be studied only in one dimension, as it has done in previous sections. However, real treatment plans take place in three dimensions, and before a description of $s_{w,air}$ in terms of residual range is adopted, transversal variations have to be ruled out. The calculations in [LUHR2011] already show that no relevant effects are expected in the transversal directions. We simulated the scanned irradiation in water of a plan delivering a homogeneous dose inside a cube of 3 cm side, situated at a depth of 50 mm. They were created with TriP with a lateral distance of 2 mm between raster points and the physical base data from HIT [PARODI2012].

The results of such calculation are displayed in Figures 5.18 to 5.21. As expected, no substantial variations in the transversal directions are observed in the horizontal or in the vertical plane. A description of $s_{w,air}$ depending on the residual range, like the one which we present in section 5.5, is therefore valid to represent the complete field, at least for an extended homogeneous dose distribution. More realistic patient plans will be addressed in the next chapter.

5.4.5. Discussion

In terms of statistical uncertainties, the statistical errors in the fluence scorers *fluw* and *flua* were of the order of 0.5%, for each voxel. However, since *the same* tracks were used to calculate *fluw* and *flua*, numerator and denominator of equation (5.1), the statistical fluctuations in the fluence had a very small effect on $s_{w,air}$, as it was calculated as a ratio between sums of scored track lengths. The Monte Carlo statistical errors of $s_{w,air}$ were negligible, compared to the uncertainty in the I-values.

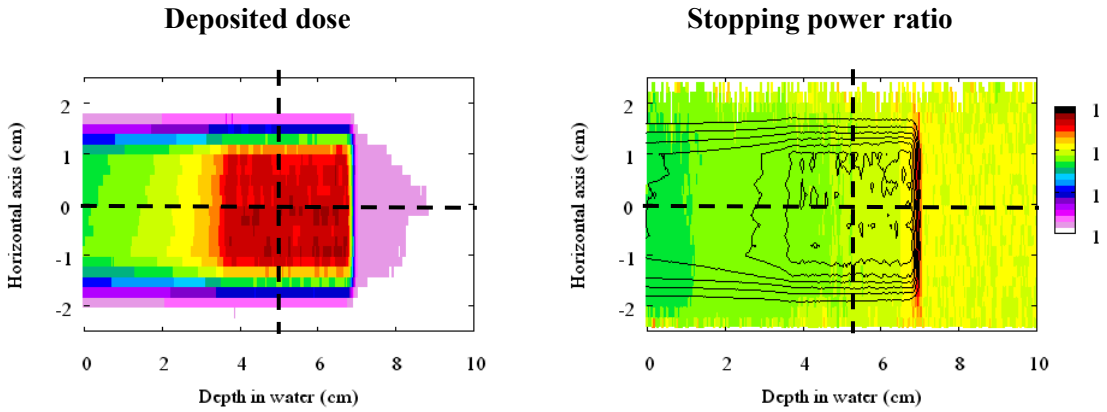

Figure 5.18. FLUKA calculations for deposited dose (left) and $s_{w,air}$ (right) for a cubic volume of homogeneous dose in water irradiated with ^{12}C. Horizontal slice in the XZ plane for y=0 cm (the plan is centred at the point {0,0,5}, in cm). Contours in the $s_{w,air}$ plot represent isodose lines.

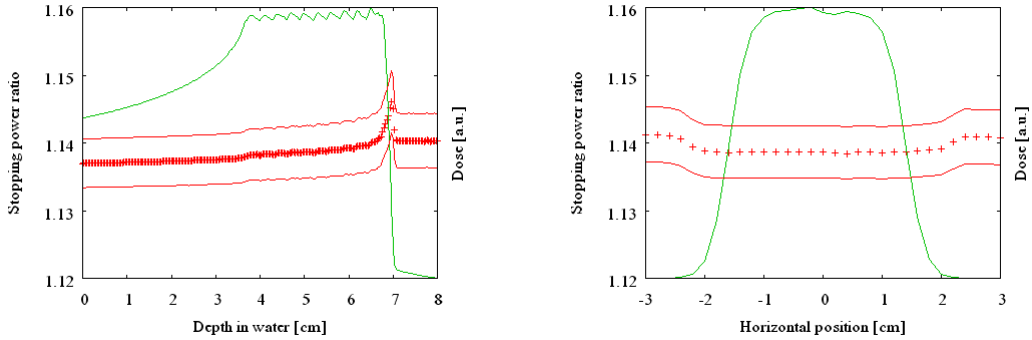

Figure 5.19. One-dimensional plots showing $s_{w,air}$ and deposited dose for the longitudinal axis (left) and the transversal axis (right), corresponding to the profiles marked by the dashed lines on Figure 5.18.

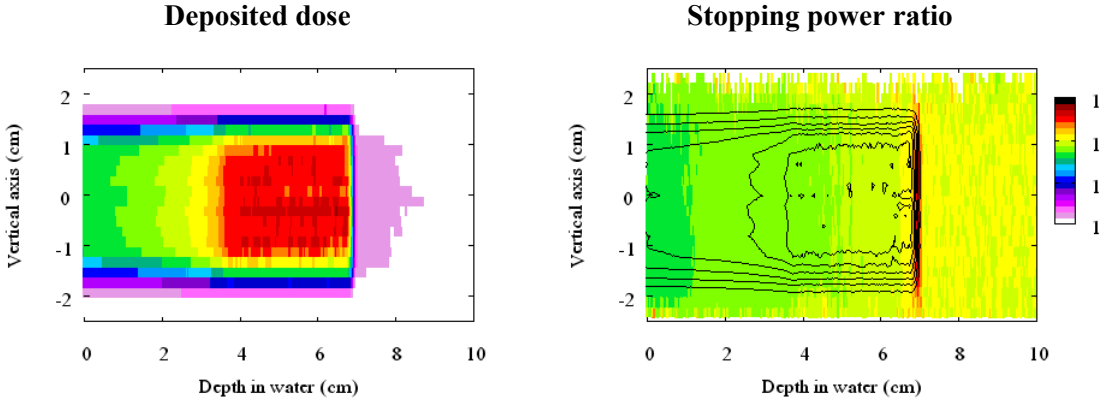

Figure 5.20. FLUKA calculations for deposited dose and $s_{w,air}$ for a cubic volume of homogeneous dose in water irradiated with ^{12}C. Vertical slice in the YZ plane for x=0 cm (the plan is centred at the point {0,0,5}, in cm). Contours in the $s_{w,air}$ plot represent isodose lines.

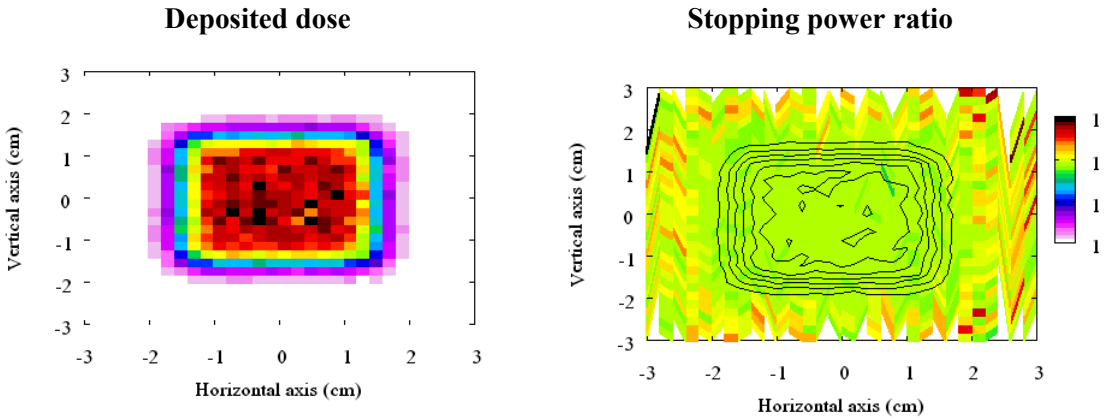

Figure 5.21. FLUKA calculations for deposited dose and $s_{w,air}$ for a cubic volume of homogeneous dose in water irradiated with ^{12}C. Beam's eye view slice in the XY plane for z=5 cm (the plan is centred at the point {0,0,5}, in cm). Contours in the $s_{w,air}$ plot represent isodose lines.

At the view of the results of [MEDIN1997], we investigated on the effect of delta ray tracking in $s_{w,air}$,. The calculation of stopping power ratio for pristine peaks shown in section 5.4.4.1 was repeated, using unrestricted stopping power tables for air and water (extracted from the FLUKA output) and turning off delta ray generation and tracking. The results, shown in Figure 5.22, reproduces the previous work: calculating $s_{w,air}$ without delta ray tracking yields lower values and a less homogeneous distribution, with differences up to 1% in the plateau area. Thus, the results of any MC $s_{w,air}$ calculation are conditioned by the choice of the delta-ray threshold. As this value should be adapted to match the range of electrons with the cavity size, there is no "single" correct solution to the problem, which has to be considered independently for different cavity sizes. For instance, the experimental data shown in Figure 5.22 approximates to the $s_{w,air}$ calculated with unrestricted stopping power values, since in the measurements the $s_{w,air}$ were derived from energy losses instead of from energy depositions. The air gap acted like an infinite ionization chamber, integrating over all dose depositions from delta electrons. Another example on how the finite size of the chambers can influence the observed water-to-air ratio is given in section 6.3.3.

Therefore, the Monte Carlo calculations shown in this section are bound to a delta ray threshold of 30 keV, corresponding to a range of electrons in air of about 1 cm [BERGER2005]. This value, as discussed previously, was chosen because of a number of practical reasons, including computation speed (the full calculation with delta ray tracking at 30 keV takes more than three times than the calculation with unrestricted stopping powers, and computation time increases dramatically as the threshold is decreased). Therefore, care must be taken when interpreting the calculations shown, as well as the derived results which will be presented in the following sections.

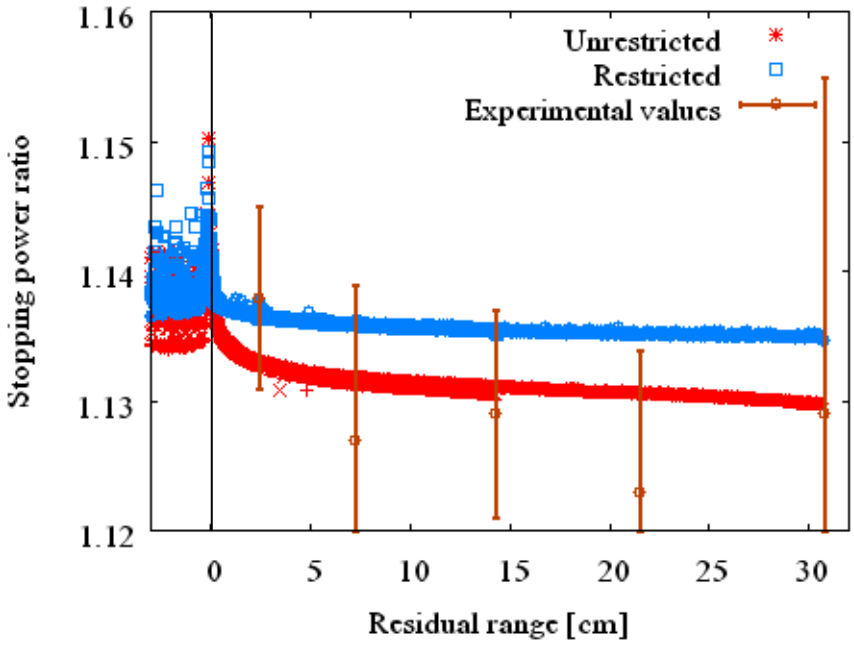

Figure 5.22. FLUKA calculation of $s_{w,air}$ versus residual range, for three monoenergetic ^{12}C beams of 100.07, 270.55 and 430.10 MeV/u using a delta ray threshold of 30 keV (blue), and from unrestricted stopping power tables, with no delta ray tracking at all (red). In brown are shown the experimentally measured values (cf. section 5.3).

5.5. An empirical expression for water-to-air stopping power ratio

As justified in the previous sections, it is possible to find an expression for $s_{w,air}(R_{res})$ which describes the behaviour of the stopping power ratio for a complete ^{12}C treatment field. The raise of $s_{w,air}$ at the distal edge of the peak can be reproduced by the following equation,

$$s_{w,air}(R_{res}) = \begin{cases} s_0, & R_{res} + \varepsilon \le 0 \\ s_0 + b\ln(R_{res} + \varepsilon), & R_{res} + \varepsilon > 0 \end{cases}, \qquad (5.11)$$

where R_{res} is defined at the 25 % level ($R_{res} = R_{25} - z$) and expressed in cm, and the parameter ε represents the distance between the point with $R_{res} = 0$ and the observed maximum.

The values of the parameters were obtained by fitting the $s_{w,air}$ calculated with FLUKA for different SOBPs (Figure 5.17) using the plotting program *gnuplot*. The upper and lower limits for the 1σ-confidence interval (shown for every SOBP in Figure 5.16) were also fit, in order to derive the uncertainty for the parameters and propagate correctly the uncertainty for the individual values of $s_{w,air}(R_{res})$. The resulting values of the parameters are shown in Table 5.7.

For each of the parameters (s_0, b and ε), the combined standard uncertainty is calculated adding two components quadratically. The first component $(u(\overline{s_0}), u(\overline{b})$ and

$u(\bar{\varepsilon})$ respectively) is the standard uncertainty of the fit with I_w=78.0 and I_{air}=90.2, enclosing the dependence with peak size and depth.

The second component is the difference between the fit values calculated with the boundary I-values. Combining both uncertainties, the values of the parameters can be expressed as s_0 = 1.1391 ± 0.0037, b = (9.5 ± 1.5)·10^{-4} and ε = (8.53 ± 0.39)·10^{-2} cm. Figure 5.23 shows the match between the stopping power ratios calculated with equation (5.11) and the FLUKA-calculated $s_{w,air}$ values.

The application of this empirical model represents an improvement with respect to the currently recommended value of 1.13 with a 2% uncertainty, from TRS-398 [IAEA2000], as illustrated in Figure 5.24. However, as it was already mentioned, care needs to be taken when using this expression in situations when the chosen Spencer-Attix threshold value of 30 keV for electrons might not be appropriate. In those cases, a further study or a raise of the uncertainty margins is recommended.

	I_w = 78.0 eV ***I_{air} = 90.2 eV***	*I_w = 78.0 eV* *I_{air} = 88.4 eV*	I_w = 78.0 eV I_{air} = 92.0 eV
$\bar{s}_0$	***1.1391***	*1.1428*	*1.1354*
$u(\bar{s}_0)$	***0.0004***	*0.0004*	*0.0004*
$\bar{b}$	***$9.5\cdot10^{-4}$***	*$11.0\cdot10^{-4}$*	*$8.0\cdot10^{-4}$*
$u(\bar{b})$	***$0.36\cdot10^{-4}$***	*$0.37\cdot10^{-4}$*	*$0.35\cdot10^{-4}$*
$\bar{\varepsilon}$ [cm]	***0.0853***	*0.0842*	*0.0866*
$u(\bar{\varepsilon})$ [cm]	***0.0037***	*0.0036*	*0.0037*

Table 5.7. Average parameters for the fits of nine ^{12}C SOBPs to equation (5.11) for three different sets of water and air I-values.

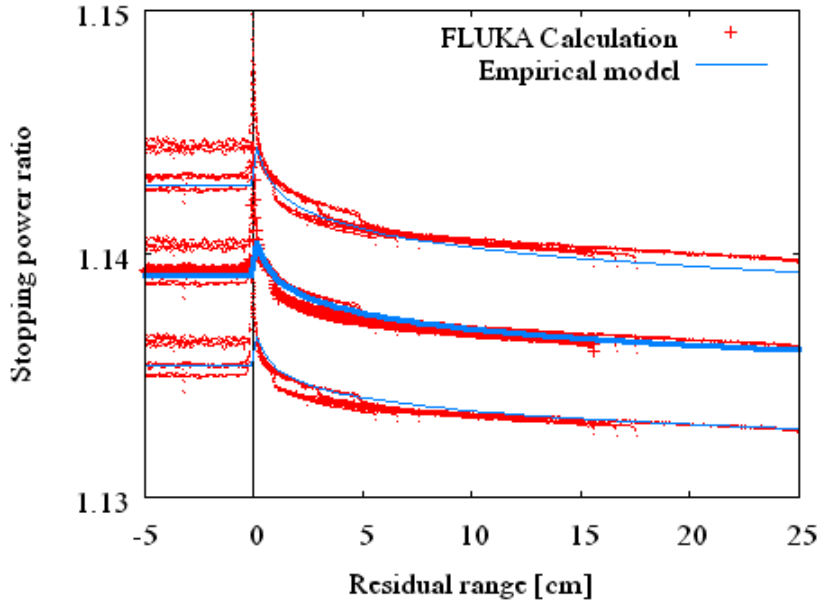

Figure 5.23. $s_{w,air}$ calculated with expression (5.11) (blue solid line), with fit parameters obtained from FLUKA calculated stopping power ratios (red dots) for nine ^{12}C SOBPs.

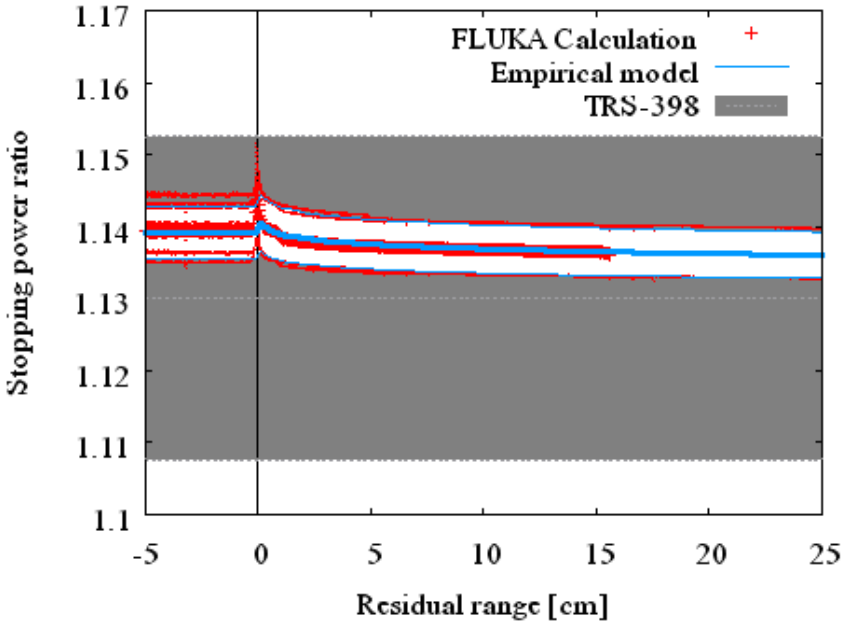

Figure 5.24. Comparison of the 1σ-confidence interval for $s_{w,air}$ given from the proposed expression (blue lines over white area), and the currently recommended value from TRS-398 [IAEA2000] (grey area).

CHAPTER 6 Monte Carlo study on plan verification with ionization chambers

6.1. Plan verification with an ionization chamber matrix

A described in detail in section 3.4.2, the delivery of treatment plans is often verified with a matrix of ionization chambers immerse in a water phantom (see Figure 3.4 on page 35). The treatment planning system performs a forward calculation of the plan to derive the expected dose that the chambers will collect in the irradiation, and those values are compared with the measured values. A discrepancy of 5% is allowed to consider a plan delivery successful [KARGER1999]. The plan verification tool is usually integrated in the TPS software (see Figure 6.1), interfacing with the data acquisition software of the ionization chamber matrix.

The Monte Carlo code presented in the previous chapters was used to study possible effects in treatment plan verification with the ionization chamber matrix. In this chapter, effects derived from the $s_{w,air}$ distribution, and possible physical crosstalks between ICs are addressed.

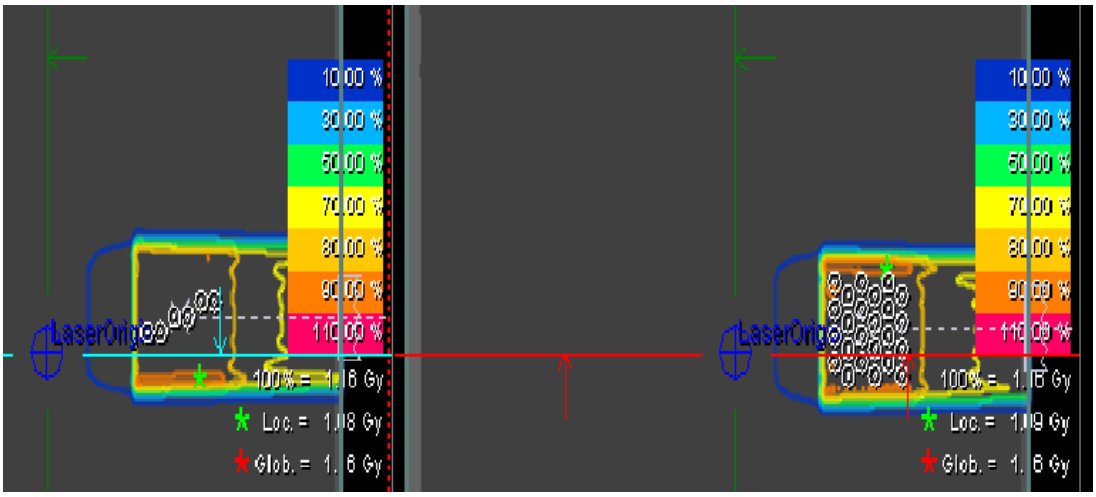

Figure 6.1 Snapshot of the plan verification interface from the TPS software (Syngo PT Planning, Siemens Particle Therapy) in use at the Siemens Test Centre Marburg. The white circles represent the positions of the ionization chambers in the matrix, inside the water phantom.

6.2. Water-to-air stopping power ratio in full patient plans

6.2.1. Introduction

The variation of $s_{w,air}$ with the position in the treatment field was studied in detail in the previous chapter, for pristine peaks, SOBPs, and homogeneous three-dimensional dose

distributions. Using the calculated $s_{w,air}$ distributions and the measurements, expression (5.11) was derived to model the variation of stopping power ratio with residual range. This expression could be directly used for the calculation of the IC quality factor for dosimetry under reference conditions (cf. chapter 3), where a homogeneous field is used and the practical range can be easily established. However, further work needs to be done in order to implement such model into a treatment plan verification scheme, since the residual range changes between plans and between different positions inside the same plan.

This section presents the calculation of 3D $s_{w,air}$ plans for real treatment fields, corresponding to two patients treated at HIT. The first one (Figure 6.2, left) corresponds to a head-and-neck tumour of average size, while the second one (Figure 6.2, right) is a patient with a tumour in the pelvic region, for which the target volume is remarkably large. Apart from the target size, there is a main difference in terms of depth: while for the first patient the beam needs to penetrate only a few centimetres into the body, the second one has the target at a deep position, which requires to be higher energy beams and implies that the particles travel a longer path inside the body, suffering from more fragmentation and scattering.

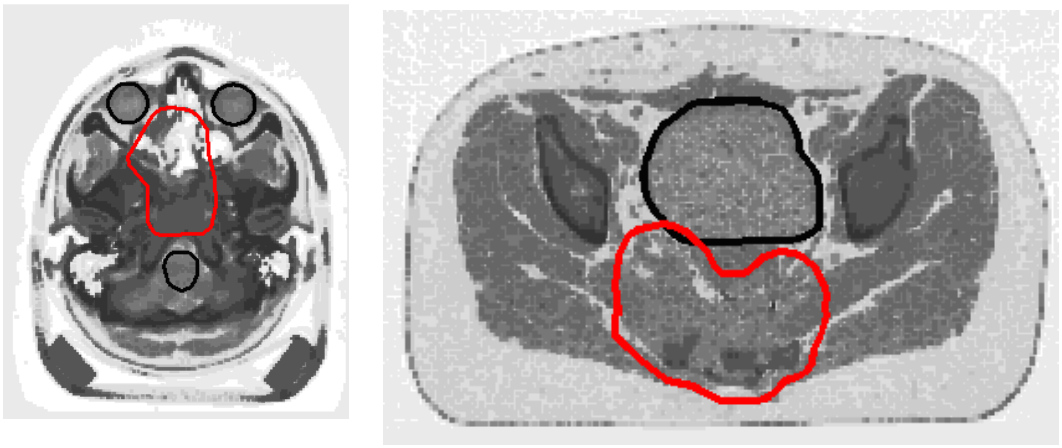

Figure 6.2. CT images and delineation of target volumes (red) and organs at risk (black) for a head-and-neck patient (patient #1, left) and a pelvic patient (patient #2, right)

6.2.2. 3D Stopping power ratio maps

The Monte Carlo code FLUKA, with the same settings described in section 5.4, was used to calculate $s_{w,air}$ maps. Since plan verification is done individually for each treatment field (a treatment is usually composed of several fields), only one field from each patient case was simulated.

6.2.2.1. Patient #1

Figure 6.3-6.6 show different projections for deposited dose and $s_{w,air}$ for the irradiation of a single field of the first patient plan. No distinctive effects have been observed in comparison with the irradiation of simple homogeneous plans, described in section 5.4.4.

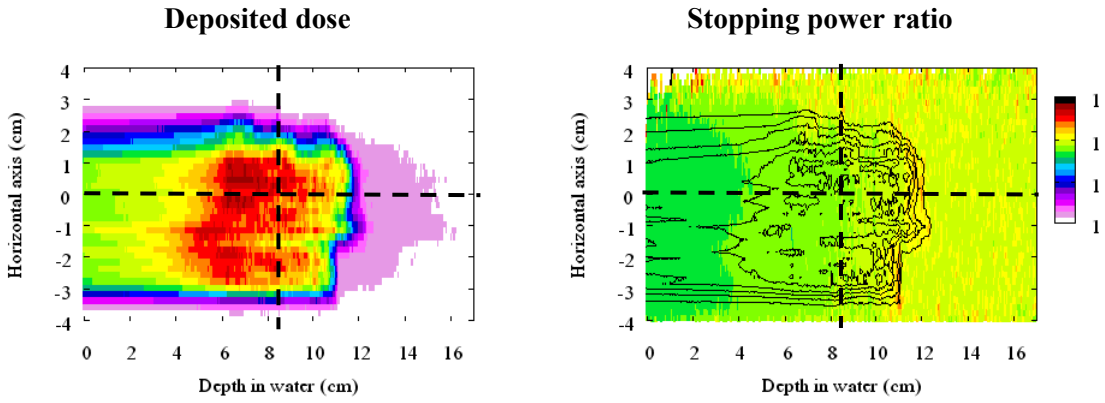

Figure 6.3. FLUKA calculations for deposited dose and $s_{w,air}$ for the plan verification of one field of patient treatment plan #1, irradiated with ^{12}C in water. Horizontal slice in the XZ plane for y=0 cm. Contours in the $s_{w,air}$ plot represent isodose lines.

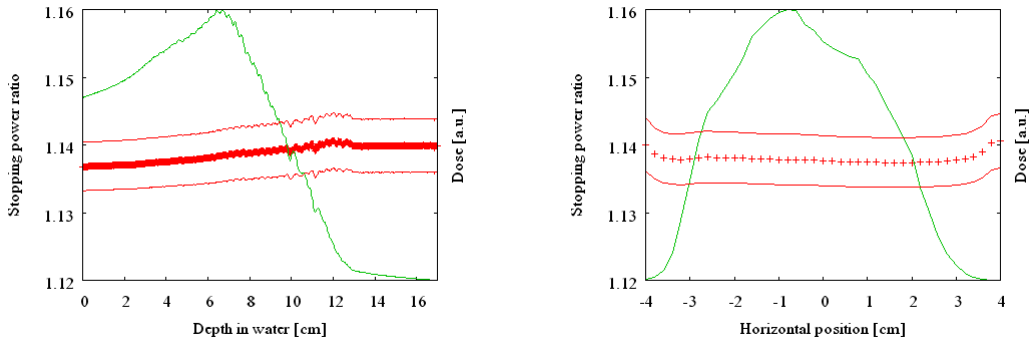

Figure 6.4. One-dimensional plots showing $s_{w,air}$ and deposited dose for the longitudinal axis (left) and the transversal axis (right), corresponding to the profiles marked by the dashed lines on Figure 6.3.

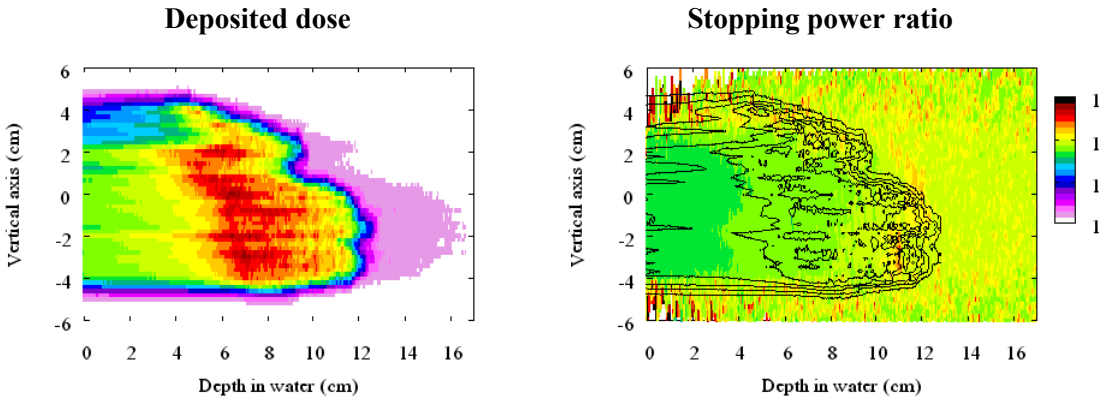

Figure 6.5. FLUKA calculations for deposited dose and $s_{w,air}$ for the plan verification of one field of patient treatment plan #1, irradiated with ^{12}C in water. Vertical slice in the XY plane for x=0 cm. Contours in the $s_{w,air}$ plot represent isodose lines.

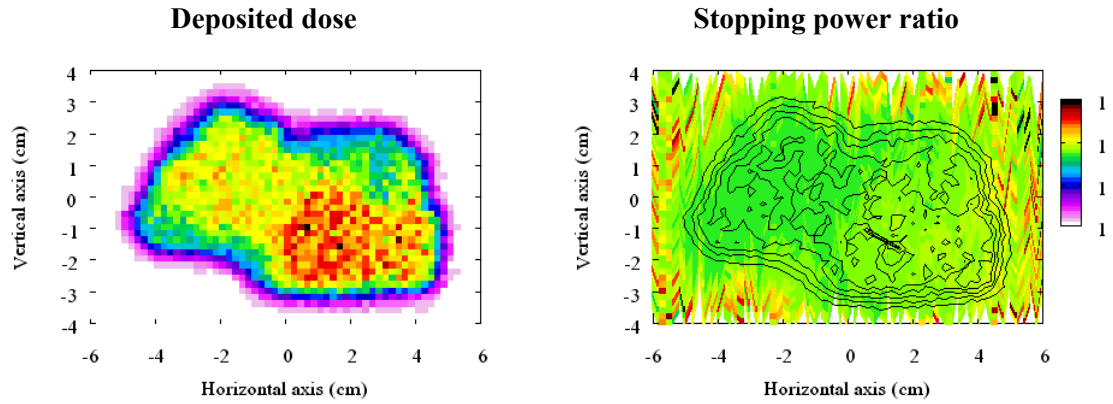

Figure 6.6. FLUKA calculations for deposited dose and $s_{w,air}$ for the plan verification of one field of patient treatment plan #1, irradiated with ^{12}C in water. Beam's eye view slice in the XY plane for z=8.2 cm. Contours in the $s_{w,air}$ plot represent isodose lines.

6.2.2.2. Patient #2

Similar results are shown for the second patient plan (figures 6.7-6.10), exhibiting a slight raise towards the distal edge of the target volume, and no remarkable effects in the transversal directions. Similarly, the increased energies and higher number of fragments present on the second plan do not seem to alter the $s_{w,air}$ calculation significantly.

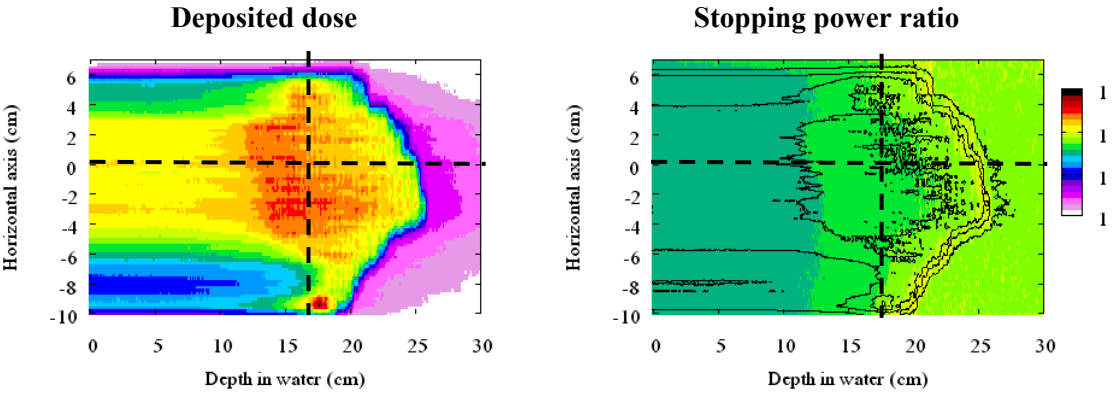

Figure 6.7. FLUKA calculations for deposited dose and $s_{w,air}$ for the plan verification of one field of patient treatment plan #2, irradiated with ^{12}C in water. Horizontal slice in the XZ plane for y=0 cm. Contours in the $s_{w,air}$ plot represent isodose lines.

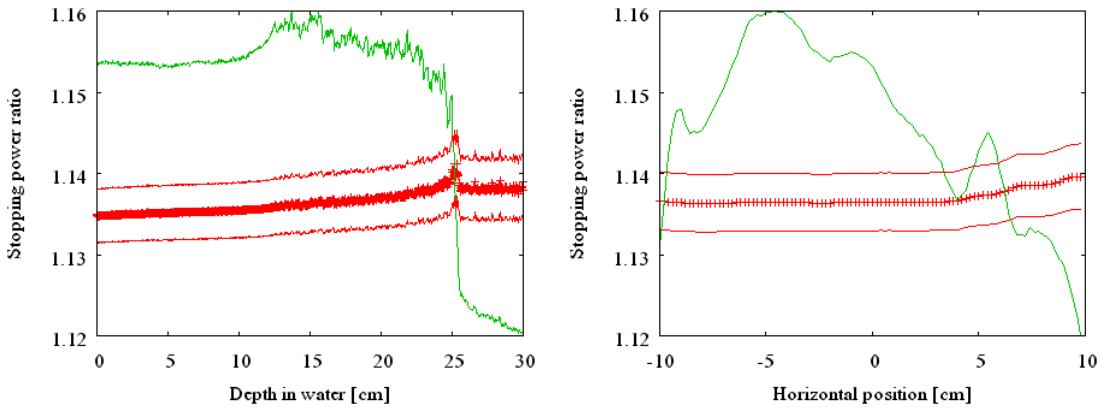

Figure 6.8. One-dimensional plots showing $s_{w,air}$ and deposited dose for the longitudinal axis (left) and the transversal axis (right), corresponding to the profiles marked by the dashed lines on Figure 6.7.

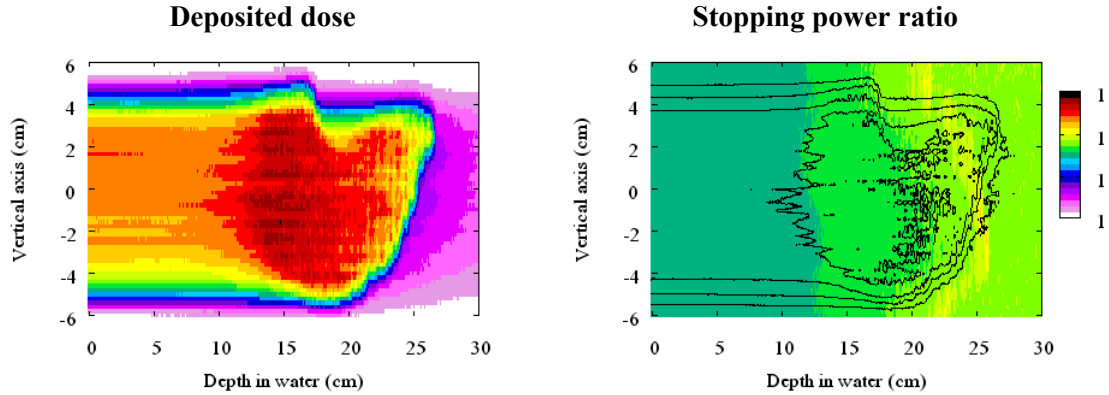

Figure 6.9. FLUKA calculations for deposited dose and $s_{w,air}$ for the plan verification of one field of patient treatment plan #2, irradiated with ^{12}C in water. Vertical slice in the XY plane for x=0 cm. Contours in the $s_{w,air}$ plot represent isodose lines.

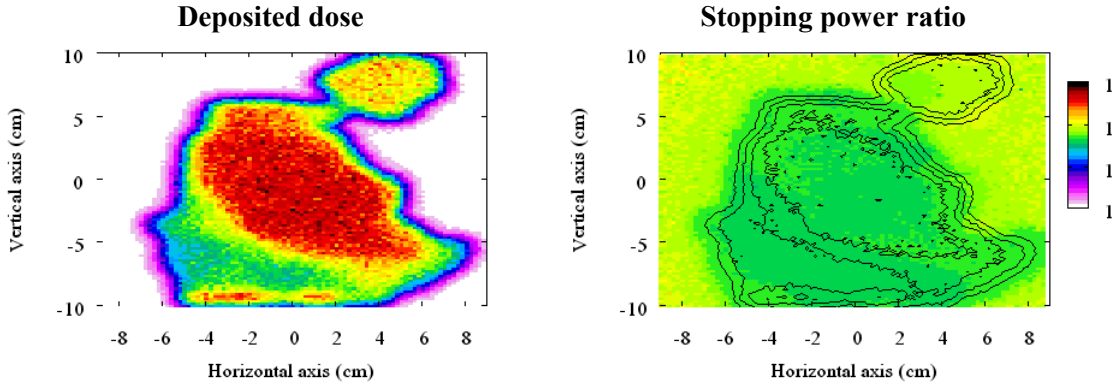

Figure 6.10. FLUKA calculations for deposited dose and $s_{w,air}$ for the plan verification of one field of patient treatment plan #2, irradiated with ^{12}C in water. Beam's eye view slice in the XY plane for z=16.5 cm. Contours in the $s_{w,air}$ plot represent isodose lines.

6.2.3. Application of empirical expression to plan verification

In order to apply expression (5.11) to calculate correction factors for plan verification with ionization chambers, an adaptation of the concept of "residual range" needs to be developed. Here an implementation is presented, which can be deployed as part of a treatment planning system with plan verification capability.

For every ionization chamber, the effective point of measurement is determined. This is a property of the chamber itself, which depends on its geometry and material composition. The transversal {x,y} coordinates of the effective point of measurement are then matched to the closest raster point from the treatment plan (Figure 6.11), with coordinates {x',y'}. For this raster point, the highest energy slice is chosen from the plan, and its range R_{25} looked up in a table, constructed previously from the physical base data. The residual range, as it appears in equation (5.11), is finally calculated as $R_{res}=R_{25}(x',y') - z$, where z is the longitudinal coordinate of the effective point of measurement.

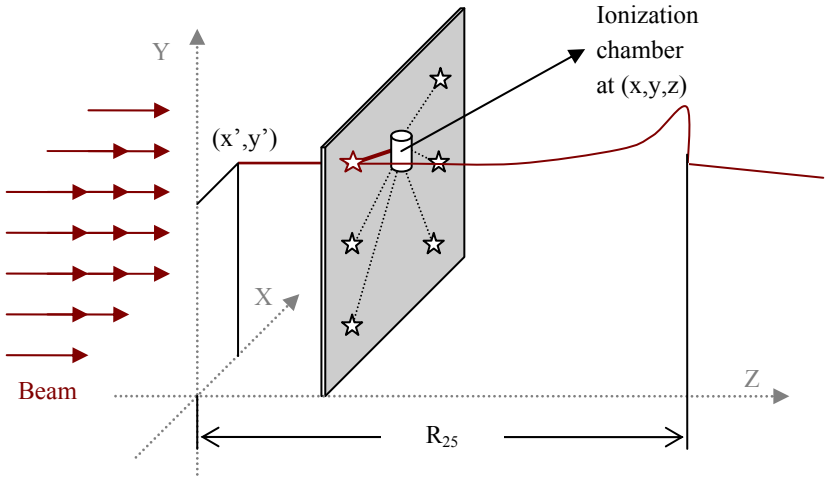

Figure 6.11. Scheme depicting the determination of the R_{25} reference point, depending on the effective point of measurement in the field.

To test the method, the stopping power maps calculated with FLUKA for a homogeneous cubic volume (section 5.4.4.3) and for two patient plans (previous section), were recalculated using the aforementioned algorithm at every voxel. The results are presented in the following way. The left panel of Figure 6.12 presents a visual comparison between the results of the full FLUKA calculation and the R_{res} model, for a horizontal slice of the treatment volume irradiated with the three different plans. As the figures show, the model can reproduce the three-dimensional variations of $s_{w,air}$ with considerable accuracy, only failing at reproducing very high $s_{w,air}$ and dose gradients, such as the distal part of the cubic volume in Figure 6.12, top.

In addition, each of the fields has been automatically divided into four parts (entrance channel, target, distal area and lateral areas) by analysing the irradiation plans. In a similar way as shown in Figure 6.11, for each raster point, the depth dose distribution from the physical base data is used to determine the 95% dose limits in the longitudinal direction, for the most distal and proximal energy levels. The portion of space with more than 95% of the

dose is marked as "target", the points situated before it (in the direction of the beam) are tagged as "entrance channel", and the points situated beyond the peak are marked as "distal edge". Finally, the voxels for which no raster point is defined in the transversal plane are labeled as "lateral". This classification is used to study the benefits of implementing the R_{res}– based model, in comparison to using $s_{w,air}$=1.13 for the complete field [IAEA2000]. The histograms displayed in the right panel of Figure 6.12 compare the differences between the $s_{w,air}$ values calculated with full FLUKA simulation, those obtained from the R_{res} model and the fixed value of 1.13 for the four parts of the field. For the three cases, the empirical model reproduces the Monte Carlo calculation with higher accuracy than the fixed value of $s_{w,air}$ =1.13. While an overall overestimation of underestimation of all $s_{w,air}$ values is possible (i.e. a global shift to all histograms in Figure 6.13), due to the uncertainties the I-values or to an inappropriate choice of delta ray threshold (cf. discussion in section 5.4.5), it is clear that the empirical model can reproduce consistently the variations of $s_{w,air}$ within the field, as calculated by the MC.

6.3. Monte Carlo study of the plan verification IC matrix

6.3.1. Modelling ionization chambers and detector block with FLUKA

The geometry of the detector block used for plan verification was modelled with FLUKA combinational geometry. On a first step, ionization chamber PTW model 31015 [PTW2009] was modelled (see Figure 6.14) according to the technical drawings. The materials used in its composition were dry air, aluminium and PMMA, from the FLUKA standard material database. No electric field was implemented in the geometry.

24 of these chambers were built into the geometry, according to their nominal position in the detector block (see Figure 6.15), centred at the reference position {0,0,0}.The final position of the IC matrix was determined at execution time using a ROT-DEFI card in the FLUKA input file, which is applied using the directives $start_transform and $end_transform to the complete detector block.

The IC matrix is submerged in a block of water, whose density is set at 0.998 g/cm^3. In the immediate surroundings of the detector block (and also affected by the transform directive), a virtual water box is created. The aim of this structure is to be able to set a specific delta ray transport threshold of 30 keV inside this virtual box (and thus, affecting all IC chambers and ensuring charge equilibrium in the surroundings of the detectors), while turning off completely delta ray tracking outside the box. This reduces remarkably the simulation time, without compromising the precision of the simulation.

Apart from these geometrical changes, the FLUKA physics settings were set up as defined in the previous chapters.

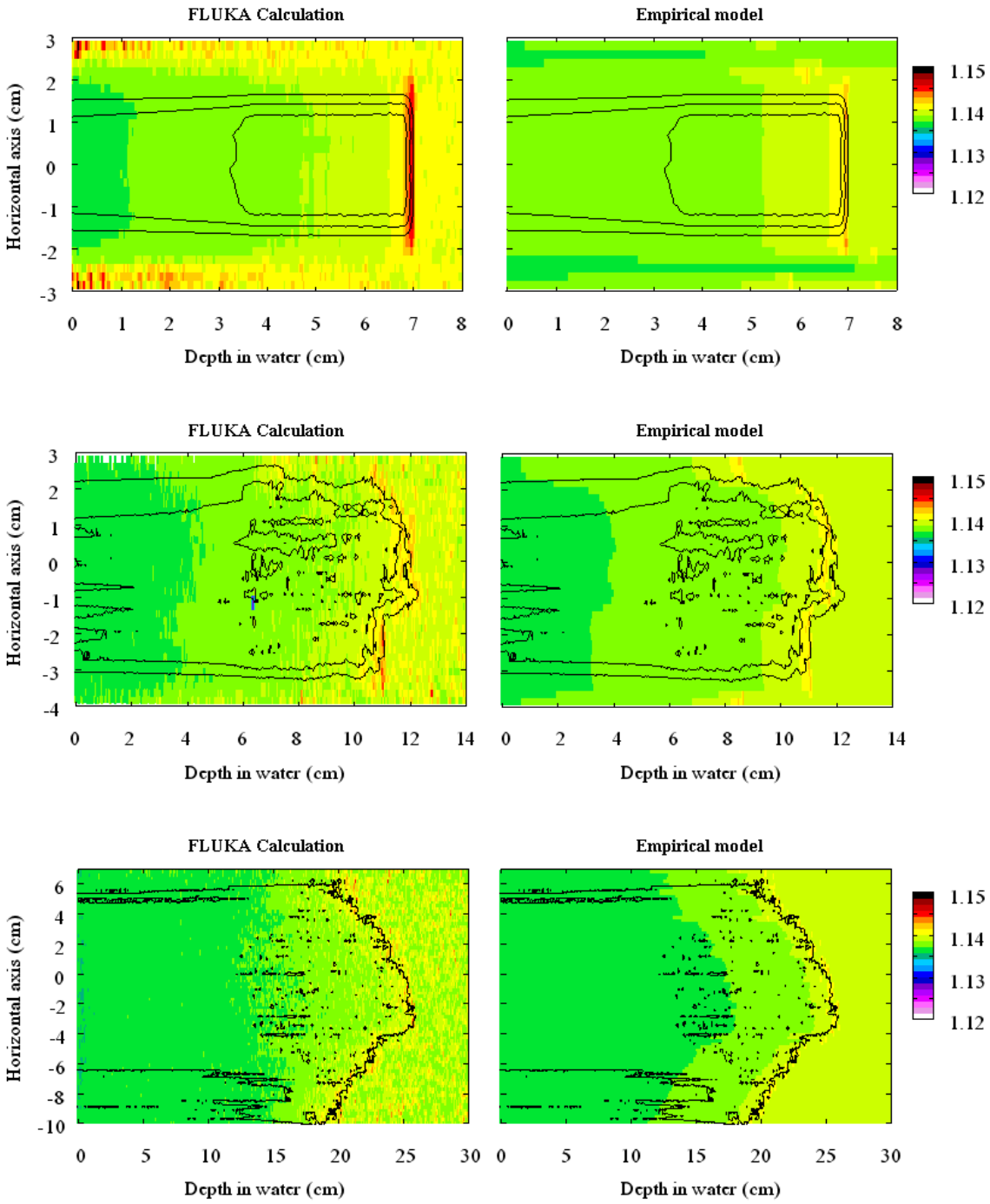

Figure 6.12. $s_{w,air}$ calculated with FLUKA simulation (left) and with the analytical algorithm described in section 6.2.3 (right), for a cubic volume (top), patient plan #1 (middle) and #2 (bottom).

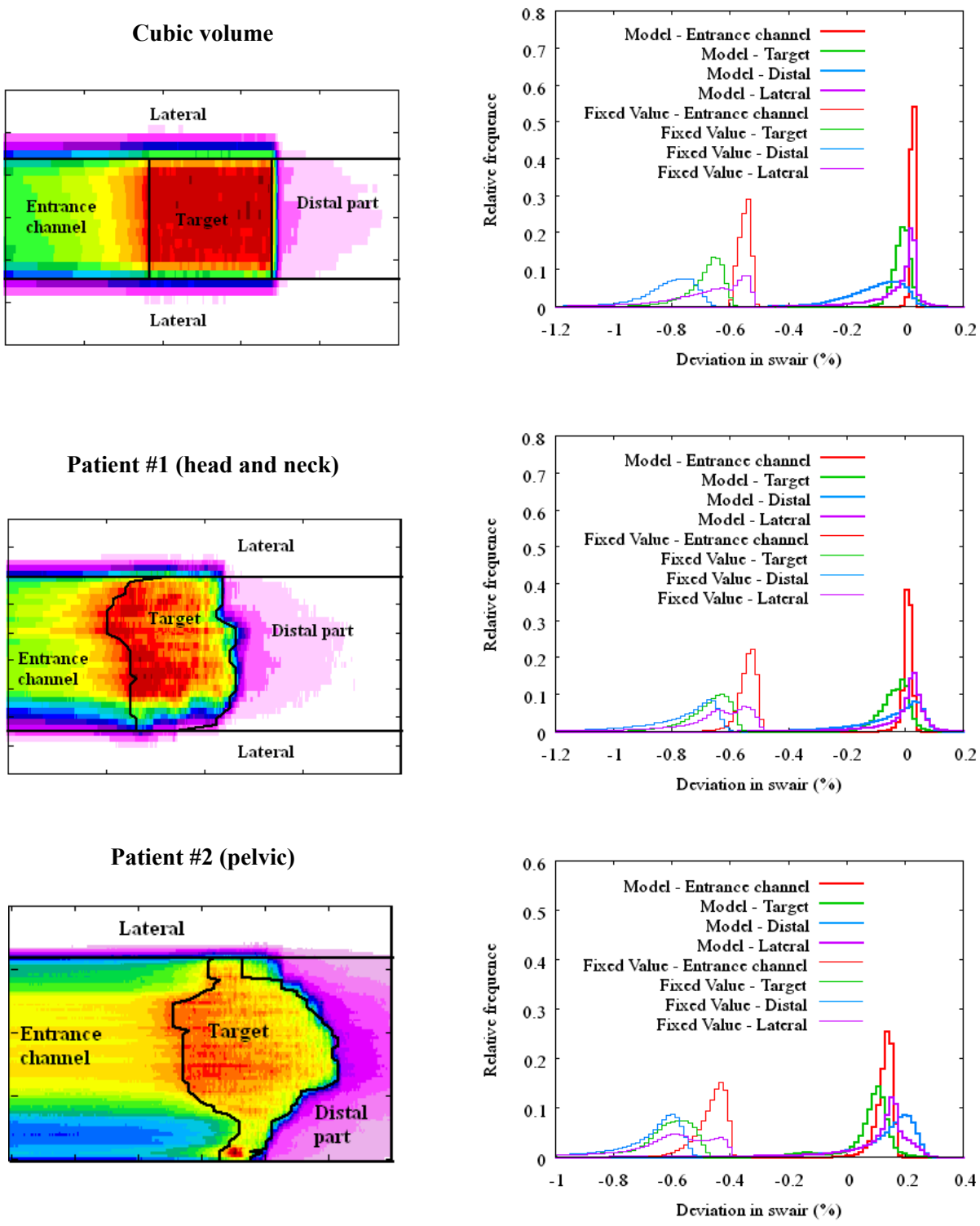

Figure 6.13. Dose distribution with automatic subdivision of treatment field (left) and histograms showing the distribution of errors in $s_{w,air}$ for the 4 parts in which the field is divided, comparing the $s_{w,air}$ values given by IAEA and the R_{res} model with the results of the full FLUKA calculation (right).

6.3.2. Physical crosstalks between IC chambers

The principle of the geometrical arrangement of the IC matrix is that the measured dose from different chambers inside the matrix does not affect each other. The assumption is that chambers behave as if they were surrounded only by water, with nothing perturbing the charge equilibrium or the particle fluence around them. From the original article where the device was proposed [KARGER1999] *"distortion of the dose distribution by introduction of the PMMA mounting into the water caused by scattering is negligible for heavy ions"*.

The goal of our study was to investigate whether any distortion exists when placing two ionization chambers at a close distance, in different angles with respect to the beam direction, and if such an effect exists, to determine at which distance it becomes relevant. Of course, only physical effects (scattered particles, distortion of particle fluence) can be studied in this manner; nothing can be said about possible electronic crosstalks at the readout circuitry.

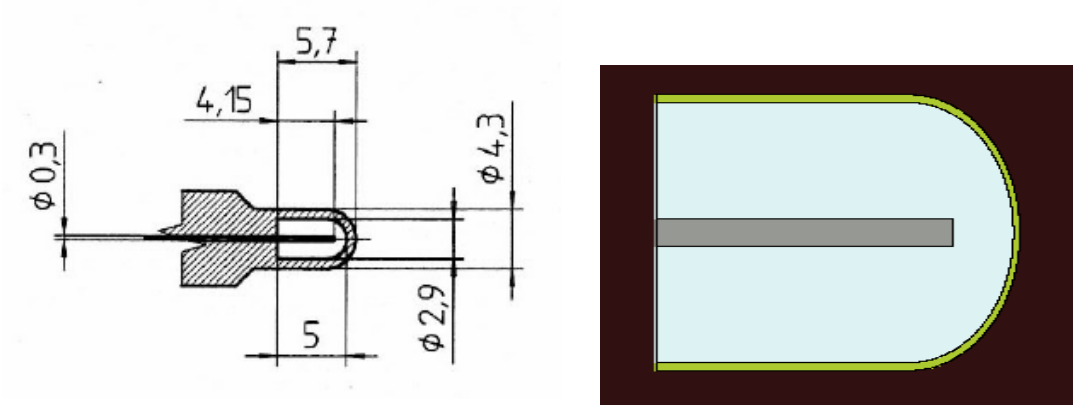

Figure 6.14. Technical drawings of PTW model 31015 [PTW2009] (left), and scheme of implementation with FLUKA combinational geometry (right).

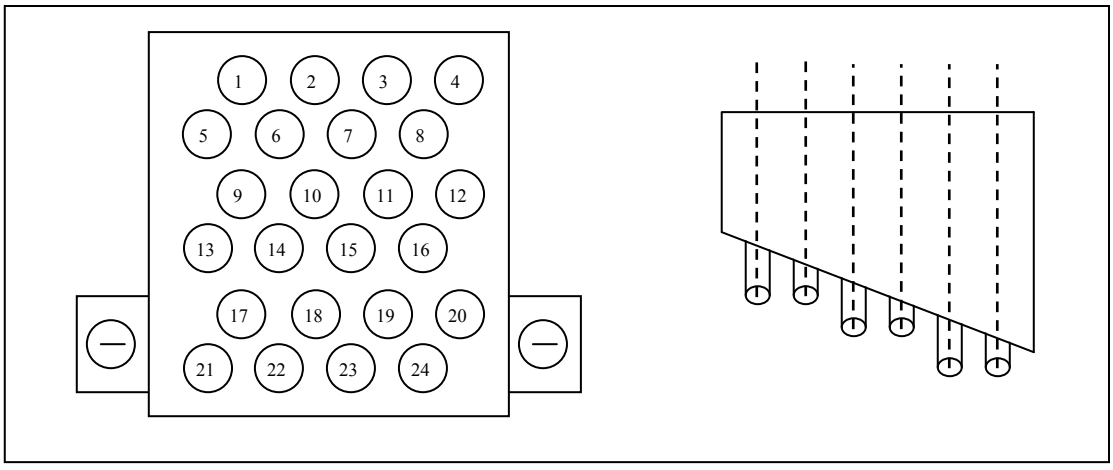

Figure 6.15. Upper (left) and lateral schematic views (right) of the detector block PTW Freiburg T21003 showing the 24 ionization chambers (PTW model 31015).

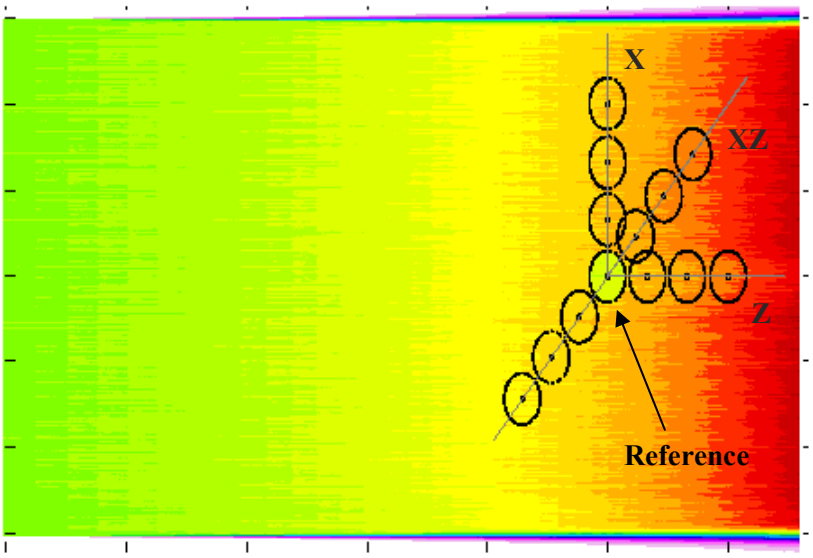

Figure 6.16. Test positions of the second chamber around the reference chamber in lateral, posterior, lateral-posterior and lateral-anterior directions. The colour wash display in the background shows the dose distribution for a 200 MeV/u ^{12}C beam extended homogeneously in the transversal directions (FLUKA simulation).

For this study, we simulated an ionization chamber (using the model of PTW 31015 chamber, depicted in Figure 6.14) placed at a depth of 5 cm inside a field composed of a 200 MeV/u ^{12}C beam, extended laterally and vertically to a 6x6 cm2 in the transversal plane. In the verification matrix, the distance between two chambers in the same plane is slightly higher than 1cm. The simulation was carried out repeated times, each time placing a second chamber next to the first one (at the side, behind, and diagonally) with at a distance between centres varying between 3 mm and 20 mm. Figure 6.16 shows a scheme of the positioning of the reference and test chambers at the different axes. In all cases, the chambers were placed in the same vertical plane.

For each repetition of the simulation, the dose deposited inside the air gap of the reference chamber was scored (using a region-based USRBIN scorer), and compared with the reference value, obtained for the first run with only the reference chamber in place. In order to obtain collect statistics, the number of primaries simulated for each run was raised to $5 \cdot 10^7$ (and up to 10^8 for the reference run), which yielded a relative statistical uncertainty of about 0.1% in the chamber dose. However, after running simulations by a total of about 3000 hours, the statistical uncertainties are still of the same order of magnitude as the effect under study.

The results of the study, shown in Figure 6.17, are highly inconclusive due to the aforementioned lack of statistics. For distances below 1 cm, the presence of an adjacent chamber in the X direction seems to reduce the dose collected by the reference chamber, probably by reducing the lateral equilibrium of secondary electrons. However, the effect of placing an adjacent chamber behind the reference chamber seems to be the opposite one, increasing the dose collected by the latter. This effect could be caused by particles backscattered by the second chamber. No clear trends can be identified in the diagonal directions.

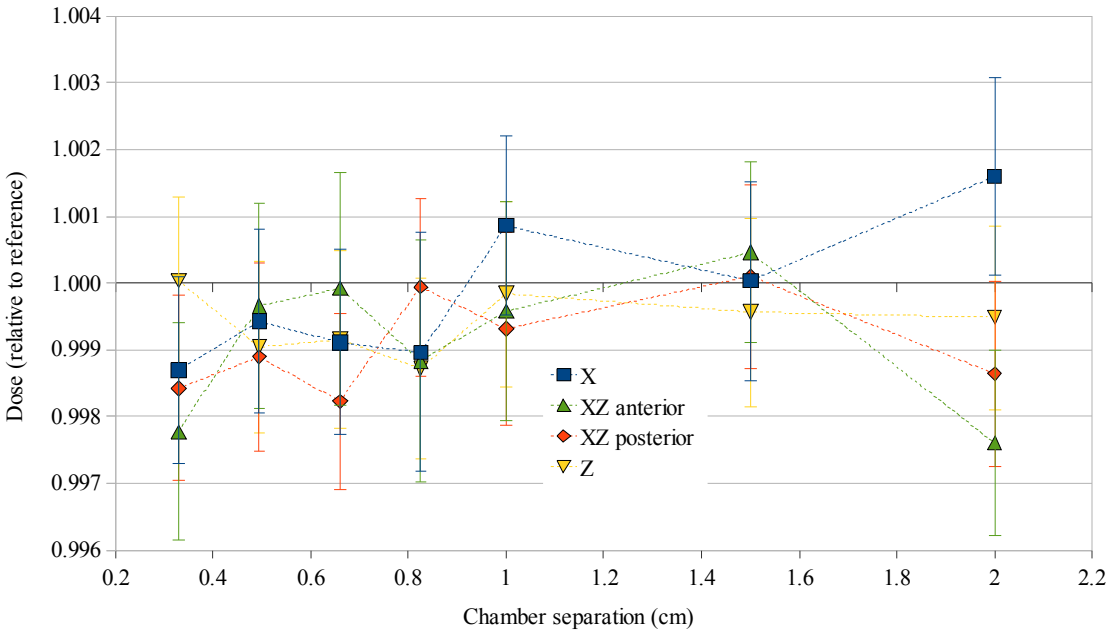

Figure 6.17. Dose collected by the reference chamber in presence of a second chamber at a given distance in four different directions, relative to the dose by collected by the chamber in absence of a second chamber. Solid lines are shown only to guide the eye.

Since the crosstalk effect cannot be accurately characterized, it is also not possible to determine a minimum packing distance above which its relevance decreases. It is clear, in any case, that for all the studied distances, physical crosstalk effects are not bigger than 0.3% of the collected dose. That is the only affirmation which can be supported by the collected statistics.

The combined effect of the surrounding chambers was also simulated, by simulating the irradiation of a cubic volume of homogeneous dose (cf. section 5.4.4.3), and comparing the dose collected by a single IC centred in the cube, with the dose collected by the same IC, placed at the same position, but surrounded by other ICs with the same spatial distribution as in the verification matrix. After more than 10^7 primaries, the chamber which was immersed in the matrix collected 0.25% more dose than the "lonely" one. Since the statistical dose uncertainty was 0.4%, no statistically significant effect could be observed on the basis of the simulated data.

6.3.3. Chamber-specific $s_{w,air}$

The code described in chapter 5 was adapted to score water-to-air stopping ratio in macroscopic regions, instead of in a voxel-per-voxel basis. This was used to score the quantities *fluw* and *flua* inside the sensitive volume of the ionization chamber, so that the quantity *fluw/flua* yields directly the stopping power ratio "as seen by" the ionization chamber, for the irradiation of patient plan #1, with the ionization matrix placed at the distal edge of the target, as shown in Figure 6.18.

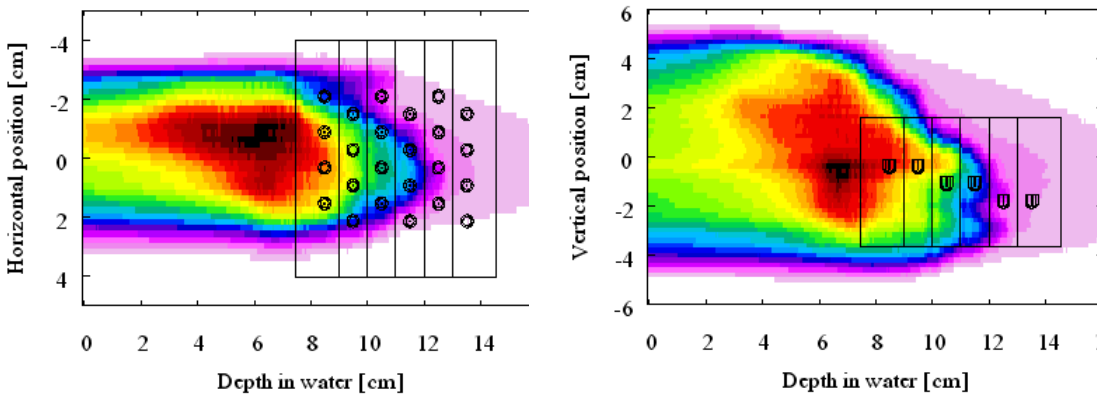

Figure 6.18. Vertical and horizontal projections of the ionization chamber matrix in the field. Dose distribution shown at the background for y=0 (horizontal projection, left) and for x=0 (vertical projection, right).

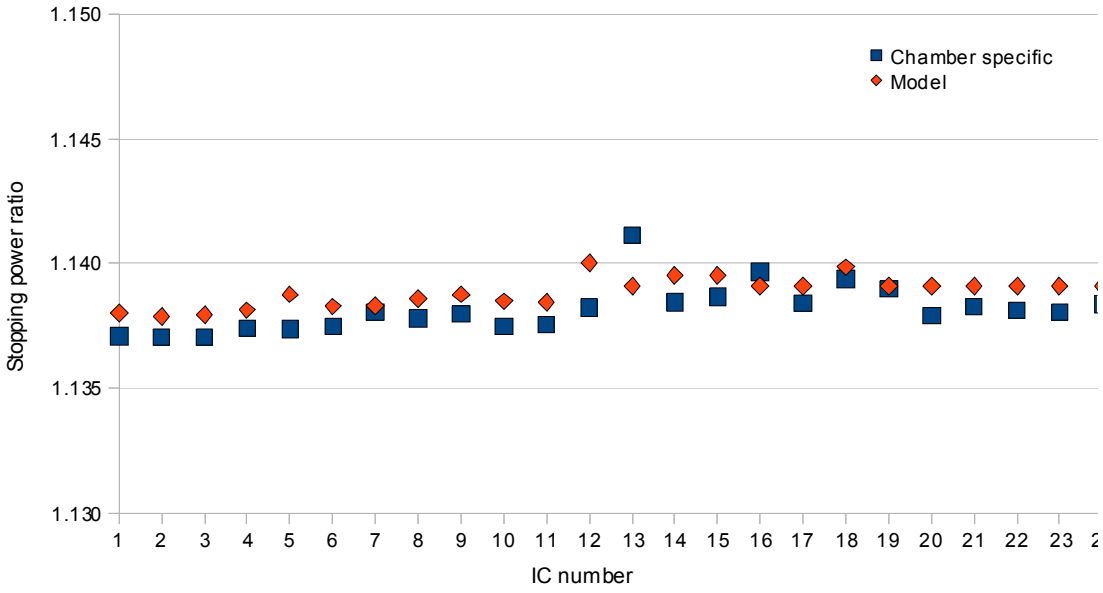

Figure 6.19. Chamber-specific values of $s_{w,air}$ for patient plan #1 and matrix geometry as shown in Figure 6.15, as calculated with full FLUKA simulation (blue) and as predicted by the residual range model according to the effective position of the chambers (red). Positions of the ionization chambers are detailed in Figure 6.14.

The chamber-specific values of $s_{w,air}$ were compared with the values calculated by the residual range model, using the effective point of the chambers as an input. The result is shown in Figure 6.19. The residual range model yielded values slightly higher than the FLUKA calculated ones, but the difference was only about 0.1%. As expected, the mismatch was slightly higher for areas of higher dose gradients (i.e. chambers #12 and #13, placed at the distal area, see Figure 6.14).

On the basis of the results of the simulation, it can be concluded that the stopping power ratio model proposed in section 5.5 can be applied to treatment plan verification with ionization chambers, as described in section 6.2.3. A finite volume effect is observed, but its impact is reasonably low, at least for the model of ionization chambers used (PTW model 31015), with a sensitive volume of 0.03 cm^3. Further investigations with chambers of different sensitive volumes might be interesting to make sure that the mentioned volume effects do not exceed the uncertainty margins.

6.4. Conclusions

Treatment plan verification for particle therapy radiotherapy is a complex procedure, and its results can be affected by purely physical effects (fragmentation of the beam, variation of $s_{w,air}$ over the treatment field) and practical considerations (chamber calibration and finite volume effects, crosstalks between different ionization chambers). Monte Carlo techniques are a useful and precise way of studying such complex systems. The set of simulations presented in this chapter bring some insights on plan verification for carbon ion beam fields.

The empirical model describing the range dependence of $s_{w,air}$ has been applied to real 3D treatment plans with successful results, using the plan information available from any TPS code: physical basic data, raster point positions and iso-energy slices. When performing treatment plan verification with ionization chambers, a chamber-specific correction accounting for the dependence of $s_{w,air}$ with the effective point of measurement could be easily implemented in the TPS and would result in a slight improvement of the overall accuracy of the plan verification module. The described model is consistent with the FLUKA MC calculations.

Finally, Monte Carlo simulations of the irradiation of a complete ionization chamber matrix (proposed in [KARGER1999] and currently in use in many treatment centres) have found no relevant geometrical crosstalks in the plan verification scheme. However, a minor volume effect might take place, lowering the apparent stopping power ratio of the chambers by a very small percentage. Its impact might have to be considered when further improving the accuracy of the $s_{w,air}$ model for absolute dosimetry, paying special attention to the transport thresholds of the MC calculations, and when possibly, validating the simulations against experimental data.

CHAPTER 7 Outlook and conclusions

In a complex medical technique such as particle therapy, the accuracy of the treatment is determined by a huge number of factors arising from intrinsic physical properties, partial understanding of the biological processes involved, and practical constraints in the delivery of the treatment. Within such a multidisciplinary framework, all the relevant fields (physics, engineering, biology, medicine) have to give their best, in a coordinated fashion, to be able to provide the best possible treatment to the patients. In this context, a precise and consistent set of dosimetric protocols has a clear impact on the state of the art, as it reduces uncertainties in further biological and clinical studies.

There are only a few facilities dedicated to carbon ion beam radiotherapy in operation in the world. In this context, and taking into account that they are dedicated to patient treatment for most of the time, experimental data are very valuable and relevant. Because of that, measurements are an important part of the work presented in this Thesis. The indirect determination of the mean ionization potential of water (I_w) from range measurements, presented in Chapter 4 as a part of the initial validation and calibration of the used FLUKA Monte Carlo code, is an example of that. Although it cannot be considered a precise method to obtain I_w, because it depends strongly on the underlying FLUKA models, it undoubtedly adds more evidence to support an I-value in the range of 78 eV for water, coinciding with the latest reports from ICRU.

The main experimental contribution in this work is the direct measurement of the water-to-air stopping power ratio from incremental projectile range shifts. The obtained value of $s_{w,air} = 1.132 \pm 0.003$ (statistical) $\pm$ 0.003 (variation over the considered energy range) is in agreement with the previously published data. By fitting the measured data to an analytical expression, a ratio of I-values between air and water was determined, namely $I_{air}/I_w = 1.157 \pm 0.023$. This ratio would mean that the I-value for air, assuming $I_w = 78$ eV, would be slightly higher than the commonly adopted values. Thus, there is certainly room for further investigations on this topic.

The described experimental procedure could be applied with some modifications to determine $s_{w,air}$ for different projectiles other than carbon, such as protons, alpha particles or oxygen ions, and at energies different than the ones considered. In particular, it would be interesting to continue with measurements in the low-energy area, in order to observe experimentally the predicted raise in $s_{w,air}$ towards the end of the Bragg peak.

In a second step of the work, Monte Carlo simulations were carried out, using the collected experimental data as an input, to calculate water to air stopping power ratio in three-dimensional volumes irradiated with different treatment plans. The results of the simulation are consistent with the previously published data generated with other codes: a raise at the distal end of the peaks is observed, and this raise is more pronounced for pristine peaks than for SOBPs. No effects are observed in the transversal directions, what allows a description of $s_{w,air}$ as a function of the residual range. Such a description is already in use for proton

absolute dosimetry, and it could now be implemented into the clinical protocols for carbon ion beam dosimetry.

Although the main scope of studying water-to-air stopping power ratios is the determination of beam quality correction factors for absolute dosimetry with ion chambers, the findings can also be used to improve accuracy in dosimetry outside reference conditions. Air-filled ionization chambers of different types are used in several QA and dosimetry procedures, from determination of depth dose distributions, to patient plan verification. The variation of water-to-air stopping ratio within the treatment field can lead to errors in the subpercent level which can be relevant for precision measurements. In such cases, we demonstrated that a simple model to determine $s_{w,air}$ from the residual range can be applied to minimize those errors with minimal effort and easy integration in treatment planning systems.

Overall, a complete study including theory, experimental measurements, data analysis, Monte Carlo simulation and application to practical cases from operational ion beam therapy centres has been presented, providing novel insights which can help to improve the quality and precision of QA and dosimetry procedures with carbon ion beams.

Publications resulting from this Thesis

Articles in peer-reviewed journals:

- D Sánchez-Parcerisa, A Gemmel, O Jäkel, K Parodi and E Rietzel, 2012. "Experimental study of water-to-air stopping power ratio of monoenergetic carbon ion beams for particle therapy". *Phys. Med. Biol.* 57 (2012) 3629-3641

Oral presentations in specialized congresses and conferences

- D Sánchez-Parcerisa, A Gemmel, K Parodi, O Jäkel and E Rietzel, 2011. Experimental investigation of water-to-air stopping power ratio and mean air ionization potential in therapeutic carbon ion beams. PTCOG 50, Philadelphia, USA, 13th May 2011.

- D Sánchez-Parcerisa, A Gemmel, K Parodi, O Jäkel and E Rietzel, 2011. Investigation of water-to-air stopping power ratio for carbon ion beam dosimetry based on experimental data and FLUKA simulation. AAPM&COMP Joint Meeting, Vancouver, Canada. 2nd August 2011.

Poster presentations

- D Sánchez-Parcerisa, A Gemmel, O Jäkel, K Parodi and E Rietzel, 2012. Effect of water-to-air stopping power ratio in patient plan verification for carbon ion radiotherapy. PTCOG 51, NCC, Goyang and Seoul, South Korea, 14th-19th May 2012.

References

[AMALDI2010] Amaldi U et al. 2010. Accelerators for hadrontherapy: From Lawrence cyclotrons to linacs. Nuclear Instruments and Methods in Physics Research Section A: Accelerators, Spectrometers, Detectors and Associated Equipment, 620, (2-3) 563-577.

[ANDERSEN2004] Andersen V et al. 2004. The FLUKA code for space applications: recent developments. Advances in Space Research, 34, (6) 1302-1310.

[BARKAS1963] Barkas HW 1963. Nuclear Research Emulsions. New York, Academic.

[BATTISTONI2006] Battistoni G et al. 2006, Recent developments in the FLUKA nuclear reaction models. 11th Intl. Conf. on Nucl. React. Mech, 12-16 June 2006.

[BATTISTONI2007] Battistoni G et al. 2006. The FLUKA code: Description and benchmarking, In Proceedings of the Hadronic Shower Simulation Workshop 2006, Albrow M & Raja R (ed), pp. 31-49.

[BERGER2005] Berger MJ et al. 2005. ESTAR, PSTAR, and ASTAR: Computer Programs for Calculating Stopping-Power and Range Tables for Electrons, Protons, and Helium Ions. <http://physics.nist.gov/Star> (accessed on 6/1/2012).

[BERT2011] Bert C & Durante M 2011. Motion in radiotherapy: Particle therapy. Phys. Med. Biol., 56, (16) R113.

[BETHE1930] Bethe H 1930. Zur Theorie des Durchgangs schneller Korpuskularstrahlen durch Materie. Annalen der Physik, 397, (3) 325-400.

[BETHE1953] Bethe HA 1953. Molière's Theory of Multiple Scattering. Physical Review, 89, (6) 1256-1266.

[BIPM2008] BIPM 2008. Evaluation of measurement data - Guide to the expression of uncertainty in measurement., JCGM 100:2008 ed.

[BIPM2008A] BIPM 2008. Evaluation of measurement data - Supplement 1 to the "Guide to the expression of uncertainty in measurement" – Propagation of distributions using a Monte Carlo method, JCGM 101:2008 ed.

[BLOCH1933] Bloch F 1933. Zur Bremsung rasch bewegter Teilchen beim Durchgang durch Materie. Annalen der Physik, 408, (3) 285-320.

[BÖHLEN2010] Böhlen TT et al. 2010. Benchmarking nuclear models of FLUKA and GEANT4 for carbon ion therapy. Phys. Med. Biol., 55, (19) 5833.

[BORTFELD1997] Bortfeld T 1997. An analytical approximation of the Bragg curve for therapeutic proton beams. Med. Phys., 24, (12) 2024-2033.

[BREDE2006] Brede HJ et al. 2006. Absorbed dose to water determination with ionization chamber dosimetry and calorimetry in restricted neutron, photon, proton and heavy-ion radiation fields. Phys. Med. Biol., 51, (15) 3667.

[BWT2003] BWT 2003. CILLIT HS Combi 2 Safety Data Sheet.

[CARABEFERNANDEZ2011] Carabe-Fernandez A et al. 2011 SU-E-T-648: Range Uncertainty in Proton Therapy Due to Variable Biological Effectiveness, 6th ed, AAPM, p. 3639.

[CERUTTI2006] Cerutti F et al. 2006. Low energy nucleus-nucleus reactions: the BME approach and its interface with FLUKA, 11th Intl. Conf. on Nucl. React. Mech., pp. 507-511.

[CHU2006] Chu WT 2006. Overview of Light-Ion Beam Therapy. ICRU-IAEA Meeting, 16th Jun 2006.

[COMBS2010] Combs SE et al. 2010. Particle therapy at the Heidelberg Ion Therapy Centre (HIT): Integrated research-driven university-hospital-based radiation oncology service in Heidelberg, Germany. Radiotherapy and Oncology, 95, (1) 41-44.

[CUTTONE2011] Cuttone G 2011. Dosimetry Techniques for Ion Beams. From the book "Ion Beam Therapy", Ute Linz (ed). Springer, 2011.

[DEMENTYEV1999] Dementyev AV & Sobolevsky NM 1999. SHIELD: universal Monte Carlo hadron transport code: scope and applications. Radiation Measurements, 30, (5) 553-557.

[ECO2011] European Cancer Observatory <http://eu-cancer.iarc.fr> (accessed on 3/1/2012).

[ELSÄSSER2010] Elsässer T et al. 2010. Quantification of the Relative Biological Effectiveness for Ion Beam Radiotherapy: Direct Experimental Comparison of Proton and Carbon Ion Beams and a Novel Approach for Treatment Planning. International journal of radiation oncology, biology, physics, 78, (4) 1177-1183.

[FANO1954] Fano U 1954. Inelastic Collisions and the MoliÃ¨re Theory of Multiple Scattering. Physical Review, 93, (1) 117-120.

[FASSO2005] Fasso A, Ferrari A, Ranft J, and Sala PR 2005. FLUKA: a multi-particle transport code. CERN-2005-10; INFN/TC_05/11; SLAC-R-773.

[FERRARI1998] Ferrari A. & Sala PR 1998. The Physics of High Energy Reactions. Singapore, World Scientific.

[GEITHNER2006] Geithner O et al. 2006. Calculation of stopping power ratios for carbon ion dosimetry. Phys. Med. Biol., 51, (9) 2279-2292.

[GEMMEL2010] Gemmel A et al. 2010. Development and performance evaluation of a dynamic phantom for biological dosimetry of moving targets. Phys. Med. Biol., 55, (11) 2997.

[GEMMEL2008] Gemmel A et al. 2008. Biological dose optimization with multiple ion fields. Phys. Med. Biol., 53, (23) 6991.

[GEORG2010] Georg D 2010. Adaptive ion beam therapy. PARTNER Course: Hadrontherapy today and tomorrow (slides), Geneva, February 2010.

[GILLIN2010] Gillin MT et al. 2010. Commissioning of the discrete spot scanning proton beam delivery system at the University of Texas M.D. Anderson Cancer Centre, Proton Therapy Centre, Houston. Med. Phys., 37, (1) 154-163.

[GILLIN2011] Gillin MT, Zhu XR, & Sahoo N 2011. Considerations for an Effective Quality Assurance Program for Proton Therapy. From the book "Ion Beam Therapy", Ute Linz (ed). Springer, 2011.

[GOTTSCHALK1993] Gottschalk B et al. 1993. Multiple Coulomb scattering of 160 MeV protons. Nuclear Instruments and Methods in Physics Research Section B: Beam Interactions with Materials and Atoms, 74, (4) 467-490.

[GOTTSCHALK2004] Gottschalk B 2004. Passive Beam Spreading in Proton Radiation Therapy (report) <http://huhepl.harvard.edu/˜gottschalk> (accessed on 3/1/2012).

[GRAYBILL1959] Graybill FA & Deal RB 1959. Combining unbiased estimators. Biometrics, 15, 543-550.

[GRÜBLING2009] Grübling P & Weber U 2009. Status Report: Particle Therapy Centre of Marburg. 48th Particle Therapy Cooperative Group (PTCOG), 24th November 2009.

[GUDOWSKA2004] Gudowska I et al. 2004. Ion beam transport in tissue-like media using the Monte Carlo code SHIELD-HIT. Phys. Med. Biol., 49, (10) 1933.

[GUNZERTMARX2008] Gunzert-Marx K et al. 2008. Secondary beam fragments produced by 200 MeV/u 12C ions in water and their dose contributions in carbon ion radiotherapy. New Journal of Physics, 10, (7) 075003.

[HABERER1993] Haberer T et al. 1993. Magnetic scanning system for heavy ion therapy. Nuclear Instruments and Methods in Physics Research Section A: Accelerators, Spectrometers, Detectors and Associated Equipment, 330, (1-2) 296-305.

[HABERER2004] Haberer T et al. 2004. The Heidelberg Ion Therapy Centre. Radiother.Oncol., 73 Suppl 2, S186-S190.

[HAETTNER2006] Haettner E. 2006. Diploma Thesis: Experimental study on carbon ion fragmentation in water using GSI therapy beams. GSI.

[HARTMANN1999] Hartmann GH et al. 1999. Determination of water absorbed dose in a carbon ion beam using thimble ionization chambers. Phys. Med. Biol., 44, (5) 1193.

[HAYNES2010] Haynes, W 2010. Handbook of Chemistry and Physics, 91st Edition ed. CRC Press.

[HENKNER2009] Henkner K et al. 2009. Monte Carlo simulations on the water-to-air stopping power ratio for carbon ion dosimetry. Med.Phys., 36, (4) 1230-1235.

[HIGHLAND1975] Highland VL 1975. Some practical remarks on multiple scattering. Nuclear Instruments and Methods, 129, (2) 497-499.

[HIRAOKA1995] Hiraoka T & Bichsel H 1995. Stopping power and ranges for heavy ions. Jpn.J.Med.Phys., 15, 91-100.

[HOWLADER2011] Howlader N et al. 2011. SEER Cancer Statistics Review, 1975-2008 National Cancer Institute. Bethesda, MD.

[IAEA2000] IAEA 2000. Absorbed Dose Determination in External Beam Radiotherapy: An International Code of Practice for Dosimetry based on Standards of Absorbed Dose to Water Technical Report Series TRS-398.

[IAEA2008] IAEA 2008. Relative Biological Effectivness In Ion Beam Therapy. Technical Report Series TRS-461.

[ICRU1994] ICRU 1994. ICRU Report 49: Stopping powers and ranges for protons and alpha particles. Med. Phys., 21, (5) 709-710.

[ICRU1998] ICRU 1998. ICRU Report 59: Clinical Proton Dosimetry - Part I: Beam Production, Beam Delivery and Measurement of Absorbed Dose. Journal of Applied Physics.

[ICRU2000] ICRU 2000. ICRU Report 63: Nuclear Data for Neutron and Proton Radiotherapy and for Radiation Protection.

[ICRU2005] ICRU 2005. ICRU Report 73: Stopping of ions heavier than helium.

[ICRU2007] ICRU 2007. ICRU Report 78: Prescribing, Recording, and Reporting Proton-Beam Therapy.

[JÄKEL2000] Jäkel O et al. 2000. Effective point of measurement of cylindrical ionization chambers for heavy charged particles. Phys. Med. Biol., 45, (3) 599.

[JÄKEL2001] Jäkel O et al. 2001. Relation between carbon ion ranges and x-ray CT numbers. Med. Phys., 28, (4) 701-703.

[JÄKEL2004] Jäkel O et al. 2004. A calibration procedure for beam monitors in a scanned beam of heavy charged particles. Med. Phys., 31, (5) 1009-1013.

[JANNI1982] Janni JF 1982. Energy loss, range, path length, time-of-flight, straggling, multiple scattering, and nuclear interaction probability: In two parts. Part 1. For 63 compounds Part 2. For elements Z=1-92. Atomic Data and Nuclear Data Tables, 27, (2-3) 147-339.

[JONGEN2010] Jongen Y et al. 2010. Compact superconducting cyclotron C400 for hadron therapy. Nuclear Instruments and Methods in Physics Research Section A: Accelerators, Spectrometers, Detectors and Associated Equipment, 624, (1) 47-53.

[KANAI1997] Kanai T et al. 1997. Irradiation of mixed beam and design of spread-out Bragg peak for heavy-ion radiotherapy. Radiat.Res., 147, (1) 78-85.

[KANEMATSU2003] Kanematsu N et al. 2003. A CT calibration method based on the polybinary tissue model for radiotherapy treatment planning. Phys. Med. Biol., 48, (8) 1053.

[KARGER1999] Karger CP, Jakel O, & Hartmann GH 1999. A system for three-dimensional dosimetric verification of treatment plans in intensity-modulated radiotherapy with heavy ions. Med.Phys., 26, (10) 2125-2132.

[KARGER2010] Karger C et al. 2010. Dosimetry for ion beam radiotherapy. Phys. Med. Biol., 55, (21) R193-R234.

[KEMPE2008] Kempe J & Brahme A 2008. Energy-range relation and mean energy variation in therapeutic particle beams. Med. Phys., 35, (1) 159-170.

[HIT2011] Klinikum Uni Heidelberg 2011. Zwei Jahre Heidelberger Ionenstrahl-Therapiezentrum: Universitätsklinikum Heidelberg zieht eine positive Bilanz.

[KRAFT2000] Kraft G 2000. Tumor therapy with heavy charged particles. Progress in Particle and Nuclear Physics, 45, S473-S544.

[KRAMER2000] Krämer M et al. 2000. Treatment planning for heavy-ion radiotherapy: physical beam model and dose optimization. Phys. Med. Biol., 45, (11) 3299-3317.

[KRAMER2000A] Krämer M & Scholz M 2000. Treatment planning for heavy-ion radiotherapy: calculation and optimization of biologically effective dose. Phys. Med. Biol., 45, (11) 3319-3330

[LECHNER2010] Lechner A, Ivanchenko VN, & Knobloch J 2010. Validation of recent Geant4 physics models for application in carbon ion therapy. Nuclear Instruments and Methods in Physics Research Section B: Beam Interactions with Materials and Atoms, 268, (14) 2343-2354.

[LIN2009] Lin S et al. 2009. More than 10 years experience of beam monitoring with the Gantry 1 spot scanning proton therapy facility at PSI. Med. Phys., 36, (11) 5331-5340.

[LOMAX2001] Lomax AJ et al. 2001. Intensity modulated proton therapy: A clinical example. Med. Phys., 28, (3) 317-324.

[LOMAX2004] Lomax AJ et al. 2004. Treatment planning and verification of proton therapy using spot scanning: Initial experiences. Med. Phys., 31, (11) 3150-3157.

[LUHR2011] Luhr A et al. 2011. Analytical expressions for water-to-air stopping-power ratios relevant for accurate dosimetry in particle therapy. Phys. Med. Biol., 56, (8) 2515-2533.

[LYNCH1991] Lynch GR & Dahl OI 1991. Approximations to multiple Coulomb scattering. Nuclear Instruments and Methods in Physics Research Section B: Beam Interactions with Materials and Atoms, 58, (1) 6-10.

[DOSANJH2008] Dosanjh M 2008. Development of Hadron Therapy for Cancer Treatment in Europe, In AIP Conf. Proc., pp. 12-16.

[MARC2010] Marc M 2010. Proton therapy: scattering versus scanning. Med. Phys. Web.

[MATSUFUJI1998] Matsufuji N et al. 1998. Relationship between CT number and electron density, scatter angle and nuclear reaction for hadron-therapy treatment planning. Phys. Med. Biol., 43, (11) 3261.

[MAUGHAN2008] Maughan RL & Farr JB 2008. Quality assurance for proton therapy. From the book "Proton and charged particle radiotherapy", T. F. DeLaney et al. (ed). Lippincott Williams and Wilkins, Philadelphia, 2008.

[MEDIN1997] Medin J & Andreo P 1997. Monte Carlo calculated stopping-power ratios, water/air, for clinical proton dosimetry (50 - 250 MeV). Phys. Med. Biol., 42, (1) 89.

[METROPOLIS1987] Metropolis N 1987. The beginning of the Monte Carlo method. Los Alamos Science, Special Issue.

[MINOHARA1993] Minohara S et al. 1993. Effects of object size on a function to convert x-ray CT numbers into the water equivalent path length of charged particle beam, NIRS Publication NIRS-M-99, pp. 14-15.

[MOLIÈRE1947] Molière G 1947. Theorie der Streuung schneller geladener Teilchen.I. Einzelstreuung am abgeschirmten Coulomb-Feld. II. Mehrfach und Vielfachstreuung. Z.Naturforsch.A, 2, 133-145.

[MOLIÈRE1948] Molière G 1948. Theorie der Streuung schneller geladenen Teilchen II Mehrfachund Vielfachstreuung. Z.Naturforsch.A, 3, 78-97.

[NASA2011] NASA 2011. NASA PDS: The Planetary Atmospheres Data Node. <http://atmos.nmsu.edu/education_and_outreach/encyclopedia/sat_vapor_pressure.htm> (accessed on 10/1/2012).

[NEWHAUSER2009] Newhauser W 2009. International Commission on Radiation Units and Measurements Report 78: Prescribing, Recording and Reporting Proton-beam Therapy. Radiation Protection Dosimetry, 133, (1) 60-62.

[NIEDERLANDER2006] Niederlander E 2006. Causes of death in the EU. Eurostat - Population and social conditions - Statistics in focus, Report number KS-NK-06-010-EN-N.

[NIITA2006] Niita K et al. 2006. PHITS: A particle and heavy ion transport code system. Radiation Measurements, 41, (9-10) 1080-1090.

[PAGANETTI2002] Paganetti H et al. 2002. Relative biological effectiveness (RBE) values for proton beam therapy. International journal of radiation oncology, biology, physics, 53, (2) 407-421.

[PARODI2007] Parodi K et al. 2007. Clinical CT-based calculations of dose and positron emitter distributions in proton therapy using the FLUKA Monte Carlo code. Phys. Med. Biol., 52, (12) 3369-3387.

[PARODI2009] Parodi K et al. The FLUKA code for application of Monte Carlo methods to promote high precision ion beam therapy , In 12th International Conference on Nuclear Reaction Mechanisms, Villa Monastero, Varenna, Italy.

[PARODI2012] Parodi K et al. 2012. Monte Carlo simulations to support start-up and treatment planning of scanned proton and carbon ion therapy at a synchrotron-based facility. Phys. Med. Biol.

[PAUL2007] Paul H, Geithner O, & Jakel O 2007. The ratio of stopping powers of water and air for dosimetry applications in tumor therapy. Nuclear Instruments and Methods in Physics Research B, 256, 561-564.

[PEDRONI1995] Pedroni E et al. 1995. The 200-MeV proton therapy project at the Paul Scherrer Institute: Conceptual design and practical realization. Med. Phys., 22, (1) 37-53.

[PODGORSAK2005] Podgorsak EB et al. 2005. Radiation oncology physics: a handbook for teachers and students. International Atomic Energy Agency, Vienna, Austria.

[PTCOG2011] PTCOG 2011. Hadron Therapy Patient Statistics (as of May 2011) <http://ptcog.web.psi.ch> (accessed on 23/7/2011).

[PTW2008] PTW 2008. PEAKFINDER Water Column T41030 with Servo Control Unit T41027 user manual.

[PTW2009] PTW 2009. PinPoint Chambers 3101X user manual.

[RKA2011] Rhön-Klinikum AG 2011. Entwicklungs-Projekt Partikeltherapie wird beendet. <http://www.rhoen-klinikum-ag.com/rka/cms/rka_2/deu/presse/97898.html>. Press note, 18th July 2011.

[RIETZEL2007] Rietzel E, Schardt D, & Haberer T 2007. Range accuracy in carbon ion treatment planning based on CT-calibration with real tissue samples. Radiat.Oncol., 2, (14).

[RINALDI2011] Rinaldi I et al. 2011. An integral test of FLUKA nuclear models with 160 MeV proton beams in multi-layer Faraday cups. Phys. Med. Biol, 56, (13) 4001.

[ROSSI1952] Rossi B 1952. High-energy particles Englewood Cliffs, NJ, Prentice-Hall.

[SAHOO2008] Sahoo N et al. 2008. A procedure for calculation of monitor units for passively scattered proton radiotherapy beams. Med. Phys., 35, (11) 5088-5097.

[SCHAFFNER1998] Schaffner B & Pedroni E 1998. The precision of proton range calculations in proton radiotherapy treatment planning: experimental verification of the relation between CT-HU and proton stopping power. Phys. Med. Biol., 43, (6) 1579.

[SCHARDT2010] Schardt D, Elsässer T, & Schulz-Ertner D 2010. Heavy-ion tumor therapy: Physical and radiobiological benefits. Reviews of Modern Physics, 82, (1) 383-425.

[SCHNEIDER1996] Schneider U, Pedroni E, & Lomax A 1996. The calibration of CT Hounsfield units for radiotherapy treatment planning. Phys. Med. Biol., 41, (1) 111.

[SCHOLZ1996] Scholz M & Kraft G 1996. Track structure and the calculation of biological effects of heavy charged particles. Adv.Space Res., 18, (1-2) 5-14.

[SCHOLZ1997] Scholz M et al. 1997. Computation of cell survival in heavy ion beams for therapy. The model and its approximation. Radiat.Environ.Biophys., 36, (1) 59-66.

[SCHOLZ2003] Scholz M 2003. Effects of Ion Radiation on Cells and Tissues. Radiation Effects on Polymers for Biological Use. Advances in Polymer Science, 162, 95-155.

[SCHULZERTNER2004] Schulz-Ertner D et al. 2004. Results of carbon ion radiotherapy in 152 patients. International Journal of Radiation Oncology*Biology*Physics, 58, (2) 631-640.

[SCHWAB1990] Schwab T 1990. Transport von Schwerionen durch Materie innerhalb ionenoptischer Systeme. (Thesis). Justus-Liebig Universität Giessen.

[SIGMUND2009] Sigmund P, Schinner A, & Paul H 2009. Errata and Addenda for ICRU Report 73, Stopping of Ions Heavier than Helium. Journal of the ICRU, 5, (1).

[SOMMERER2006] Sommerer F et al. 2006. Investigating the accuracy of the FLUKA code for transport of therapeutic ion beams in matter. Phys. Med. Biol., 51, (17) 4385-4398.

[TOBIAS1952] Tobias C, Anger H, & Lawrence J 1952. Radiological use of high energy deuterons and alpha particles. Am.J.Roentgenol.Radiat.Ther.Nucl.Med., 67, 1-27.

[TORIKOSHI2007] Torikoshi M et al. 2007. Irradiation System for HIMAC. Journal of Radiation Research, 48, (Suppl. A) A15-A25.

[TRIPATHI1996] Tripathi RK, Cucinotta FA, & Wilson JW 1996. Accurate universal parameterization of absorption cross sections. Nuclear Instruments and Methods in Physics Research Section B: Beam Interactions with Materials and Atoms, 117, (4) 347-349.

[TRIPATHI1999] Tripathi RK, Cucinotta FA, & Wilson JW 1999. Accurate universal parameterization of absorption cross sections III: light systems. Nuclear Instruments and Methods in Physics Research Section B: Beam Interactions with Materials and Atoms, 155, (4) 349-356.

[UZAWA2009] Uzawa A et al. 2009. Comparison of Biological Effectiveness of Carbon-Ion Beams in Japan and Germany. International journal of radiation oncology, biology, physics, 73, (5) 1545-1551.

[VLACHOUDIS2009] Vlachoudis V 2009. FLAIR: A Powerful But User Friendly Graphical Interface For FLUKA. Conf. Proceeding, Proc.Int.Conf.on Mathematics, Computational Methods & Reactor Physics. Saratoga Springs, New York, 2009.

[WEBER1999] Weber U & Kraft G 1999. Design and construction of a ripple filter for a smoothed depth dose distribution in conformal particle therapy. Phys. Med. Biol., 44, (11) 2765.

[WILLIAMS2010] NASA Earth Fact Sheet <http://nssdc.gsfc.nasa.gov/planetary/factsheet/earthfact.html> (accessed on 23/6/2011).

[WILSON1946] Wilson RR 1946. Radiological use of fast protons. Radiology, 47, (5) 487-491.

[ZHANG2010] Zhang R et al. 2010. Water equivalent thickness values of materials used in beams of protons, helium, carbon and iron ions. Phys. Med. Biol., 55, (9) 2481-2493.

[ZIEGLER1999] Ziegler JF 1999. Stopping of energetic light ions in elemental matter. J. Appl. Phys., 85, (3) 1249-1272.